Quantum Chemical Computations of Heterogeneous Selective Oxidation, STM Images, and Multiple Bond Reactions

Thesis by

Francesco Faglioni

In Partial Fulfillment of the Requirements

for the Degree of

Doctor of Philosophy

California Institute of Technology

Pasadena, California

1998

(Submitted May 8, 1998)

To Rita and Elia.

Acknowledgements

I would like to thank my research advisor, Dr. W. A. Goddard III, for his advice and guidance during my graduate studies. I also thank the members of our research group both for the helpful discussions and the frivolous chatting. In particular, I would like to thank Ersan Demiralp, Mihail Iotov, Chris Kankel, and Lila Guterman.

Abstract

Chapter one of this thesis describes first principles electronic structure computations performed to understand the mechanism of molecular oxygen activation by vanadyl pyrophosphate. The process is believed to play a key role in the catalytic oxidation of n-butane to maleic anhydride. The results obtained demonstrate that the mechanism involves at least two layers of vanadyl pyrophosphate crystal. Based on the computed energetics for small clusters, we propose an activation mechanism which involves the transfer of one oxygen atom from the first to the second layer of the crystal concerted with dioxygen activation by the first layer.

Chapter two describes a novel ab-initio computational technique, called GVB-RCI, which correctly describes the stretching and dissociation of multiple bonds and provides smooth potential energy surfaces for most chemical reactions. The technique is a special case of Multi Configuration SCF that does not have the Perfect Pairing restriction and still scales well with the size of the system. The capabilities and limitations of GVB-RCI are illustrated in the case of a few simple chemical reactions.

Chapter three contains a theoretical model describing the Scanning Tunneling Microscopy (STM) imaging of molecules adsorbed on graphite. The model is applicable to a variety of different molecules with reasonable computational effort, and provides images that are in qualitative agreement with experimental results. The model predicts that topographic effects will dominate the STM images of alkanes on graphite surfaces. The computations correlate well with the STM data of functionalized alkanes, and allow assessment of the structure and orientation of most of the functionalized alkanes that have been studied experimentally. In addition, the computations suggest that the highly diffuse virtual orbitals, despite being much farther in energy from the Fermi level of the graphite than the occupied orbitals of the adsorbed molecules, may play an important role in determining the STM image contrast of such systems.

Contents

List of Figures

Introduction

This thesis contains a summary of the research conducted in three different and independent projects.

Chapter 1 describes the study of molecular oxygen chemisorption and activation on vanadyl pyrophosphate crystals. This step is believed to be one of the key elementary processes in the oxidation of n-butane to maleic anhydride over VPO catalyst.

Despite several years of research in this field, we can only conjecture about the activation mechanism. The system, in fact, revealed itself to be more complicated than initially thought. So, after the simplest activation mechanisms were ruled out, we were forced to consider more sophisticated and more expensive models for the crystal. This made the computations exceedingly time consuming and only tentative results could be attained.

Chapter 2 reports a novel computational method developed to correctly describe the stretching and dissociation of multiple bonds in large systems with a reasonable computational cost. The method, called GVB-RCI, is a slight generalization of the well established GVB-PP and provides a systematic way to study the molecular motion during most chemical reactions. The capabilities and limitations of the method are illustrated with a few simple examples. This chapter contains the manuscript to be submitted for publication.

Chapter 3 contains one of two articles on STM imaging of ordered molecular monolayers on graphite published jointly with C. Claypool, N. Lewis, et al. The article describes a theoretical model used to simulate the STM process, the results of a few simulations, and the theoretical interpretation of the experimental images that we gained from the model.

Since the three chapters refer to distinct areas of research, each of them was kept independent from the others, so that the reader interested in one of the topics may conveniently skip two of the chapters. In line with this idea, each chapter contains its own abstract, bibliography, and acknowledgements.

Chapter 1 Initial Steps in Selective Oxidation by Vanadyl Pyrophosphate From First Principles Electronic Structure Calculations

Abstract

The oxidation of n-butane to maleic anhydride over vanadium phosphorus oxide (VPO) catalysts has become a major industrial process. Despite extensive experimental studies of these catalysts, there is not yet an understanding of the specific reaction steps involved. We report here first principles electronic structure studies of the initial steps for chemisorbing an oxygen molecule to the catalyst surface. We explore two possible reaction pathways leading to oxygen activation and we show that one of them cannot be part of the catalytic cycle.

1.1 Introduction

The catalytic oxidation of n-butane to maleic anhydride (MA) by equilibrated vanadium phosphorus oxide (1)

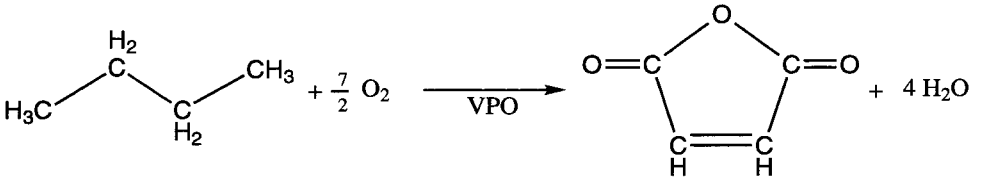

(1)

is highly selective with little side products.[1-3] Consequently this has become the major process in the US for producing MA.[3] However, productivity is low because high conversion leads to decreased selectivity.[3] Despite 20 years of research and production, the fundamental chemical mechanism for the catalytic steps is not known,[4] and we initiated theoretical studies to help elucidate the key chemical steps.

There is ample evidence[5-9] that the catalyst is vanadyl pyrophosphate crystal, (2)

$$(VO)_2P_2O_7 \tag{2}$$

In addition, there are strong indications that the reaction takes place mainly on a well defined face of the vanadyl pyrophosphate crystals.[10] This face is referred to in the literature both as (100)[5, 6, 8, 9, 11]

and (020)[11-13] and is the face obtained by cutting the crystal with a plane perpendicular to the vanadyl VO groups (see Figure 1.1). Several studies indicate a surface P/V ratio greater than one,[5-7, 10, 11] but it is not clear how the dangling bonds (surface phosphates) are saturated.

Dioxygen binds strongly to VPO. In the absence of substrate, it has a desorption peak at 430^0C and one at 520^0C,[14] indicating a chemisorption energy greater than 45 kcal/mol.

Experimental evidence[6] indicates that the rate determining step for (1) is the selective cleavage of a methylene C-H bond. One or more forms of activated oxygen in the neighborhood of the active site[2, 14] play a role in the process, but only the surface or near surface layers of the crystal are involved.[1] These observations suggest that the active site for the first steps of chemisorption and substrate activation should be well described by a small cluster of atoms suitable for first principles electronic structure calculations.

We assume that the active site for dioxygen chemisorption is one of the surface vanadium atoms. This assumption is not supported by direct experimental evidence but is based on the observation that the exposed vanadium atoms are the only acid (electron poor) centers on the surface. Thus even with further rearrangement of the structure, they would form the first bond to molecular oxygen.

In Section 2 we analyze the electronic structure of surface vanadyl groups, and in Section 3 and 4 we consider bonding of oxygen to three different clusters. Section 5 discusses the results and Section 6 contains calculational details.

1.2 Electronic Structure of the Reactants

In order to understand the mechanism of oxygen activation, it is important to establish the electronic structure of the vanadyl sites on the crystal surface and of molecular and atomic oxygen.

1.2.1 Vanadyl Groups

In bulk $(VO)_2P_2O_7$ (2), the vanadium is in the IV oxidation state, indicating that one unpaired electron remains on the V (a radical). On the surface, vanadium atoms could have oxidation state IV or V depending on how the surface dangling bonds are saturated. Experimentally, a small excess of phosphorus on the surface has often been observed and it does not quench the reaction.[2, 5-7, 12] Since excess phosphorus forces the vanadium to be IV, it is likely that the oxidation state at the first stage of the reaction is IV.

The clusters used in this paper contain, in general, some oxygen atoms that mimic the pyrophosphate oxygens of the crystal. We will refer to these atoms and to their substituents as the *equatorial* atoms. The remaining atoms include all vanadia, vanadyl oxygens and reacting oxygens, and will be referred to as *active* atoms. In the clusters examined, the dangling bonds on the equatorial oxygens were saturated following two distinct approaches.

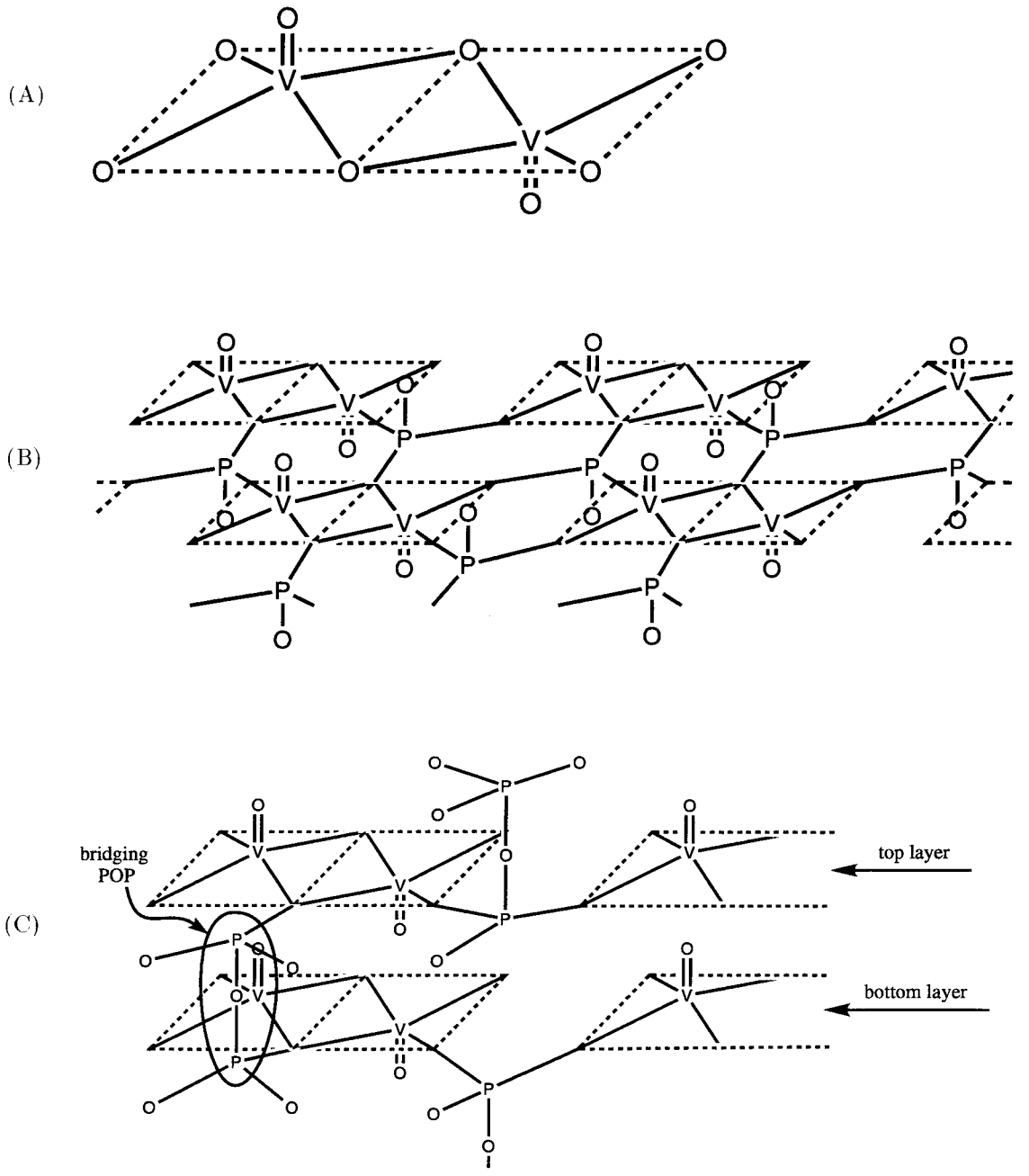

Figure 1.1: Unreconstructed (100) surface layer of Vanadyl Pyrophosphate [Based on reference 9]. The dotted lines connect six oxygen atoms lying in the same plane and indicate the basic units. The basic units (A) are connected by pyrophosphate groups to form layers (B) which are stacked with aligned vanadyl groups and held in place by *POP* bridges (C).

2(A) 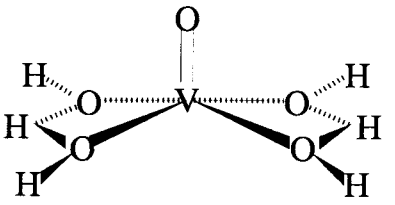

2(B) 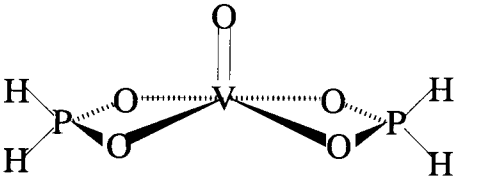

Figure 1.2: Clusters used to study the vanadyl bond. (A) H-cluster: all the equatorial oxygens and the hydrogens are constrained to be in the same plane and the cluster is forced to maintain C_{2v} symmetry; (B) P-cluster: the geometry is fully optimized with C_{2v} symmetry.

The first approach is to saturate all dangling bonds with hydrogen atoms. We call the resulting compounds H-clusters. To reproduce the fact that some of the equatorial oxygens in the crystal are equivalent, some of the hydrogen atoms were placed in a bridging position between two oxygens. Although this formally leads to a transition state, it is straightforward to inhibit the geometries to collapse by forcing a certain molecular symmetry upon all geometry optimizations. In order to mimic the geometric constraints of the crystal, the equatorial atoms were also forced to lie in the same plane throughout all geometry optimizations.

The second approach is to saturate the dangling bonds with hydrogen when the crystal oxygen would have a single covalent bond and with bridging phosphines when the crystal oxygen would have half single and half double bond character. We call these P-clusters. In this case, the geometries obtained are stable and we relaxed the constraint that all equatorial atoms lie in the same plane effectively performing full geometry optimizations. Examples of both kinds of clusters are given in Figures 1.2 and 1.5.

Since H-clusters are smaller, they were used for detailed wavefunction analysis and for expensive computational methods (MP2). P-clusters were used to verify that the results do not depend strongly on the cluster termination or on artificial constraints.

To study electronic characteristics of the vanadyl bond, $V = 0$, we considered the clusters in Figure 1.2. Both clusters lead to a formal oxidation state of V^{IV}, just as for the surface sites depicted in Figure 1.1.

Carrying out Generalized Valence Bond (GVB) calculations on cluster 2(A) leads to the orbitals in Figure 1.3. In such GVB calculations, each pair of electrons is described with two orbitals which are allowed to overlap. For a covalent bond each of the two orbitals localizes with one orbital on each atom of the bond. For a lone pair both orbitals localize on one atom. Figure 1.3a describes the covalent sigma bond between an electron in O_{p_z} and an electron in $V_{d_{z^2}}$. The two pairs of electrons in Figures 1.3b and 1.3c describe two electrons in O_{p_x} and O_{p_y}, respectively (these are collectively denoted as O_{p_π}); but each has some backbonding into the empty V_{d_π} orbitals ($d_{\pi_{xz}}$ or $d_{\pi_{yz}}$). Thus the oxygen has 5 electrons in p orbitals, corresponding to O^-.

In addition to the orbitals in Figures 1.3a, 1.3b, and 1.3c, the V has one electron in a $d_{x^2-y^2}$

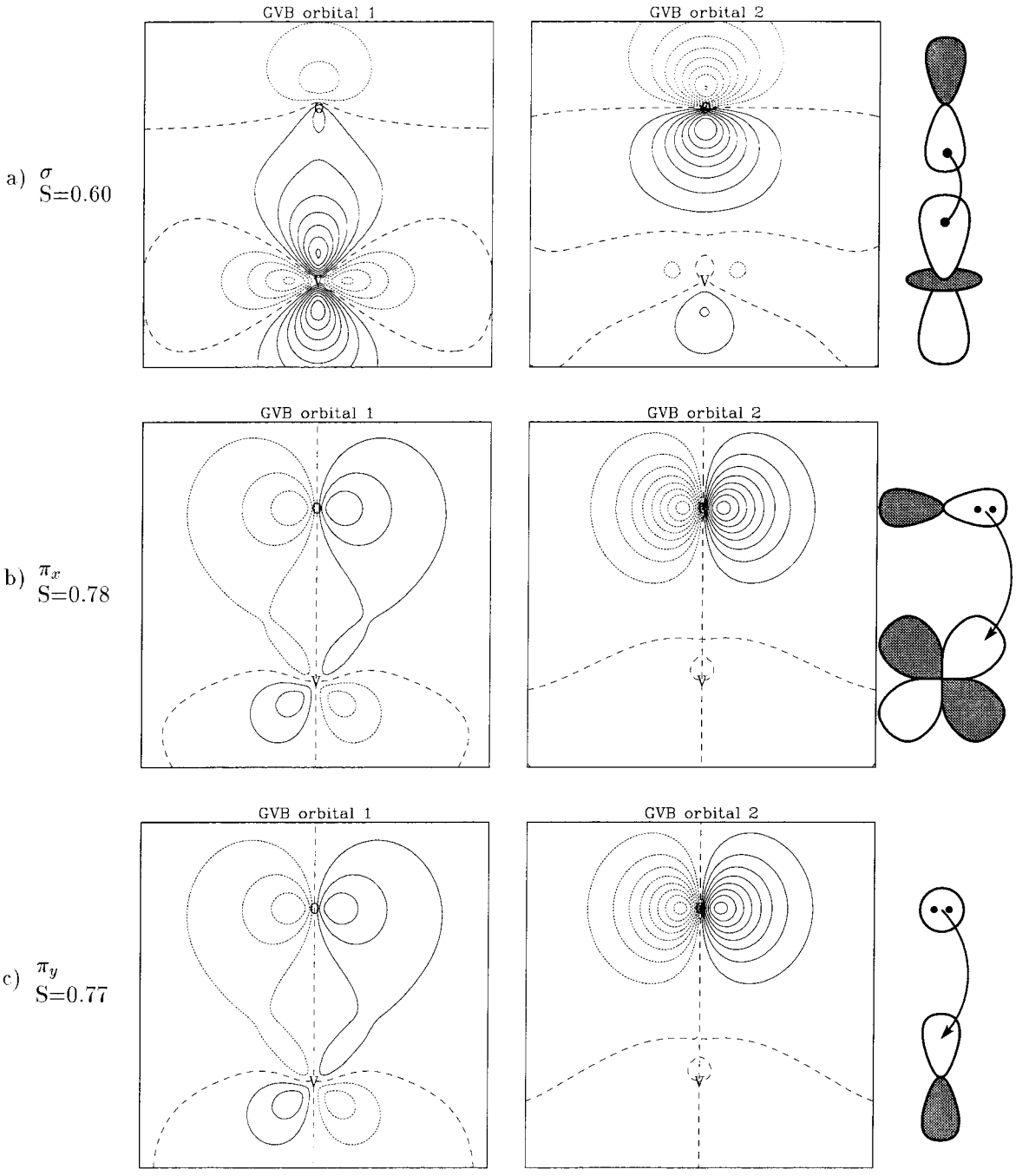

Figure 1.3: GVB orbitals describing the vanadyl group at the optimal distance $R_{VO} = 1.59$Å. Each row contains the two GVB orbitals of a bond pair, where each orbital is singly-occupied but overlapping. (a) is the covalent σ bond, (b) and (c) are equivalent donor-acceptor π bonds. The GVB diagrams for each pair give our interpretation of the orbitals. S indicates the overlap between the two orbitals forming a GVB pair.

orbital. This electron can be spin-coupled with the equivalent electron on one of the neighboring vanadyls. A proper description of this electron requires the use of a larger cluster, including at least two vanadyl groups, and it is provided later in this section. The other occupied orbitals in the complex are mainly on the equatorial ligands, with little V character.

Summarizing, the GVB wavefunction leads to a description with two valence electrons localized in d orbitals on the V: the d_{z^2} orbital making a σ bond to the O^- and a $d_{x^2-y^2}$ orbital in the equatorial plane. Thus we describe the vanadyl bond as

$$\cdot V^{3+} - O^- \tag{3}$$

where

1. V^{3+} indicates a d^2 configuration with $5 - 3 = 2$ electrons on the V (d_{z^2} bonded to the O and $d_{x^2-y^2}$ not paired).

2. O^- indicates a $(2p)^5$ configuration with the singly-occupied orbital covalently bonded to the V.

3. The dot on the V in (3) indicates an unpaired electron remaining on the V.

Formally, the oxidation state of vanadium in this cluster is described as IV because it is assumed that the covalent bond in Figure 1.3a is completely localized on the O, leading to O^{2-}. In order to minimize confusion, we will use the notation V^{IV} and V^V to indicate the *formal* oxidation state (assuming that ligands are closed shell, e.g., O^{2-}). We will use the notation V^{3+}, V^{4+}, etc., to indicate the number of electrons remaining in valence orbitals on the V (in the GVB wavefunction), e.g., 2 for V^{3+}, 1 for V^{4+}.

The above description is for the equilibrium $V^{3+} - O^-$ distance of 1.59 Å. As the bond is stretched, charge transfer is less favorable so that for 2.0Å, we obtain the result in Figure 1.4. Here we find that the σ pair corresponds to a stretched covalent bond (polarized toward the oxygen), while the π_x and π_y pairs describe one covalent bond and one lone pair on the oxygen. As the two π systems are almost equivalent, resonance between the two configurations described in Figure 1.4 plays an important role. For this case we found a resonance stabilization of 12 kcal/mol.

Thus the vanadyl for Figure 1.4 is described as

$$\cdot V^{2+} = O \tag{4}$$

where

1. V^{2+} indicates that there are $5 - 2 = 3$ electrons in d orbitals on the V.

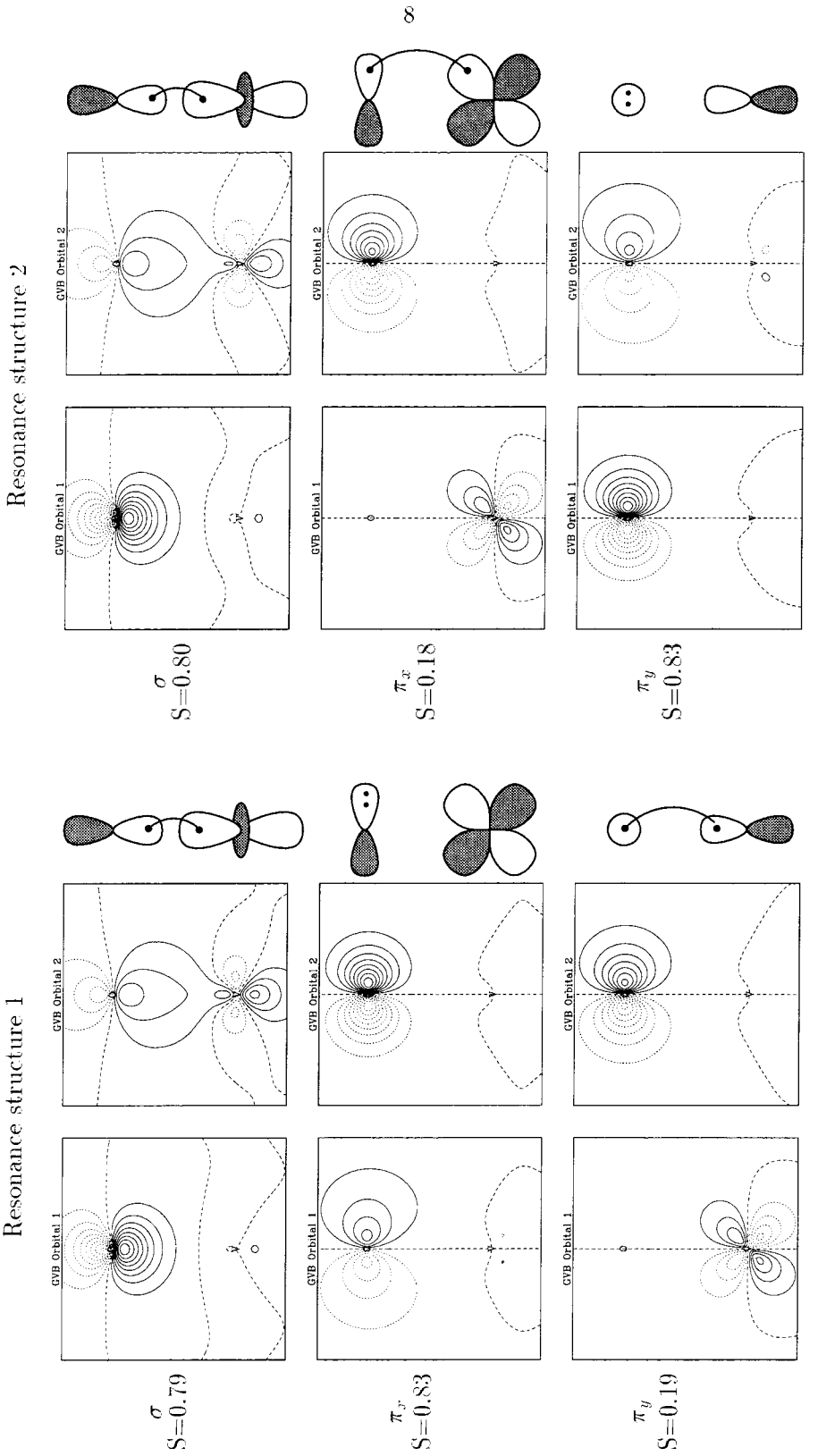

Figure 1.4: Orbitals for axial V^{IV} bonds of Figure 2(A) at $R_{V\text{-}O} = 2.0$Å. S indicates the overlap between the two orbitals forming a GVB pair.

5(A)

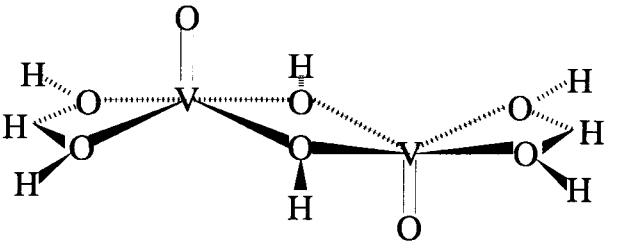

5(B)

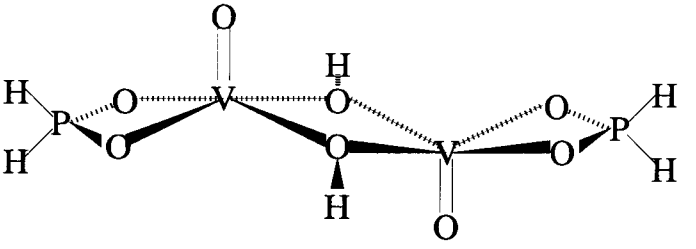

Figure 1.5: Cluster models used to study the unpaired vanadyl electron. (A) H-cluster: all the equatorial oxygens and the hydrogens are constrained to be in the same plane and the cluster is forced to maintain C_{2h} symmetry; (B) P-cluster: the geometry is fully optimized with C_{2h} symmetry.

2. O indicates that there are 4 electrons in p orbitals on the O.

3. The double bond indicates two covalent bonds.

The P-cluster 2(B) was used to verify that the choice of the ligands used to terminate the cluster is not affecting the essential picture described above and that the artificial constraints forced upon the H-cluster 2(A) are physically sound.

To study the coupling of the unpaired electron on each vanadium center, we used the clusters in Figure 1.5. The H-cluster in Figure 1.5(A) was used for the detailed wavefunction analysis. When the electrons on neighboring vanadyls are singlet paired, GVB predicts the orbitals reported in Figure 1.6. The overlap between these orbitals is very small ($S = 1.1 \cdot 10^{-4}$). The orbitals obtained when the electrons are triplet paired are essentially identical.

Although all computational methods predict the singlet and triplet states to be almost degenerate, the spin multiplicity of the ground state of the system depends on the computational method used. GVB predicts weak triplet pairing, with the singlet state 0.03 kcal/mol higher than the triplet. MP2, on the other hand, predicts the singlet to be more stable by 0.06 kcal/mol. The ground state spin configuration cannot be measured directly, but indirect evidence suggests a singlet ground state with a significant population of the triplet excited state at room temperature.[1]

1.2.2 Oxygen Atom

The orbital configuration of a free O atom is $(1s)^2(2s)^2(2p)^4$. Hence, ignoring the $1s$ and $2s$ electrons, the configuration can be represented as in Figure 1.7(A), where the p_y orbital out of the plane is

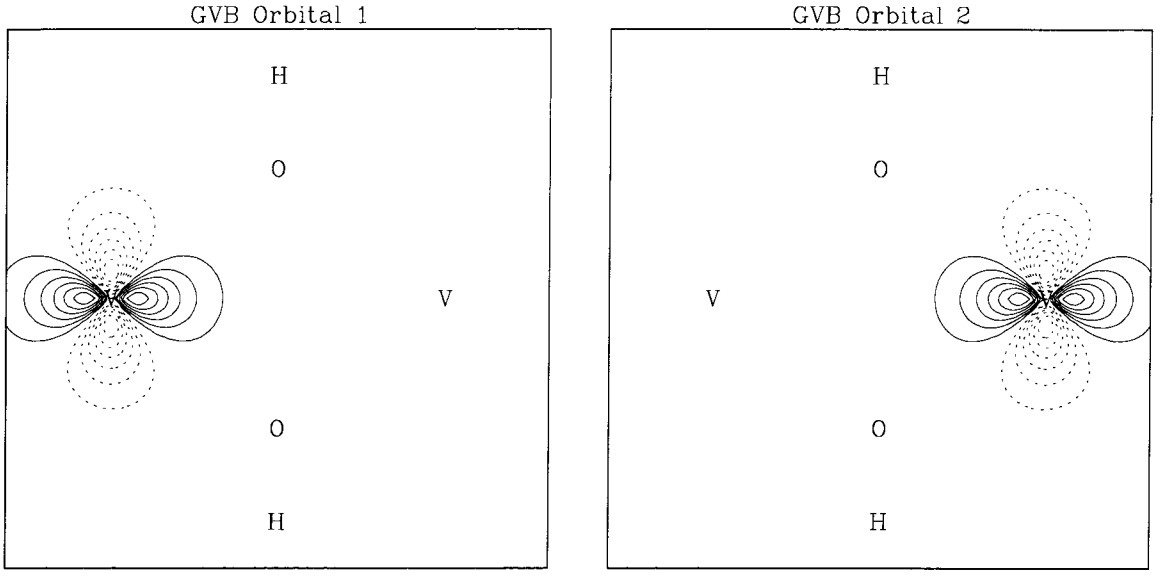

Figure 1.6: GVB orbitals describing the $d_{x^2-y^2}$ orbitals for the vanadium atoms in cluster 5(A).

represented by a circle (the top lobe of the p orbital) and the p_x and p_z orbitals in the plane are represented as two-lobed p orbitals (partially obscured by p_y). The occupations are indicated by dots. The two singly-occupied orbitals are coupled high spin to yield a $S = 1$ or triplet ground state. There are three possible configurations of spatial orbitals (with either p_x, p_y, or p_z doubly occupied), leading to the ^3P ground state of oxygen atom.

1.2.3 Oxygen Molecule

As discussed elsewhere[15] the GVB description of O_2 leads to a resonance of two configurations as in Figure 1.8 and sketched schematically in Figure 1.7(B). In each configuration, the O atoms (see Figure 1.7(A)) are oriented to make a σ bond but in such a way that the singly-occupied π orbitals do *not* overlap. The reason is that overlapping of the p_π orbitals to form a bond leads to overlap of the doubly-occupied p_π orbitals in the other plane (see Figure 1.7(C)), leading to additional repulsive interactions. Since the singly-occupied orbitals in Figure 1.7(B) are orthogonal, the ground state of O_2 is a triplet ($^3\Sigma_g^-$).

This description is equivalent to the Molecular Orbital (MO) description in which the σ and two π bonding orbitals are doubly occupied and the two π^* anti bonding orbitals are singly occupied. Notice, however, that in order to describe correctly the dissociation of the molecule, the correlation between the motions of the electrons in the π space must be accounted for. The MO description is thus somewhat incomplete unless more than one configuration are considered.

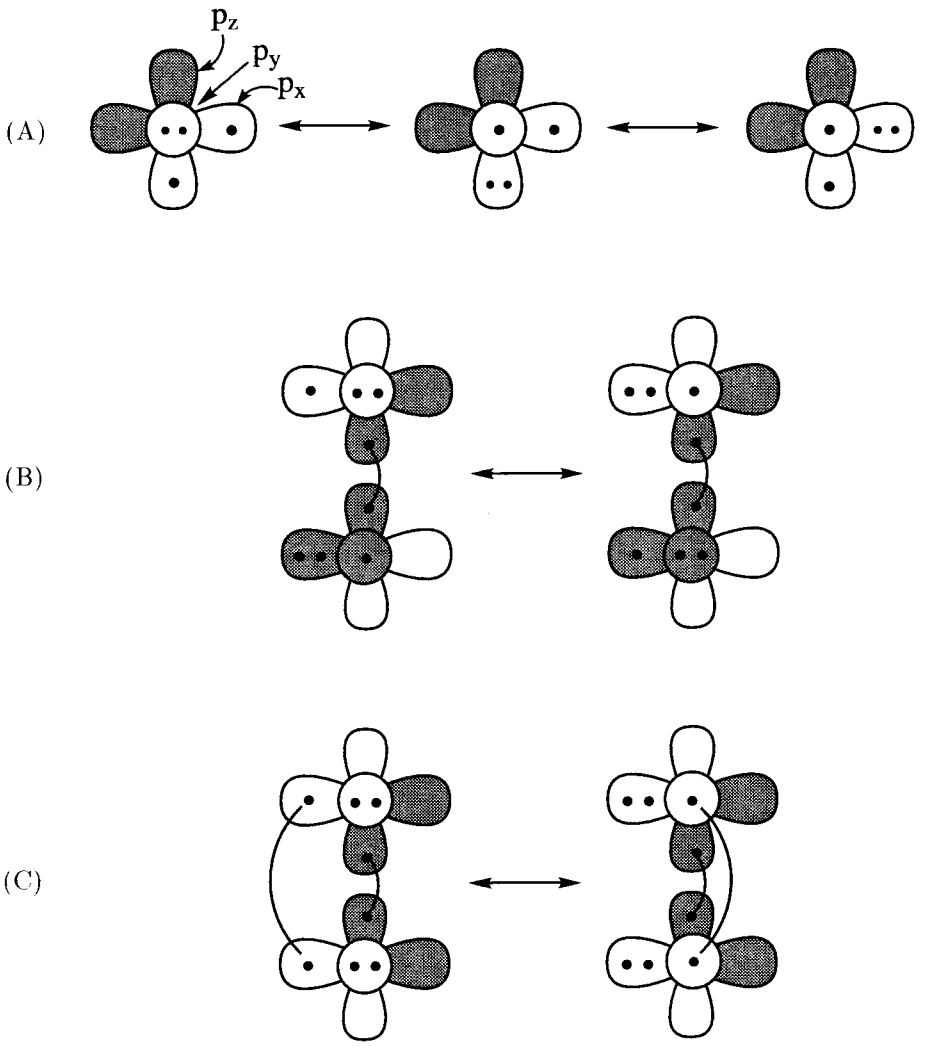

Figure 1.7: GVB diagrams. (A) oxygen atom; (B) triplet ground state of O_2; (C) singlet excited state of O_2.

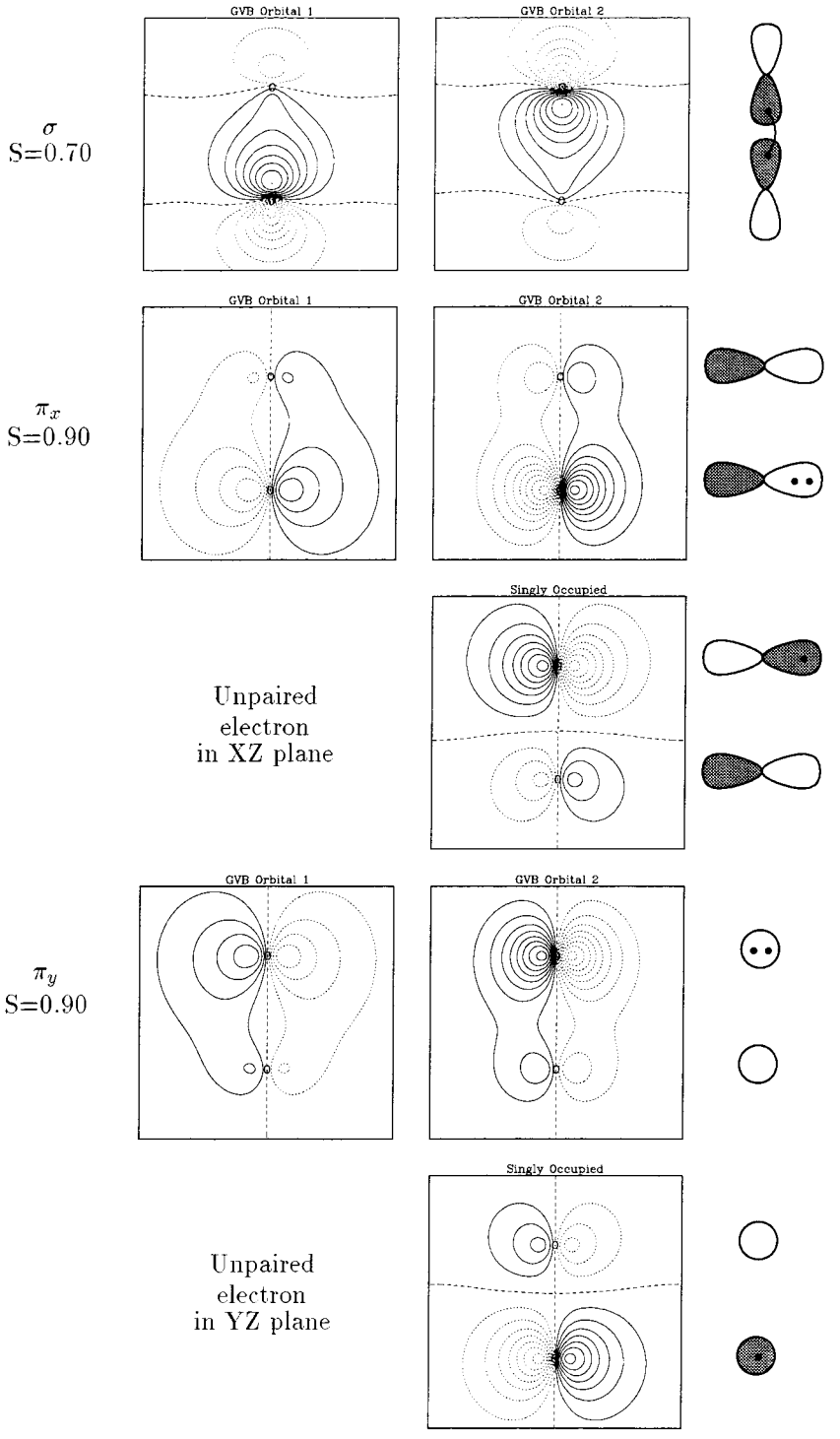

Figure 1.8: One of the two equivalent resonance structures describing O_2 at the GVB(3/6) level. The other resonance structure is obtained by interchanging the x and y coordinates.

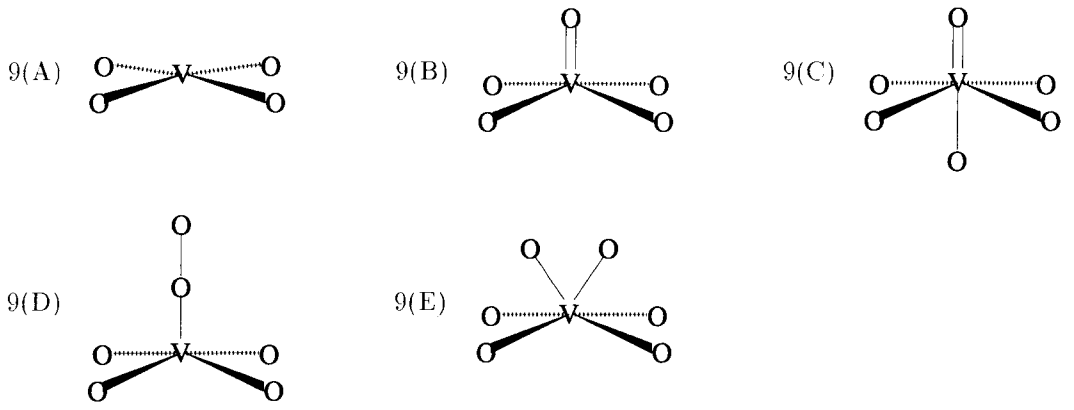

Figure 1.9: Cluster models containing one vanadium center for which it was possible to optimize the geometry. All attempts to bind O_2 to cluster 9(B) failed.

Table 1.1: Bond energies in kcal/mol of the relevant bonds for the oxidation of clusters containing one vanadium atom.

Reaction			MP2[a]	DFT-BLYP[b]
9(A)+O	$\longrightarrow$	9(B)	175	161
9(B)+O	$\longrightarrow$	9(C)		18
9(B)+O	$\longrightarrow$	9(D)		25
9(B)+O	$\longrightarrow$	9(E)		43
9(B)+O_2	$\longrightarrow$	9(B)+O_2	not bound	not bound

[a] refers to the MP2 optimized geometry of the H-clusters.
[b] refers to the DFT-BLYP optimized geometry of the P-clusters.

1.3 Clusters Containing One Vanadium Atom

In this section we discuss possible reactions involving only one vanadium center. The clusters used to mimic the catalyst are the same used to analyze the electronic structure of the vanadyl bond and are reported in Figure 1.2. The complete list of the clusters used is given in Figure 1.9 and a summary of the results obtained is in Table 1.1.

Cluster 9(A) was studied to assess how the energetics are affected by the cluster termination and by the computational method used.

In order to bind one oxygen atom to cluster 9(B), we considered the attacking positions described in Figures 1.9(C-E).

For geometry 9(C) two adsorption mechanisms were considered. First, the unpaired vanadyl electron was transferred to the incoming oxygen, giving rise to an overall doublet spin state. Second, the unpaired electron was left on the vanadium and the spin density of the incoming oxygen was delocalized to the vanadyl bond, originating an overall quartet spin state. The charge-transfer doublet state gave energies higher than the energies of the dissociated cluster 9(B) plus an isolated oxygen atom, indicating that the compound is not stable. The energies reported in Table 1.1 refer to the quartet state.

The most stable wavefunction for geometry 9(D) corresponds to the sum of an oxygen molecule

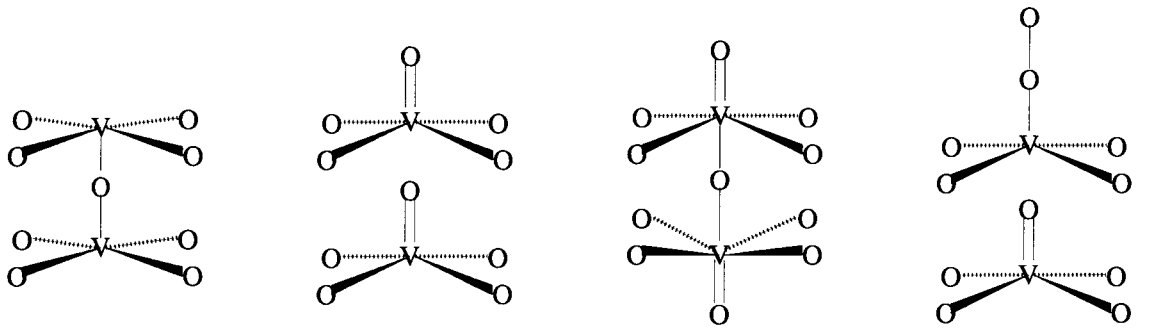

10(A) 10(B) 10(C) 10(D)

Figure 1.10: Cluster models containing two coaxial vanadium centers for which the geometry was optimized. All attempts to bind O_2 to cluster 10(B) failed. The distance between the two equatorial planes was fixed at the bulk interplanar distance of 3.86Å.[5, 16, 17]

Table 1.2: Bond energies in kcal/mol of the relevant bonds for the oxidation of clusters containing two coaxial vanadium atoms.

Reaction			DFT-BLYP[a]
10(A)+O	$\longrightarrow$	10(B)	154
10(B)+O	$\longrightarrow$	10(C)	33
10(B)+O	$\longrightarrow$	10(D)	38
10(B)+O_2	$\longrightarrow$	10(B)+O_2	not bound

[a] refers to the DFT-BLYP optimized geometry of the H-clusters.

to cluster 9(A). The two unpaired electrons of the O_2 are singlet coupled with two π electrons on the vanadium atom.

Geometry 9(E) corresponds to the oxygen atom attacking the unpaired vanadyl electron in the vanadium d orbital perpendicular to the vanadyl bond.

All attempts to bind O_2 to cluster 9(B) failed, giving either energies higher than the dissociated system or geometries corresponding to physisorption with bond energies of less than 5 kcal/mol.

1.4 Clusters Containing Two Vanadium Atoms

Clusters containing two vanadium centers can be used to study two distinct kinds of interactions: the pairing between coaxial vanadyls on different planes and the pairing of nearest vanadyls on the same plane. In order to understand the importance of these pairings, two families of clusters were considered.

1.4.1 Pairing of Coaxial Vanadyl Groups

The pairing of coaxial vanadyls was studied using the clusters in Figure 1.10, where cluster 10(B) represents the unreacted crystal. The energetics for these clusters are reported in Table 1.2.

To understand the effect of the second layer vanadyl, we notice how the strengths of equivalent bonds changes when the second vanadyl is missing.

Table 1.3: Reaction energies in kcal/mol for the oxidation of clusters containing two neighboring vanadium atoms.

Reaction			MP2[a]	DFT-BLYP[b]
11(A)+O	—	11(B)		162
11(B)+O	—	11(C)	49	48
11(B)+O	—	11(D)	-15	-1
11(B)+O	—	11(E)	87	65
11(B)+O_2	—	11(B)+O_2	not bound	not bound

[a] refers to the MP2 optimized geometry of the H-clusters.
[b] refers to the DFT-BLYP optimized geometry of the P-clusters.

According to our calculations at the DFT-BLYP level, the original surface vanadyl bond, for instance, is weakened by 6 kcal/mol (it is worth 160 kcal/mol for the one-vanadium cluster and 154 kcal/mol in the two-vanadium cluster). Although the error associated with the bond energies is of the same order of magnitude of the change, the direction of the change is meaningful as long as the comparison is made using the same computational technique for both cases.

More pronounced effects are observed when the original cluster 10(B) is reacted with atomic oxygen. For the geometries considered, the extra stabilization due to the second layer vanadyl veries between 12 and 23 kcal/mol. This indicates that the second layer vanadyl is likely to play a significant role in stabilizing reactive species on the surface.

The stabilization effect of the third and subsequent layers cannot be estimated quantitatively without considering larger clusters. At the qualitative level, however, we estimate the third layer stabilization to be small compared to the second layer one. The main energy gain, in fact, comes from the fact that the highly energetic extra oxygen can interact with the neighboring vanadyls. In cluster 9(C), for instance, the extra oxygen can interact with one vanadium center whereas in cluster 10(C) it can interact with two and is hence more stable. In a three vanadium cluster, the extra oxygen would have essentially the same electronic stabilization as in the two vanadium cluster, except for a better delocalization of partial charges and radical character, so the extra stabilization would be minor.

When we reacted cluster 10(B) with molecular oxygen we could find no stable products. As was the case for the one-vanadyl clusters, all resulting species are either more energetic than the reactants or correspond to weak physisorption.

1.4.2 Pairing of Neighboring Vanadyl Groups

The pairing effect of neighboring vanadyl groups was studied using the clusters in Figure 1.11. Cluster 11(B) represents the unreacted catalyst and the energetics for the relevant reactions are reported in Table 1.3.

When atomic oxygen reacts with cluster 11(B) attacking the vanadium end of one of the vanadyl groups, the vanadyl oxygen moves to a bridging position between the two vanadium atoms, as

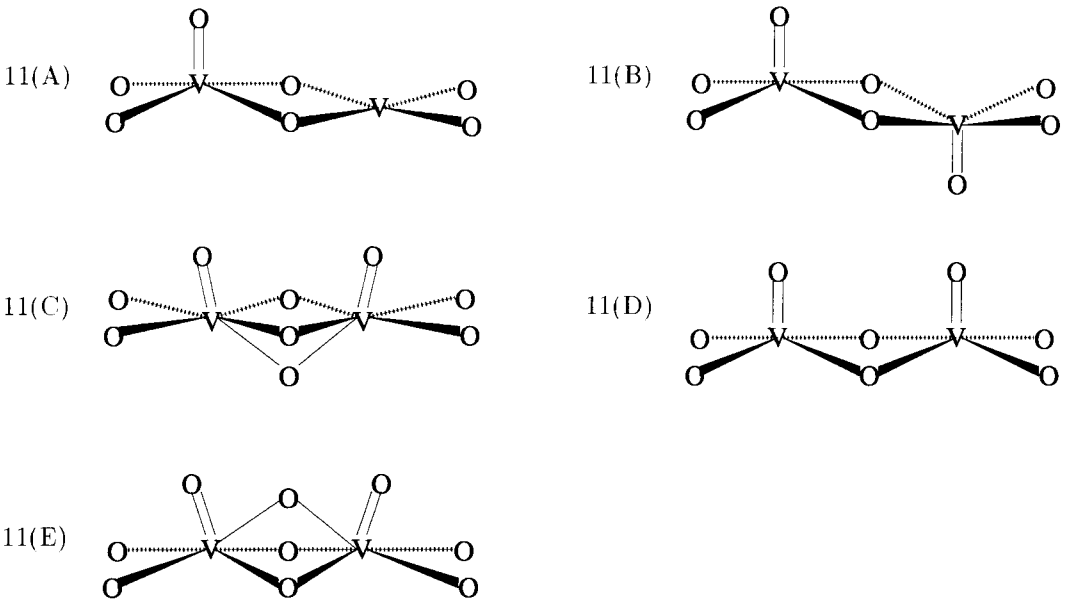

Figure 1.11: Cluster models containing two neighboring vanadium centers for which the geometry was optimized. All attempts to bind O_2 to cluster 11(B) failed.

depicted in Figure 1.11(C). The resulting cluster contains two vanadyls and a bridging oxygen. One of the vanadyls (right in Figure 1.11(C)) is formed with the newly arrived oxygen. The two unpaired vanadyl electrons in cluster 11(B) form bonds with the bridging oxygen in cluster 11(C), so that the overall spin multiplicity is singlet and the vanadium atoms have formal oxidation state V.

Both MP2 with the H-clusters and BLYP with the P-clusters predict a binding energy of approximately 48 kcal/mol.

A more stable configuration is found assuming that all three active oxygens lie on the same side of the equatorial plane. Cluster 11(E), in fact, is predicted to be 65 or 87 kcal/mol more stable than cluster 11(B) plus atomic oxygen, depending on the computational method used. In order to obtain such a cluster, however, it would be necessary to first rearrange the geometry of cluster 11(B) to eclipse the two vanadyls, as in cluster 11(D). The net energy cost for this step is estimated to be small, but the results depend strongly on the constraints forced on the cluster.

Once again, molecular oxygen does not react with cluster 11(B).

1.5 Discussion

The computations reported in the previous two sections indicate that one- and two-vanadium clusters do not react with molecular oxygen. Two possible explanations for the discrepancy between these results and the experimental evidence have been considered. First, the activation may be due to a defect in the crystal or, second, more than two vanadyls may cooperate to activate a single oxygen

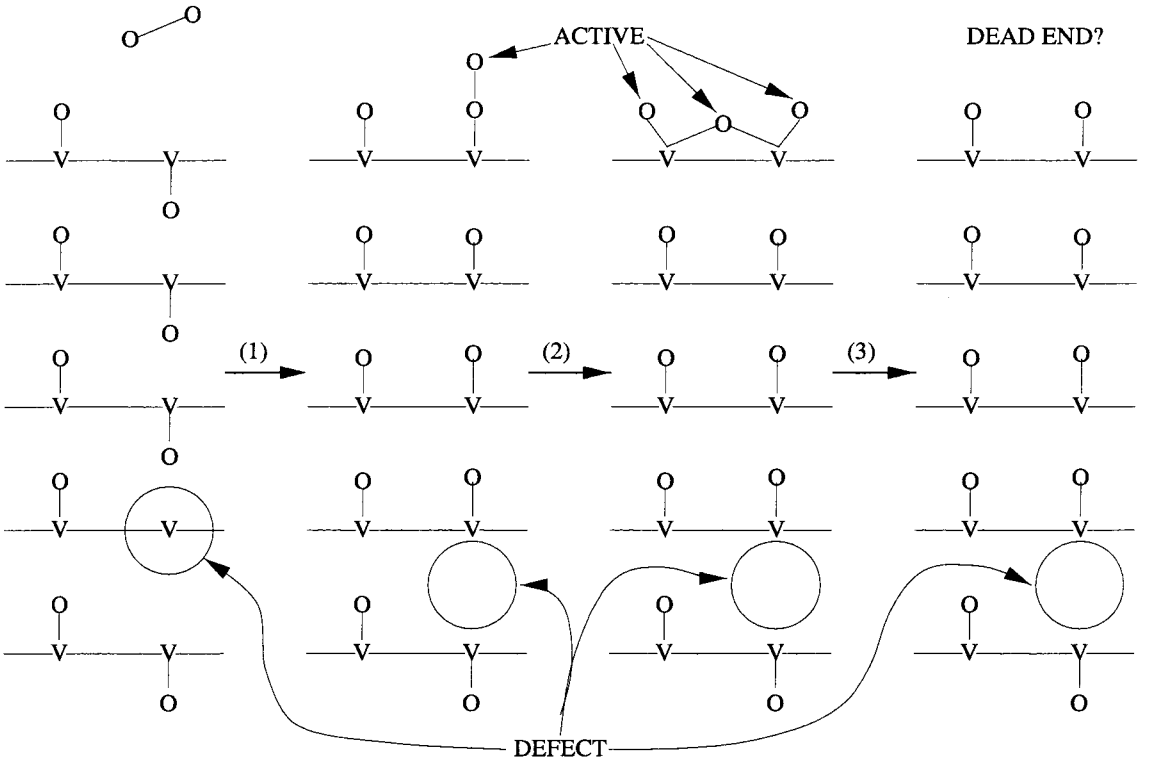

Figure 1.12: Schematic description of the activating mechanism due to a defect (oxygen vacancy) in the bulk of the crystal.

molecule.

These possibilities cannot be investigated with direct computations due to the size of the clusters, but strong suggestive evidence in favor of the second explanation can be derived from the energetics of the clusters already studied.

1.5.1 Defect Hypothesis

If a defect is to be responsible for increasing the affinity of the crystal toward oxygen, then it must involve a somewhat reduced form of the perfect crystal. The defect that would activate the catalyst the most is then an oxygen vacancy. We hence considered the vacancy of one of the vanadyl oxygens inside the crystal. As depicted schematically in Figure 1.12, the defect could activate oxygen. The energetics for the process can be estimated, if first approximation, from the results of the previous sections, and they indicate that even assuming the most favorable conditions the process cannot be catalytic.

Step (1) in Figure 1.12 requires that all the vanadyl oxygens between the defect and the surface rearrange their structure and transfer to the vanadium atom one layer closer to the vacancy. The more energy this rearrangement costs, the less favorable this route becomes. Assuming the most

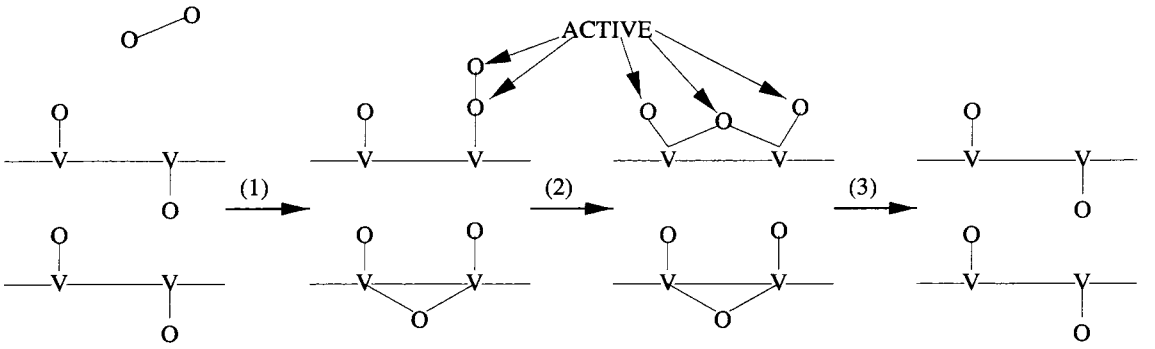

Figure 1.13: Schematic description of the activating mechanism involving the first two layers of the crystal.

favorable case, the cost will be negligible. The energy balance of step (1) is hence due to the binding of O_2 to the first layer vanadium atom, and this can be estimated from the energetics of clusters 10(A) and 10(D) to be favorable by approximately 74 kcal/mol (we assumed the $O-O$ bond energy to be 118 kcal/mol).

Similarly, from the results obtained for clusters 11(A) and 11(E), we estimate step (2) to be favorable by approximately 41 kcal/mol. If we combine the first two steps into a single elementary reaction, the net energy gain will be of 115 kcal/mol.

The removal of one of the surface oxygens will then cost approximately 66 kcal/mol, so the surface oxygens are in fact more active than molecular oxygen. The removal of a second surface oxygen, however, is expected to cost about 160 kcal/mol, as it requires the cleavage of a vanadyl bond.

This mechanism, therefore, leads to a stable form of the crystal where the initially reduced vanadium is oxidized via the inversion of a chain of vanadyl bonds. This form is expected to be almost as stable as the perfect crystal, so the presence of the defect cannot activate O_2 catalytically.

1.5.2 Four Vanadyl Hypothesis

According to our computations, each pair of vanadyls can adsorb one oxygen atom but not two. In order to activate molecular oxygen, it may then be necessary to consider at least four vanadyl centers. The distance between pairs of vanadyl centers on the surface is too large for an oxygen molecule to react with four vanadium atoms at the same time (the closest surface vanadia of different pairs are 4.9 Å apart). It is possible, however, that the first two layers of the crystal adsorb one oxygen each as suggested in Figure 1.13.

The proposed mechanism is the following. As O_2 attacks the exposed surface vanadium, the corresponding vanadyl oxygen is pushed onto the second layer, which stores it by moving one of the oxygens to a bridging position. From the energetics for clusters 11(B), 11(C), 10(A), and 10(D), we estimate step (1) in Figure 1.13 to be uphill by 32 kcal/mol.

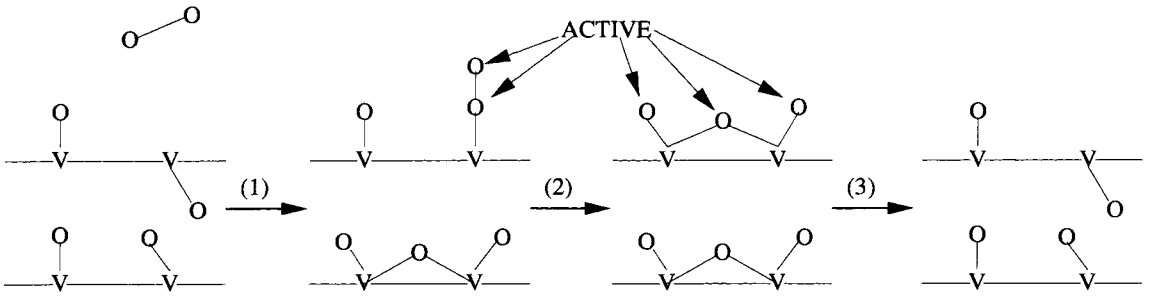

Figure 1.14: Schematic description of the activating mechanism by a speculated form of the equilibrated catalyst.

Step (2) in Figure 1.13 is expected to be downhill by between 27 and 47 kcal/mol, depending on the computational method and the cluster termination considered.

The combined first two steps can be envisioned as a single elementary reaction with a balance between 15 kcal/mol downhill and 5 kcal/mol uphill. Due to the large error bar associated to these numbers, it is not clear whether the process can actually happen and further investigations are required to give better estimates of the energies, but the results suggest that this mechanism is at least plausible.

Once dioxygen has been adsorbed, the surface oxygens must be removed one at a time to estimate their reactivity. The first surface oxygen to be removed is bound by approximately 65 kcal/mol and the second one by 48 kcal/mol. Both oxygen atoms are thus more active than dioxygen. The removal of two surface oxygens restores the crystal to the starting configuration and hence the activation can be repeated catalytically.

The intermediates considered in Figure 1.13 are not the most stable forms of oxidized catalyst. A net stabilization of between 17 and 38 kcal/mol would result for the intermediates considered if the bridging oxygen on the second layer was on the other side of the equatorial atoms, as depicted in Figure 1.14. At the same time the starting structure would result somewhat destabilized, making the formation of the first $V - O_2$ bond more favorable.

It is conceivable that during the activation of the catalyst, which requires several weeks and millions of catalytic cycles, the second layer of the crystal displaces one of its oxygens to effectively transfer the bridging oxygen closer to the surface. The experimentally observed rate determining step, in fact, is the activation of the alkane molecule, indicating that during the reaction the catalyst spends most of the time in the oxidized state.

This would bring the first step suggested within a plausible energy balance and would make the combined first two steps definitely favorable.

1.5.3 Conclusions

With first principles quantum chemistry techniques we have studied the chemisorption of dioxygen on the catalytic surface of vanadyl phyrophosphate. These computations indicate that the adsorption mechanism must involve at least two layers of the crystal. We show that a defect in the bulk of the catalyst is not likely to be responsible for the catalytic activation of molecular oxygen. We propose an activation mechanism involving the top two layers of the catalyst which is consistent with the experimental data available.

1.6 Calculational Details

Basis Sets

For H-clusters we used the STO-3G minimal basis set[18] on the equatorial atoms, Los Alamos Core-Valence Effective Core Potential (ECP) with double-ζ basis set[19] on the vanadium atoms, and 6-31G* double-ζ plus polarization basis set[20] on the active oxygens.

For P-clusters we used Los Alamos Core-Valence ECP with double-ζ basis set[19] on the vanadium atoms, 6-31G double-ζ basis set[20] on the equatorial atoms and 6-31G* double-ζ plus polarization basis set[20] on the active oxygens.

Methods

The choice of the computational methods was based on the following considerations. The simplest ab-initio method that correctly describes the dissociation of both the O_2 molecule and the vanadyl bond is MP2. Due to its high cost, we performed computations at the MP2 level only for some of the H-clusters. The results are provided in Tables 1.1 and 1.3 when available.

We tested several DFT methods on small molecules for which the experimental bond energies and geometries are known. The molecules considered are: VO, VCl, VBr, and $VOCl_3$. We included in the study the following functionals:

GGAII: generalized gradient functional with Slater local exchange,[21] Perdew-Wang 1991 local correlation and Perdew-Wang 1991 GGAII non-local exchange and non-local correlation functionals.[22]

BLYP: generalized gradient functional with Slater local exchange.[21] Becke's 1988 non-local gradient correction to exchange[23] and Lee-Yang-Parr non-local correlation functionals.[24]

B3LYP: hybrid functional using exact HF, Slater local exchange,[21] and Becke's 1988 non-local gradient correction[23] for the exchange and Lee-Yang-Parr local and non-local functionals[24] for the correlation.

The study revealed a clear deficiency of the hybrid method B3LYP, whereas the two generalized gradient methods performed both reasonably well. BLYP gave slightly better results than GGAII, so it was chosen. The importance of allowing unrestricted wavefunctions for open shell systems was studied only using BLYP. It was determined that the unrestricted description is essentially identical to the restricted one for the molecules investigated.

The restricted version of BLYP was therefore adopted to study O_2 activation.

Programs

The GVB computations were performed using our computer code. All MP2 computations and the BLYP on clusters 10(A,B,C,D) as well as the other cluster studied with two coaxial vanadium centers were performed using the GAUSSIAN commercial packages.[25] The other computations were performed using the PSGVB or JAGUAR commercial packages.[26]

Acknowledgements

The research was funded by NSF (CHE 91-100289 and ASC 92-100368). The facilities of the MSC are also supported by grants from DOE-AICD, Allied-Signal Corp., Asahi Chemical, Asahi Glass, BP Chemical, Chevron Petroleum Technology, BF Goodrich, Vestar, Xerox, Hughes Research Lab., and Beckman Institute.

Bibliography

[1] Pepera, M.A.; Callahan, J.L.; Desmond, M.J.; Milberger, E.C.; Blum, P.R.; Bremer, N.J; *J. Am. Chem. Soc.* **1995**, *107*, 4883.

[2] Centi, G.; Trifirò, F.; Ebner, J.R.; Franchetti, V.M.; *Chem. Rev.* **1988**, *88*, 55.

[3] Centi, G.; *Catal. Today* **1993**, *16*, 1.

[4] Centi, G.; *Catal. Today* **1993**, *16*, 5.

[5] Ebner, J.R.; Thompson, M.R.; *Catal. Today* **1993**, *16*, 51.

[6] Okuhara, T.; Misono, M.; *Catal. Today* **1993**, *16*, 61.

[7] Trifirò, F.; *Catal. Today* **1993**, *16*, 91.

[8] Bordes, E.; *Catal. Today* **1993**, *16*, 27.

[9] Zhang, Y.; Sneeden, R.P.A.; Volta, J.C.; *Catal. Today* **1993**, *16*, 39.

[10] Hodnet, B.K.; *Catal. Today* **1993**, *16*, 131.

[11] Matsumura, I.; *Catal. Today* **1993**, *16*, 123.

[12] Ye, D.; Satsuma, A.; Hattori, T.; Murakami, Y.; *Catal. Today* **1993**, *16*, 113.

[13] Schiøtt, B.; Jørgensen, K.A.; *Catal. Today* **1993**, *16*, 79.

[14] Schuurman, Y.; Gleaves, J.T.; Ebner, J.R.; Mummey, M.J.; in *New Developments in Selective Oxidation* (Cortès Corberàn and Vic Bellòn Eds. 1993).

[15] Moss, B.J.; Goddard III, W.A.; *J. Chem. Phys.* **1975**, *63*, 3523.

[16] Centi, G.; Trifirò, F.; Busca, G.; Ebner, J.; Gleaves, J.; *Faraday Discuss. Chem. Soc.* **1989**, *87*, 215.

[17] Johnson, J.W.; Johnston, D.C.; Jacobson, A.J.; Brody, J.F.; *J. Am. Chem. Soc.* **1984**, *106*, 8123.

[18] Hehre, W.J.; Stewart, R.F.; Pople, J.A.; *J. Chem. Phys.***1969**, *51*, 2657. Hehre, W.J.; Ditchfield, R.; Stewart, R.F.; Pople, J.A.; *J. Chem. Phys.***1970**, *52*, 2769. Collins, J.B.; Schleyer, P. von R.; Binkley, J.S.; Pople, J.A.; *J. Chem. Phys.***1976**, *64*, 5142. Pietro, W.J.; Levi, B.A.; Hehre, W.J.; Stewart, R.F.; *Inorg. Chem.***1980**, *19*, 2225. Pietro, W.J.; Blurock, E.S.; Hout, R.F.; Hehre, W.J.; DeFrees, D.J.; Stewart, R.F.; *Inorg. Chem.***1980**, *20*, 3650.

[19] Hay, P.J.; Wadt, W.R.; *J. Chem. Phys.***1985**, *82*, 299.

[20] Ditchfield, R.; Hehre, W.J.; Pople, J.A.; *J. Chem. Phys.***1971**, *54*, 724. Hehre, W.J.; Pople, J.A.; *J. Chem. Phys.***1972**, *56*, 4233. Binkley, J.S.; Pople, J.A.; *J. Chem. Phys.***1977**, *66*, 879. Hariharan, P.C.; Pople, J.A.; *Theor. Chim. Acta***1973**, *28*, 213. Hehre, W.J.; Ditchfield, R.; Pople, J.A.; *J. Chem. Phys.***1972**, *56*, 2257. Francl, M.M.; Pietro, W.J.; Hehre, W.J.; Binkley, J.S.; Gordon, M.S.; DeFrees, D.J.; Pople, J.A.; *J. Chem. Phys.***1982**, *77*, 3654.

[21] Slater, J.C.; *Quantum Theory of Molecules and Solids, Vol. 4: The Self-Consistent Field for Molecules and Solids.* (McGraw-Hill, New York, 1974).

[22] Perdew, J.P. in *Electronic Structure Theory of Solids,* Zieshe and Eshrig eds. (Akademie Verlag, Berlin 1991). Perdew, J.P.; Chevary, J.A.; Vosko, S.H.; Jackson, K.A.; Pederson, M.R.; Singh, D.J.; Fiolhais, C.; *Phys. Rev. B***1992**, *46*, 6671.

[23] Becke, A.D.; *Phys. Rev. A***1988**, *38*, 3098.

[24] Lee, C.; Yang, W.; Parr, R.G.; *Phys. Rev. B***1988**, *37*, 785, implemented as described in Miehlich, B.; Savin, A.; Stoll, H.; Preuss, H.; *Chem. Phys. Lett.***1989**, *157*, 200.

[25] *Gaussian 92/DFT*, Revision F.4, Frisch, M.J.; Trucks, G.W.; Schlegel, H.B.; Gill, P.M.W.; Johnson, B.G.; Wong, M.W.; Foresman, J.B.; Robb, M.A.; Head-Gordon, M.; Replogle, E.S.; Gomperts, R.; Andres, J.L.; Raghavachari, K.; Binkley, J.S.; Gonzalez, C.; Martin, R.L.; Fox, D.J.; Defrees, D.J.; Baker, J.; Stewart, J.P.P; Pople, J.A.; Gaussian, Inc., Pittsburgh, PA, 1993. *Gaussian 94*, Revision B.3, Frisch, M.J.; Trucks, G.W.; Schlegel, H.B.; Gill, P.M.W.; Johnson, B.G.; Robb, M.A.; Cheeseman, J.R.; Keith, T.; Petersson, G.A.; Montgomery, J.A.; Raghavachari, K.; Al-Laham, M.A.; Zakrzewski, V.G; Ortiz, J.V.; Foresman, J.B.; Peng, C.Y.; Ayala, P.Y.; Chen, W.; Wong, M.W.; Andres, J.L.; Replogle, E.S.; Gomperts, R.; Martin, R.L.; Fox, D.J.; Binkley, J.S.; Defrees, D.J.; Baker, J.; Stewart, J.P.P; Head-Gordon, M.; Gonzalez, C.; Pople, J.A.; Gaussian, Inc., Pittsburgh, PA, 1995.

[26] Jaguar 3.0, Schrodinger, Inc., Portland, Oregon, 1997.

Chapter 2 GVB-RCI: a Reliable MCSCF Wavefunction for Large Systems

Abstract

We have developed a version of Generalized Valence Bond (GVB) that overcomes the major weakness of the perfect pairing approximation without requiring a full transformation of the integrals at each step of the self-consistent orbital optimization. The method, called Generalized Valence Bond-Restricted Configuration Interaction (GVB-RCI), describes properly the dissociation of up to triple bonds and provides smooth potential energy surfaces for most chemical reactions. The wavefunctions obtained are a good starting point for more sophisticated computational techniques. A few simple examples of computations are included to illustrate the capabilities of the method.

2.1 Introduction

Accurate and reliable potential energy surfaces are essential for assessing chemical reaction rates and mechanisms. A common approach to compute *ab initio* energies is to start from the Hartree-Fock (HF) wavefunction (either restricted or unrestricted) and to correct the result with a number of standard methods to estimate the correlation energy. Such methods include partial configuration interaction (CI) expansions and perturbative treatments (e.g., MP2).

This approach has two major shortcomings: (1) the correlation energy (i.e., the difference between the HF and the Full CI energy for a given basis set) depends strongly on the nuclear position, being in general small close to equilibrium geometry and big as one or more bonds are stretched, broken, and reformed. The post HF corrections, therefore, need to be accurate and expensive in order to correctly describe the regions where the correlation energy is big. (2) Near the transition states for forbidden reactions, the HF potential energy corresponding to a given spin state contains nonphysical edges (discontinuities in the gradient). This problem generally remains for the higher level treatments.

A convenient way to handle these problems is to use as starting point for the correlation treatment a better self-consistent wavefunction, including just enough correlation to correctly describe bond dissociations and transition states. Several multiconfiguration self-consistent field (MCSCF) wavefunctions[1, 2] are appropriate, ranging from a simple one-pair GVB calculation for a single bond dissociation to larger complete active space self-consistent field (CASSCF)[3] for more complicated systems. In general, including additional configurations in the self-consistent field (SCF) is more

expensive. It is therefore important to select a wavefunction that has just the right amount of correlation.

The GVB-PP (Generalized Valence Bond with Perfect Pairing approximation)[4, 5] wavefunction is excellent in describing reactions involving breaking and formation of single bonds, as it does not require expensive integral transformations at each step of the SCF procedure. GVB-PP, however, has similar problems to HF in describing multiple bonds and forbidden reactions. More general forms of GVB[5], as well as most other forms of MCSCF[1, 2, 3] (including CASSCF), require a complete transformation of the four center integrals at each step of the SCF, making the cost increase very rapidly with the size of the system.

Here we present a method to obtain self-consistent wavefunctions at a level that is intermediate between the most general GVB and the GVB-PP. The method, called GVB-RCI (GVB with the Restricted CI approximation[6]), includes the minimum number of configurations to correctly describe dissociation for up to triple bonds and transition states involving few electrons. Although the same approach can be generalized to arbitrary bond order and number of electrons, the current version should be able to describe properly most of the interesting molecules that require going beyond HF or GVB-PP wavefunctions but are too big for CASSCF treatments. Because of the very limited number of configurations included, only a partial integral transformation is required at each self-consistent step. The cost of the method scales well with the size of the system, making this approach promising for future applications to extensive systems.

Section 2 outlines the method and derives the main formulas used. Section 3 reports results obtained for simple reactions and compares them with other computational methods.

2.2 Theoretical Method

2.2.1 Formalism

We use lower case letters a, b, ..., i, j, ... to indicate orthogonal orbitals. The orbitals in the GVB space (or *active* orbitals) are grouped into pairs. The two orbitals of each pair are denoted as g for the bonding orbital (good) and u for the antibonding orbital (ungood) which does not imply that the pair has symmetry (both orbitals can have the same symmetry). We use capital letters to indicate the pair number; for instance, g_I indicates the g orbital of pair I. The symbol C indicates a numerical coefficient.

2.2.2 GVB-PP Wavefunction

The GVB-PP wavefunction describes each pair of active electrons with two variationally optimized overlapping (i.e., nonorthogonal) orbitals

$$\Psi^{GVB} = [\varphi_a(1)\phi_b(2) + \varphi_b(1)\varphi_a(2)](\alpha\beta - \beta\alpha)$$

Nonactive orbitals are treated as doubly occupied (as in the HF level) or high spin open shell.

It is convenient to carry out the GVB computations in terms of orthogonal orbitals, obtained by rewriting each GVB pair in the natural orbital representation

$$\Psi^{NO} = [C^g gg - C^u uu](\alpha\beta - \beta\alpha)$$

Thus, GVB-PP wavefunction has the form

$$\Psi^{GVB-PP} = [\{core\}\{open\}\Psi^{NO}(1,2)\Psi^{NO}(3,4)\ldots] \tag{2.1}$$

where $\{core\}$ and $\{open\}$ are products of RHF like orbitals with double and single occupancy, respectively. All singly-occupied orbitals are assumed to have spin α. This is a special case of the full GVB wavefunction, since the full GVB wavefunction allows all possible spin couplings of the active orbitals, whereas Eq. (2.1) has just a single valence bond (or perfect pairing) coupling of the spins. The GVB-PP wave function builds in *static correlation* between electrons in each GVB pair, by allowing them to each occupy their own orbital, on the average staying farther apart from one another than if they were restricted to occupy the same spatial orbital.

Upon homolytic bond dissociation, the two electrons forming the bond can smoothly follow the two fragments as they separate. However, for multiple bonds the optimal wavefunction should generally dissociate to two high spin fragments, but GVB-PP forces each electron within a pair to have equal probability of having spin α or β, regardless of the spin in the other bond pairs. Consequently, GVB-PP leads to a mixture of high and low spin components. Generally, previous GVB calculations for dissociation of multiple bonds used the GVB-PP representation but added a Full CI among the GVB orbitals (GVB-CI). This includes the proper spin configuration and generally leads to a good dissociation. In some cases, GVB3 was used to optimize the orbital for the GVB-CI wavefunction, leading to proper dissociation. An efficient alternative was the Correlation Consistent CI method (CC-CI) which incorporates all correlations that directly affect the bond dissociation.

For reactions in which pairs of electrons must exchange partners, GVB-PP often cannot do the exchange smoothly, leading to cusps in potential energy surface. Again this can be handled with GVB-CI or CC-CI but at some loss in interpretation.

2.2.3 GVB-RCI

In order to overcome the weakness of GVB-PP, it is necessary to include configurations to allow electrons in different GVB pairs to be singlet paired and hence electrons within the same GVB pair to be triplet paired. The simplest way to do this is to include configurations where two separate GVB pairs have their spins coupled into a triplet while the overall spin state (for the two GVB pairs) remains a singlet (the GF spin coupling in the original SOGI version of GVB theory).

To describe the resulting wavefunction, we define the following intermediate symbols to indicate GVB pairs and RCI groups of four orbitals from two GVB pairs

$$(gvb)_I = (C_I^g g_I g_I - C_I^u u_I u_I)\Theta_1 \qquad (C_I^g)^2 + (C_I^u)^2 = 1 \tag{2.2}$$

$$(rci)_{IJ} = (g_I u_I g_J u_J)\Theta_2(C_{IJ}^s, C_{IJ}^t) \qquad (C_{IJ}^s)^2 + (C_{IJ}^t)^2 = 1 \tag{2.3}$$

where the spin functions Θ are:

$$\Theta_1 = \frac{1}{\sqrt{2}}(\alpha\beta - \beta\alpha)$$

$$\Theta_2 = \frac{C_{IJ}^s}{2}(\alpha\beta - \beta\alpha)(\alpha\beta - \beta\alpha) + \frac{C_{IJ}^t}{\sqrt{12}}[2\alpha\alpha\beta\beta + 2\beta\beta\alpha\alpha - (\alpha\beta + \beta\alpha)(\alpha\beta + \beta\alpha)]$$

$$= \frac{C_{IJ}^t}{\sqrt{3}}(\alpha\alpha\beta\beta + \beta\beta\alpha\alpha) + \left(\frac{C_{IJ}^s}{2} - \frac{C_{IJ}^t}{\sqrt{12}}\right)(\alpha\beta\alpha\beta + \beta\alpha\beta\alpha) - \left(\frac{C_{IJ}^s}{2} + \frac{C_{IJ}^t}{\sqrt{12}}\right)(\alpha\beta\beta\alpha + \beta\alpha\alpha\beta)$$

It is also convenient to define the following terms

$$\Psi^{PP} = |\{core\}(gvb)_1 \ldots (gvb)_n >$$

$$\Psi_{12}^{RCI} = |\{core\}(rci)_{12}(gvb)_3 \ldots (gvb)_n >$$

$$\Psi_{IJ}^{RCI} \quad \text{by analogy with } \Psi_{12}^{RCI}$$

Ψ^{PP} has the form of a traditional GVB-PP wavefunction. Ψ_{IJ}^{RCI} represents the same wavefunction where two electrons from pairs I and J have had their spins recoupled. Since in Ψ_{IJ}^{RCI} the four electrons from pairs I and J occupy four different orbitals, we only require that the overall spin state is a singlet.

The GVB-RCI wavefunction with RCI correlation on N_r GVB pairs is

$$\Psi = C_0\Psi^{PP} + \sum_{I,J>I}^{N_r} C_{IJ}\Psi_{IJ}^{RCI} \qquad C_0^2 + \sum_{I,J>I}^{N_r} (C_{IJ})^2 = 1 \tag{2.4}$$

It is convenient to define

$$C_{II} = 0 \qquad C_{JI} = C_{IJ}$$

so that Eq. (4) can be rewritten as

$$\Psi = C_0\Psi^{PP} + \frac{1}{2}\sum_{I,J}^{N_r} C_{IJ}\Psi_{IJ}^{RCI} \qquad\qquad C_0^2 + \frac{1}{2}\sum_{I,J}^{N_r}(C_{IJ})^2 = 1 \tag{2.5}$$

We also define the *perfect pairing density* for pair I as

$$\Gamma_I = 1 - \sum_J C_{IJ}^2$$

Γ_I is a measure of the importance of the PP coupling within pair I. If pair I is not included in the RCI treatment, then all coefficients C_{IJ} are null and $\Gamma_I = 1$.

2.2.4 Total Energy

The energy associated with wavefunction (2.5) is

$$E = \sum_i 2f_i h_i + \sum_{i,j}(a_{ij}J_{ij} + b_{ij}K_{ij}) + \sum_{I,J}[r_{IJ}(g_I g_J|u_I u_J) + s_{IJ}(g_I u_J|u_I g_J) + t_{IJ}(g_I u_I|g_J u_J)] \tag{2.6a}$$

where f is given by

$$\begin{aligned} &f_i = 1 && \text{if } i \text{ is a core orbital} \\ &f_i = \tfrac{1}{2} && \text{if } i \text{ is an open shell orbital} \\ &f_i = \Gamma_I C_i^2 + \tfrac{1}{2}(1-\Gamma_I) && \text{if } i \in I \text{ where } I \text{ is a GVB pair} \end{aligned} \tag{2.6b}$$

The a_{ij} and b_{ij} are given by

$$\begin{aligned} a_{ij} &= 2f_i f_j \\ b_{ij} &= -f_i f_j \end{aligned} \tag{2.6c}$$

except that

(i) if i and j are both open shell orbitals, then $b_{ij} = -\frac{1}{2}$

(ii) if i is a pair orbital, then $\begin{cases} a_{ii} = \Gamma_I C_i^2 \\ b_{ii} = 0 \end{cases}$

(iii) if i and j are in the same pair I, then $\begin{cases} a_{ij} = \frac{1}{2}(1-\Gamma_I) \\ b_{ij} = -\Gamma_I C_i C_j - \frac{1}{2}\sum_J C_{IJ}^2[(C_{IJ}^t)^2 - (C_{IJ}^s)^2] \end{cases}$

(iv) if $i \in I$, $j \in J \neq I$ and $I, J \in RCI$, then

$$a_{ij} = (\Gamma_I + \Gamma_J + C_{IJ}^2 - 1)2C_i^2C_j^2 + (1 - \Gamma_I - C_{IJ}^2)C_j^2 + (1 - \Gamma_J - C_{IJ}^2)C_i^2 + \tfrac{1}{2}C_{IJ}^2$$

(v) if $i, j \in RCI$ with $|i - j|$ even, then

$$b_{ij} = -(\Gamma_I + \Gamma_J + C_{IJ}^2 - 1)C_i^2C_j^2 - \tfrac{1}{2}(1 - \Gamma_I - C_{IJ}^2)C_j^2 - \tfrac{1}{2}(1 - \Gamma_J - C_{IJ}^2)C_i^2 + \\ -C_{IJ}^2\left\{\tfrac{1}{4}[(C_{IJ}^s)^2 - (C_{IJ}^t)^2] - \tfrac{\sqrt{3}}{2}C_{IJ}^sC_{IJ}^t\right\}$$

(vi) if $i, j \in RCI$ with $|i - j|$ odd. then

$$b_{ij} = -(\Gamma_I + \Gamma_J + C_{IJ}^2 - 1)C_i^2C_j^2 - \tfrac{1}{2}(1 - \Gamma_I - C_{IJ}^2)C_j^2 - \tfrac{1}{2}(1 - \Gamma_J - C_{IJ}^2)C_i^2 + \\ -C_{IJ}^2\left\{\tfrac{1}{4}[(C_{IJ}^s)^2 - (C_{IJ}^t)^2] + \tfrac{\sqrt{3}}{2}C_{IJ}^sC_{IJ}^t\right\}$$

The r_{IJ}, s_{IJ}, and t_{IJ} are given by

$$\begin{aligned}
r_{IJ} &= C_0C_{IJ}(C_I^gC_J^u + C_I^uC_J^g)(\sqrt{3}C_{IJ}^t + C_{IJ}^s) + \\
&\qquad -(C_I^gC_J^g + C_I^uC_J^u)\sum_K C_{IK}C_{JK}(C_{IK}^sC_{JK}^s + C_{IK}^tC_{JK}^t) \\
s_{IJ} &= C_0C_{IJ}(C_I^gC_J^g + C_I^uC_J^u)(\sqrt{3}C_{IJ}^t - C_{IJ}^s) + \\
&\qquad +(C_I^gC_J^u + C_I^uC_J^g)\sum_K C_{IK}C_{JK}(C_{IK}^sC_{JK}^s - C_{IK}^tC_{JK}^t) \\
t_{IJ} &= C_0C_{IJ}(C_I^g - C_I^u)(C_J^g - C_J^u)(2C_{IJ}^s) + (C_I^g - C_I^u)(C_J^g - C_J^u)\sum_K C_{IK}C_{JK}(2C_{IK}^sC_{KJ}^s)
\end{aligned} \tag{2.6d}$$

If I or J are treated at the PP level, then these reduce to $r_{IJ} = s_{IJ} = t_{IJ} = 0$.

We can express the energy in a more standard form

$$E = \sum_i 2f_ih_i + \sum_{i,j,k,l} c_{ijkl}(ij|kl) \tag{2.7a}$$

where the f are all zero, except

$$\begin{aligned}
f_i &= 1 && \text{if } i \text{ is a core orbital} \\
f_i &= \tfrac{1}{2} && \text{if } i \text{ is an open orbital} \\
f_i &= \Gamma_IC_i^2 + \tfrac{1}{2}(1 - \Gamma_I) && \text{if } i \in I
\end{aligned} \tag{2.7b}$$

and c_{ijkl} are all zero, except:

$$
\begin{aligned}
c_{iiii} &= a_{ii} + b_{ii} \\
c_{iijj} &= a_{ij} \\
c_{ijij} &= c_{ijji} = b_{ij}/2
\end{aligned}
$$

$$
c_{ijkl} = r_{IJ}/4 \quad \text{if} \begin{cases} i,k \in I \in RCI \text{ and } j,l \in J \in RCI \text{ with } I \neq J \text{ and } (k-i) = (l-j) \\ \text{or} \\ i,l \in I \in RCI \text{ and } j,k \in J \in RCI \text{ with } I \neq J \text{ and } (l-i) = (k-j) \end{cases} \tag{2.7c}
$$

$$
c_{ijkl} = s_{IJ}/4 \quad \text{if} \begin{cases} i,k \in I \in RCI \text{ and } j,l \in J \in RCI \text{ with } I \neq J \text{ and } (k-i) \neq (l-j) \\ \text{or} \\ i,l \in I \in RCI \text{ and } j,k \in J \in RCI \text{ with } I \neq J \text{ and } (l-i) \neq (k-j) \end{cases}
$$

$$
c_{ijkl} = t_{IJ}/4 \quad \text{if } i,j \in I \in RCI \text{ and } k,l \in J \in RCI \text{ with } I \neq J
$$

2.2.5 Orbital Optimization

In order to minimize the energy of an initial guess wavefunction with respect to orbital shapes and CI coefficients, we need to estimate the effect of rotations between orbitals and between CI coefficients. For a self-consistent optimization algorithm, it is only necessary to estimate the effects of such rotations one at the time. In particular, we can optimize the CI coefficients for a given set of orbitals, then improve the orbitals assuming the CI coefficients are fixed and iterate to convergence.

General MCSCF Treatment

To optimize the shape of the orbitals, we consider all possible pairwise rotations, assuming that they are independent.

The new (improved) orbitals $|\phi' >$ are obtained by a unitary transformation T of the old orbitals $|\phi >$. The transformation matrix is written as

$$
\mathbf{T} = \exp(\underset{\sim}{\mathbf{\Delta}})
$$

where $\mathbf{\Delta}$ is an antisymmetric matrix containing the rotation angles between the orbitals.

We optimize the rotational angles variationally, assuming that all rotations are independent. The angle Δ_{pq} must satisfy the condition

$$
\frac{\partial E}{\partial \Delta_{pq}} = 0 \tag{2.8}
$$

Upon application of the rotation

$$
|\phi'_r >= \sum_i T_{ri} |\phi_i >
$$

the energy expression (2.7) transforms as follows:

$$\begin{aligned} E' &= \sum_r 2f_r < \varphi'_r|h|\varphi'_r > + \sum_{rstu} c_{rstu}(\varphi'_r\varphi'_s|\varphi'_t\varphi'_u) = \\ &= \sum_r 2f_r \sum_{ij} T_{ri}T_{rj} < i|h|j > + \sum_{rstu} c_{rstu} \sum_{ijkl} T_{ri}T_{sj}T_{tk}T_{ul}(ij|kl) \end{aligned} \tag{2.9}$$

The energy dependence from the rotation Δ_{pq} and its derivative are

$$E(\Delta_{pq}) = E_0 + \left(\frac{\partial E}{\partial \Delta_{pq}}\right)_{\Delta_{pq}=0} \Delta_{pq} + \frac{1}{2}\left(\frac{\partial^2 E}{\partial \Delta_{pq}^2}\right)_{\Delta_{pq}=0} \Delta_{pq}^2 + \cdots \tag{2.10}$$

$$\frac{\partial E}{\partial \Delta_{pq}} = \left(\frac{\partial E}{\partial \Delta_{pq}}\right)_{\Delta_{pq}=0} + \left(\frac{\partial^2 E}{\partial \Delta_{pq}^2}\right)_{\Delta_{pq}=0} \Delta_{pq} + \cdots \tag{2.11}$$

We estimate the optimal rotation angle by truncation of the series (2.11) at the second term and imposing condition (2.8), obtaining

$$\frac{\partial E}{\partial \Delta_{pq}} = 0 \implies \Delta_{pq} = -\left(\frac{\partial^2 E}{\partial \Delta_{pq}^2}\right)^{-1}_{\Delta_{pq}=0} \left(\frac{\partial E}{\partial \Delta_{pq}}\right)_{\Delta_{pq}=0}$$

For simplicity we define

$$A_{pq} = \frac{1}{4}\left(\frac{\partial E}{\partial \Delta_{pq}}\right)_{\Delta_{pq}=0} \quad ; \quad B_{pq} = \frac{1}{4}\left(\frac{\partial^2 E}{\partial \Delta_{pq}^2}\right)_{\Delta_{pq}=0}$$

so that the estimate for the optimal rotation is

$$\Delta_{pq} = -\frac{A_{pq}}{B_{pq}}$$

Noticing that

$$(T_{rs})_{\mathbf{T}=\mathbf{I}} = \delta_{rs} \tag{2.12}$$

$$\left(\frac{\partial T_{rs}}{\partial \Delta_{pq}}\right)_{\mathbf{T}=\mathbf{I}} = \delta_{rp}\delta_{sq} - \delta_{rq}\delta_{sp} \tag{2.13}$$

$$\left(\frac{\partial^2 T_{rs}}{\partial \Delta_{pq}^2}\right)_{\mathbf{T}=\mathbf{I}} = -\delta_{pr}\delta_{ps} - \delta_{qr}\delta_{qs} \tag{2.14}$$

we can evaluate A_{pq} and B_{pq} by direct differentiation of expression (2.9) and substitution of (2.12), (2.13), and (2.14). The result is

$$A_{pq} = f_p h_{qp} - f_q h_{pq} + \sum_{jkl} [c_{pjkl}(qj|kl) - c_{qjkl}(pj|kl)] \tag{2.15}$$

$$B_{pq} = (f_q - f_p)(h_{pp} - h_{qq}) + \sum_{ijk} [-c_{pijk}(pi|jk) - c_{qijk}(qi|jk)] + \tag{2.16}$$

$$+\sum_{ij}[c_{ppij}(qq|ij) - c_{pqij}(qp|ij) - c_{qpij}(pq|ij) + c_{qqij}(pp|ij) + c_{pipj}(qi|qj) - c_{piqj}(qi|pj) +$$
$$-c_{qipj}(pi|qj) + c_{qiqj}(pi|pj) + c_{pijp}(qi|jq) - c_{pijq}(qi|jp) - c_{qijp}(pi|jq) + c_{qijq}(pi|jp)]$$

Specialization to GVB-RCI

In the case of GVB-RCI, the only nonzero coefficients in expression (2.7) are given by (2.7c).

The energy can be expressed as

$$E = \sum_{i}^{occ} 2f_i h_i + \sum_{i,j}^{occ}(a_{ij}J_{ij} + b_{ij}K_{ij}) + \sum_{i\neq j\neq k\neq l}^{RCI} c_{ijkl}(ij|kl)$$

and the variational principle imposes

$$\delta E = 4\sum_{i}^{occ}\left\langle \delta\phi_i \left| f_i h + \sum_{j}^{occ}(a_{ij}J_j + b_{ij}K_j)\right| \phi_i \right\rangle + 4\sum_{i\neq j\neq k\neq l}^{RCI} c_{ijkl}(\delta\phi_i\phi_j|\phi_k\phi_l)$$

In this case we can no longer define a Fock operator in terms of Coulomb and Exchange operators because of the four index summation in the energy expression.

Although it is still possible to define a Fock operator in terms of one electron integral operators [2], this would contain a double summation over the active space. We prefer instead to use the GVB-PP Fock operators to simplify these expressions and add the corrective terms one case at a time.

We define the GVB-PP Fock operator for orbital i as

$$F^i = f_i h + \sum_{j}^{occ}(a_{ij}J_j + b_{ij}K_j)$$

(but its self-consistent eigenfunctions do not minimize the energy).

In order to reduce the summation over the active space to a single index, we adopt the following formalism: if orbital p belongs to pair P ($p \in P$), then we call p' its partner (i.e., $p' \in P; p' \neq p$). Referring to another pair I, we call i and i' the two orbitals in the pair with the same position (g or u) as p and p', respectively.

The terms A_{pq} and B_{pq} originally described in (2.15) and (2.16) reduce to the following cases:

- If $p, q \notin RCI$ then

$$A_{pq} = < p|F^p - F^q|q >$$

$$B_{pq} = < p|F^q - F^p|p > + < q|F^p - F^q|q > + \gamma_{pq}$$

where: $\gamma_{pq} = +2(a_{pp} + a_{qq} - 2a_{pq})K_{pq} + (b_{pp} + b_{qq} - 2b_{pq})(K_{pq} + J_{pq})$

- If $p \in RCI$ and $q \notin RCI$ then

$$A_{pq} = -A_{qp} =< p|F^p - F^q|q > + \frac{1}{2}\sum_{I(\neq P)}^{RCI}\Big[t_{PI}(qp'|ii') + r_{PI}(qi|p'i') + s_{PI}(qi'|p'i)\Big]$$

$$\begin{aligned} B_{pq} = B_{qp} \quad &= \quad < p|F^q - F^p|p > + < q|F^p - F^q|q > + \gamma_{pq} + \\ &\quad -\frac{1}{2}\sum_{I(\neq P)}^{RCI}\Big[t_{PI}(pp'|ii') + r_{PI}(pi|p'i') + s_{PI}(pi'|p'i)\Big] \end{aligned}$$

- If $p \in P \in RCI$ and $q \in Q \in RCI$ then

$$\begin{aligned} A_{pq} =< p|F^p - F^q|q > \quad &+ \quad \frac{1}{2}\sum_{I(\neq P)}^{RCI}\Big[t_{PI}(qp'|ii') + r_{PI}(qi|p'i') + s_{PI}(qi'|p'i)\Big] \\ &- \quad \frac{1}{2}\sum_{I(\neq Q)}^{RCI}\Big[t_{QI}(pq'|ii') + r_{QI}(pi|q'i') + s_{QI}(pi'|q'i)\Big] \end{aligned}$$

If $q \neq p'$ then B is

$$\begin{aligned} B_{pq} = \quad = \quad & < p|F^q - F^p|p > + < q|F^p - F^q|q > + \gamma_{pq} + \\ & -\frac{1}{2}\sum_{I(\neq P)}^{RCI}\Big[t_{PI}(pp'|ii') + r_{PI}(pi|p'i') + s_{PI}(pi'|p'i)\Big] + \\ & -\frac{1}{2}\sum_{I(\neq Q)}^{RCI}\Big[t_{QI}(qq'|ii') + r_{QI}(qi|q'i') + s_{QI}(qi'|q'i)\Big] + \\ & -r_{PQ}(pq|p'q') - s_{PQ}(pp'|qq') - t_{PQ}(pq'|p'q) \end{aligned}$$

while in the special case that $q = p'$

$$\begin{aligned} B_{pq} \quad = \quad & < p|F^q - F^p|p > + < q|F^p - F^q|q > + \gamma_{pq} + \\ & -\frac{1}{2}\sum_{I(\neq P)}^{RCI}\Big[4t_{PI}(pp'|ii') + (3r_{PI} + s_{PI})(pi|p'i') + (r_{PI} + 3s_{PI})(pi'|p'i)\Big] \end{aligned}$$

- If $p \notin RCI$ and q is virtual, then

$$A_{pq} = -A_{qp} =< p|F^p|q >$$

$$B_{pq} = B_{qp} =< q|F^p|q > - < p|F^p|p > +2a_{pp}K_{pq} + b_{pp}(K_{pq} + J_{pq})$$

- If $p \in RCI$ and q is virtual, then

$$A_{pq} = -A_{qp} =< p|F^p|q > +\frac{1}{2}\sum_{I(\neq P)}^{RCI}\left[t_{PI}(qp'|ii') + r_{PI}(qi|p'i') + s_{PI}(qi'|p'i)\right]$$

$$\begin{aligned} B_{pq} = B_{qp} \quad = \quad & < q|F^p|q > - < p|F^p|p > +2a_{pp}K_{pq} + b_{pp}(K_{pq} + J_{pq}) + \\ & -\frac{1}{2}\sum_{I(\neq P)}^{RCI}\left[t_{PI}(pp'|ii') + r_{PI}(pi|p'i') + s_{PI}(pi'|p'i)\right] \end{aligned}$$

Integral Requirements

The GVB-PP calculation requires the computation of one-electron terms and the two-electron operators J and K for all occupied orbitals. The GVB-RCI requires the additional effort of computing the four-orbital integrals: $(pq|ii')$, $(pi|qi')$ and $(pi'|qi)$ where $p \in RCI$, $i, i' \in I \in RCI$ and q is any orbital (occupied or virtual).

In the general case of N orbitals and R GVB pairs involved in the RCI correlation ($2R$ orbitals), the extra cost is readily estimated as follows:

	integral types		q range		i, i' range		p range
extra cost=	3	*	N	*	R	*	2(R-1)

so the overall extra cost due to integral computations is:

$$\text{extra cost} = 6NR(R-1)$$

2.2.6 Optimization of CI Coefficients

Assuming the orbitals are frozen, the optimization of the CI coefficients can exploit all the pairwise constraint relations forced upon the coefficients by the energy expression.

In the current implementation, we optimize all the CI coefficients at each wavefunction iteration, with the following procedure. First, all the pair coefficients are optimized self-consistently, then the

spin coupling coefficients, then the CI coefficients. We repeat the cycle until all the coefficients are stable and consistent with one another.

The derivation of detailed formulas to carry out the optimization is tedious but involves no new techniques or ideas. The detailed formulas used are included in the appendix.

2.3 Applications

2.3.1 Dissociation of Multiple Bonds

We examined the dissociation of the diatomic molecules N_2 and CO. For each molecule we studied the dissociation potential energy profiles at various levels of theory, using the 6-31G* basis set.

N_2

The results for the dissociation of N_2 are summarized in Figure 2.1. As expected, RHF gives a poor description of the bond and the wrong dissociation limit. RHF gives also a bad wavefunction for the MP2 treatment, as testified by the RMP2 curve in Figure 2.1. At the next level of theory, UHF predicts a barrier of about 9.3 kcal/mol for the formation of the molecule. The MP2 treatment of the UHF (UMP2) wavefunction reduces the barrier to about 1.2 kcal/mol but it fails to eliminate it. Also, UMP2 predicts an edge close the the equilibrium geometry which is not physical.

At the GVB-PP level, the triple bond formation is barrierless, but the dissociation limit is not the ground state, as the two fragments are not in their high spin configurations. This leads to a dissociate limit 66.7 kcal/mol above the correct limit. Restricted HF leads to a limit approximately 700 kcal/mol above the dissociate limit.

Both GVB-RCI(5/5) and CASSCF give a more realistic potential energy profile. The experimental energy[7] is reported for comparison.

In order to compare the active space provided by various methods, we performed a complete active space CI on top of the GVB-PP and GVB-RCI wavefunctions. The results are reported in Figure 2.2. Notice that the commercial version of CASSCF used fails to identify the best active space for this system, missing part of the correlation between $2s$ electrons on the same nitrogen atom.

The computed bond energies are reported in Table 2.1.

CO

The results obtained for the CO molecule are summarized in Figure 2.3. While in this case the UHF result is qualitatively correct, the GVB-RCI treatment gives a substantially better result, approaching the CASSCF quality.

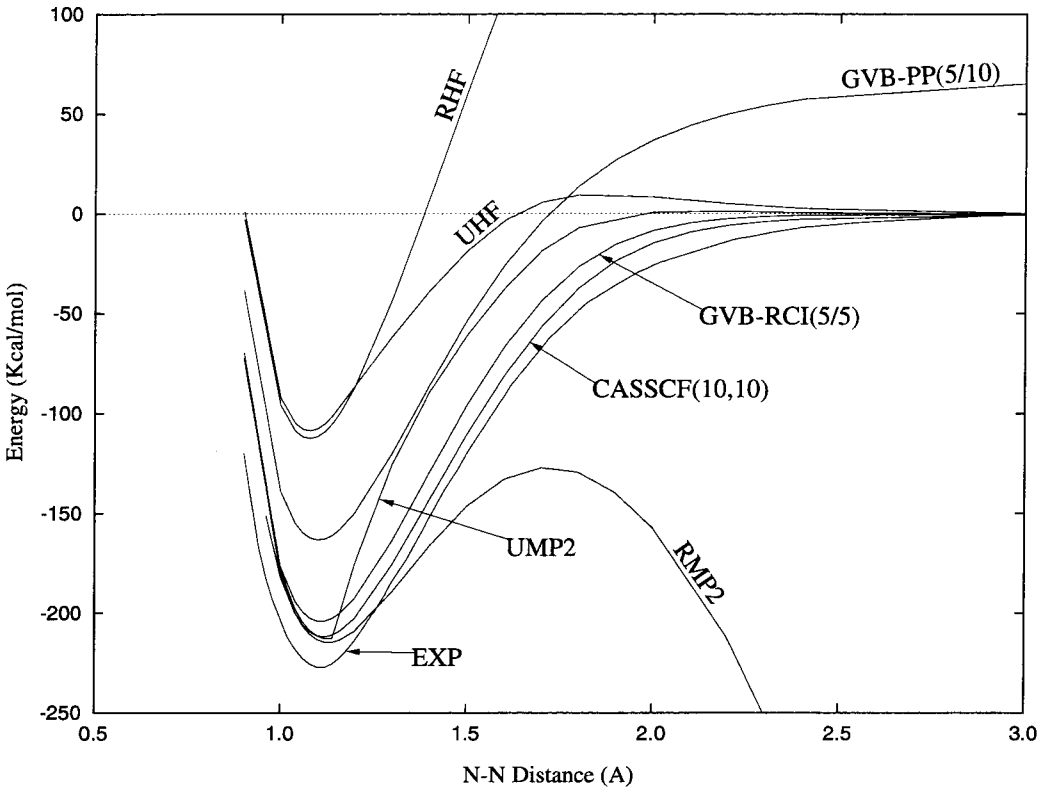

Figure 2.1: N_2 dissociation potential at various levels of theory. (All using 6-31G* basis sets.) RMP2 and UMP2 refer to the MP2 treatment on top of RHF and UHF, respectively. GVB-PP(N/M) indicates GVB-PP correlation on N pairs comprising a total of M orbitals. In the case of two orbitals per pair M=2N. GVB-RCI(N/M) indicates RCI correlation on N pairs out M and PP correlation on the remaining (M-N). The experimental curve[7] is included for comparison.

Figure 2.4 shows that the GVB-RCI active space is close to optimal for a broad region around the equilibrium geometry. Although CASSCF is preferable for the stretched bond (between 1.7 and 2.3 Å), it does not select the optimal active space at distances larger than 2.5 Å.

The computed bond energies are reported in Table 2.1.

2.3.2 Transition States

Radical Reaction: $H_2 + H$

The simplest reaction we studied is the linear $H_2 + H \longrightarrow H + H_2$. The results for several levels of computations are reported in Figure 2.5. In order to have an even number of electrons in the active space, the unpaired electron was formally paired with a fourth electron placed on a hydrogen atom at infinite distance.

In this case UHF, GVB-RCI and CASSCF all provide reasonable descriptions of the reaction. RHF and GVB-PP predict an unphysical edge at the transition state. The edge is due to the Restricted or the Perfect Pairing nature of the wavefunction: at the transition state the electrons

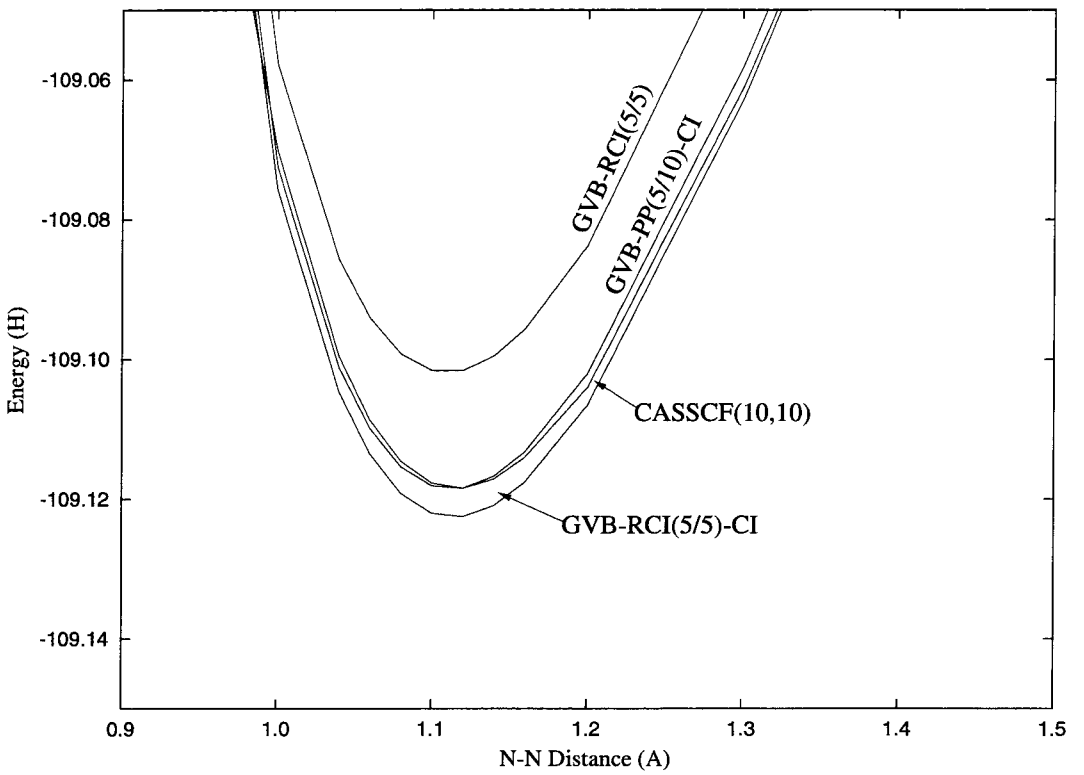

Figure 2.2: Equilibrium region of the N_2 potential at various levels of theory. (All using 6-31G* basis sets.) GVB-RCI and CASSCF are self-consistent. GVB-PP+CI and GVB-RCI+CI are active space CI based on GVB-PP and GVB-RCI wavefunctions, respectively. The fact that CASSCF gives higher energy than GVB-RCI+CI is due to the inability of the commercial implementation of CASSCF used to select the best active orbitals.

Bond	UHF	UHF+MP2	GVB-PP	GVB-RCI	CASSCF	Exper.
N_2	108.7	212.7	163.3^a	203.9^a	211.8^a	228.5
CO	171.7	255.2	207.8^b	244.2^b	253.0^b	257.3

Table 2.1: Computed bond energies of N_2 and CO in kcal/mol. ^{a} indicates 10 electrons, 10 orbitals active space, corresponding to 5 GVB pairs. ^{b} indicates 6 electrons, 6 orbitals active space, corresponding to 3 GVB pairs.

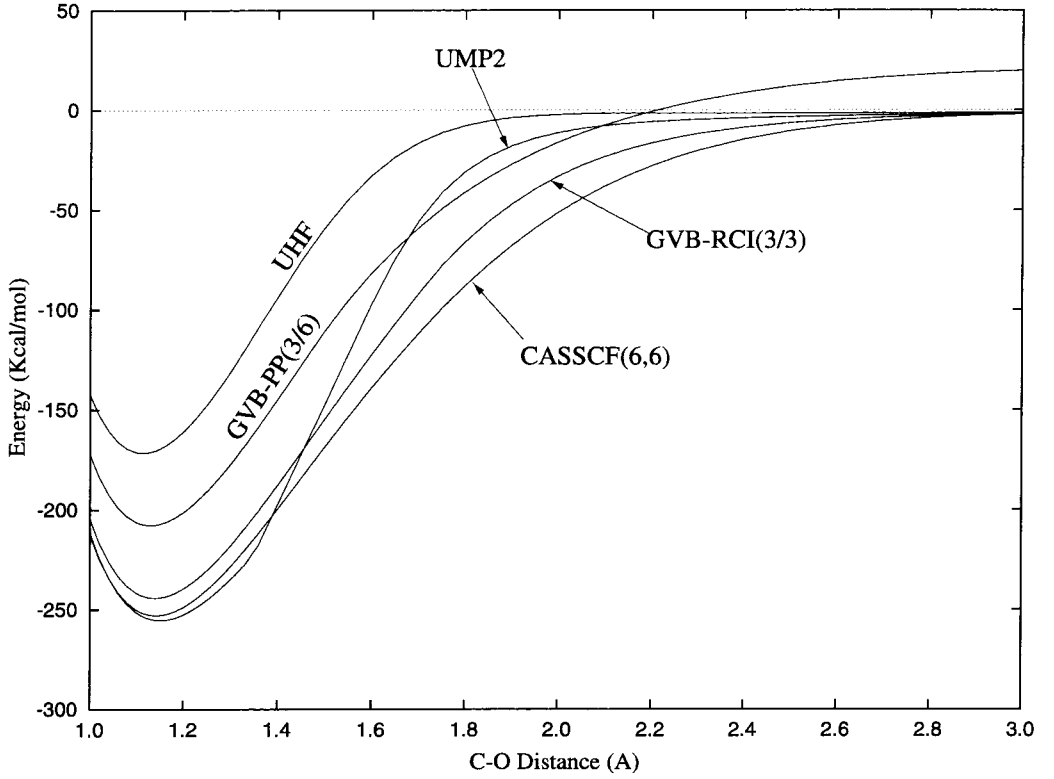

Figure 2.3: *CO* dissociation potential at various levels of theory. (All using the 6-31G* basis set.)

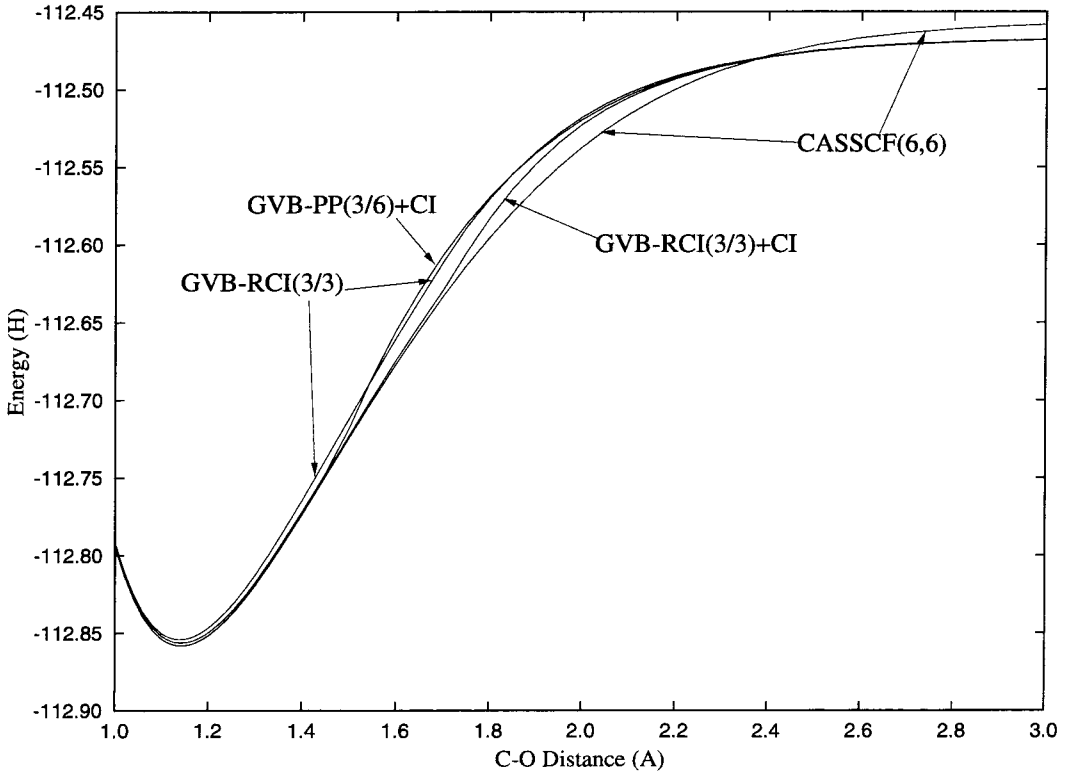

Figure 2.4: *CO* dissociation potential at various levels of theory. GVB-RCI+CI (GVB-RCI followed by active space CI) shows that GVB-RCI selects the optimal active space in a broader region than GVB-PP.

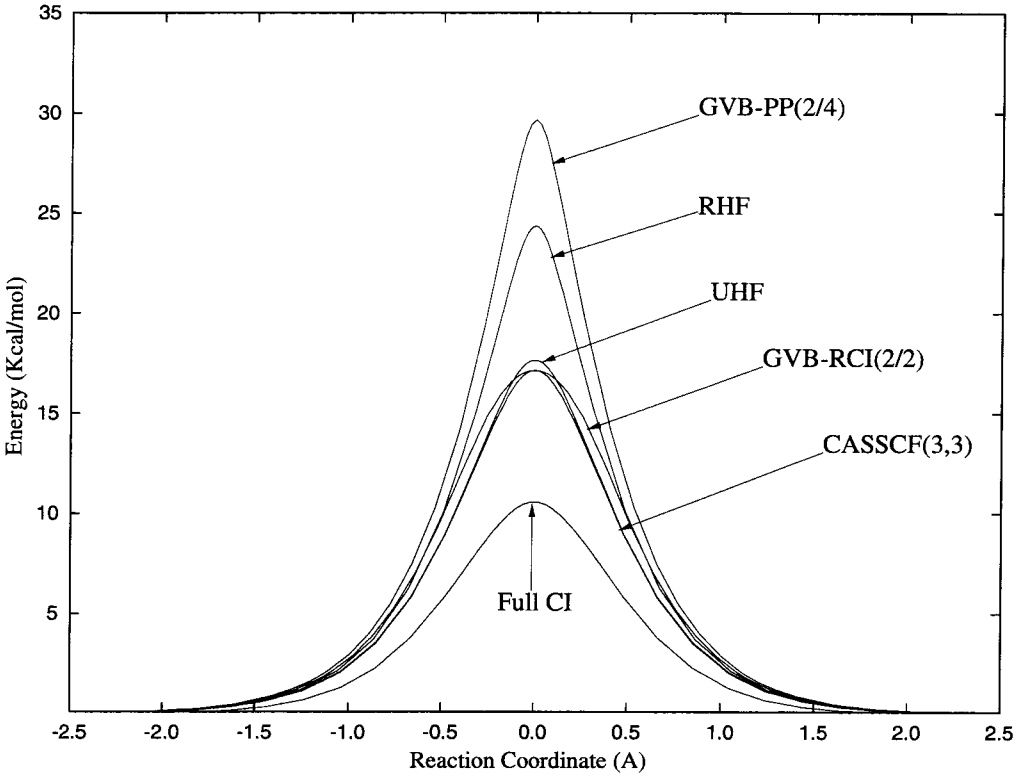

Figure 2.5: Reaction profile for $H_2 + H \longrightarrow H + H_2$ along the reaction path. (Using cc-pVTZ basis set.) The reaction coordinate was determined for each level of theory as reported in Figure 2.6, with the exception of Full CI, which is based on the CASSCF reaction coordinate.

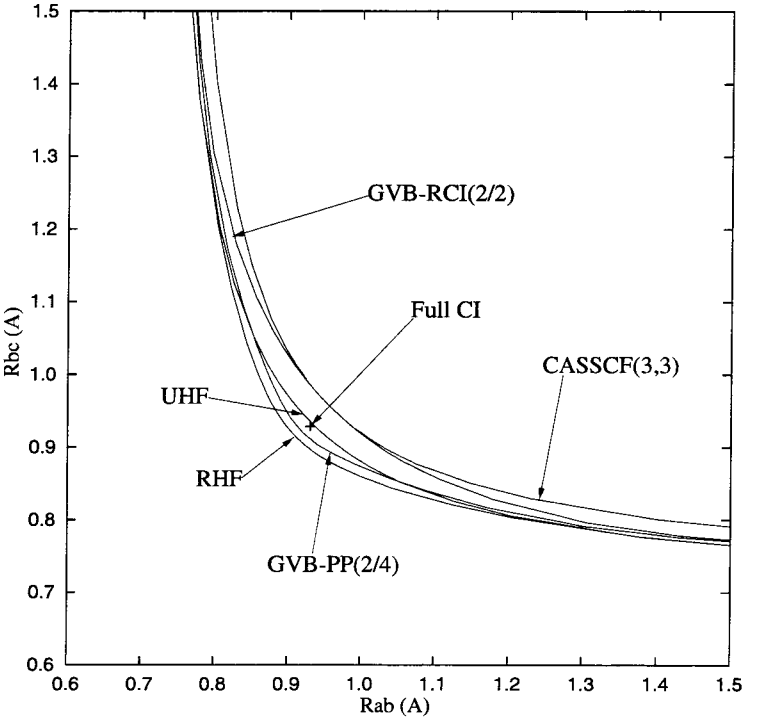

Figure 2.6: Reaction coordinate for $H_aH_b + H_c \longrightarrow H_a + H_bH_c$ for various levels of theory. (Using the cc-pVTZ basis set.) The Full CI transition state is included for comparison.

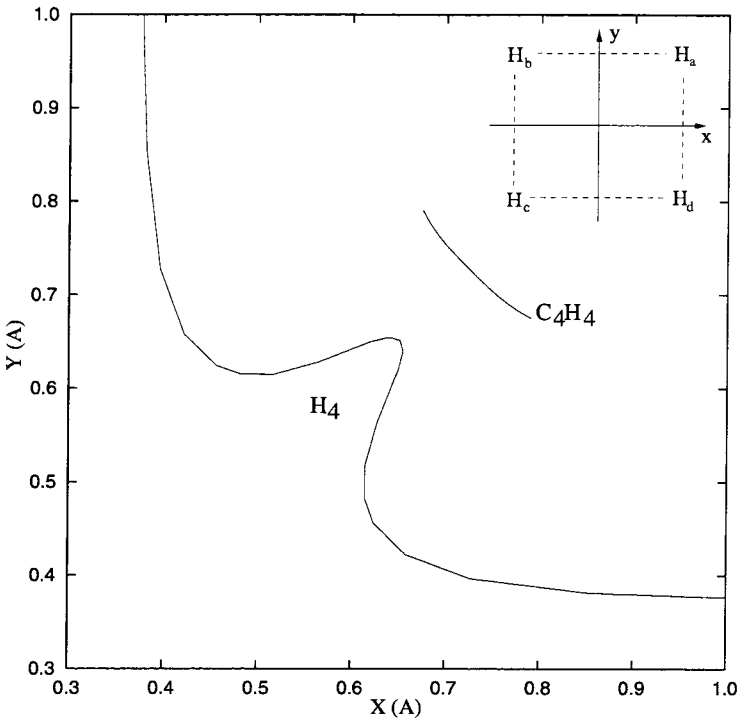

Figure 2.7: Reaction coordinates for pseudorotation of C_4H_4 and for the transition state of $H_aH_b + H_cH_d \longrightarrow H_aH_d + H_bH_c$. Both curves are computed at CASSCF(4,4) level and refer to D_{2h} systems. H_4 refers to the position of H_a in the plane of the molecule as depicted in the upper right corner. C_4H_4 refers to the position of one of the cyclobutadiene carbons. Notice that cyclobutadiene cannot stretch at the transition state due to the presence of the σ bonds.

cannot rearrange the pairing in a smooth way unless more than two natural orbitals per pair are allowed. The Full CI energy profile indicates that post-SCF treatment is required to account for a significant portion of the correlation energy.

The reaction coordinate was computed at various levels or theory and the results for the saddle point region are reported in Figure 2.6. The Full CI energy profile was computed at CASSCF geometries. Only the transition state geometry was optimized at the Full CI level and the result is included in Figure 2.6 for comparison. GVB-RCI provides essentially the same geometry as CASSCF for the maximum along the reaction coordinate while UHF and GVB-PP predict bond lengths shorter by 0.036 Å.

Forbidden Reaction: $H_2 + H_2$

The next reaction we studied is $H_2 + H_2$ with D_{2h} (rectangular planar) geometry. The reaction coordinate was determined at the CASSCF(4,4) level with cc-pVTZ basis set and it is reported in Figure 2.7. The same reaction coordinate was then used for all levels of theory. The reaction profiles are reported in Figure 2.8. In the UHF case, only the singlet spin state was considered.

As shown in Figure 2.8, UHF and GVB-PP fail to describe properly the transition state. The

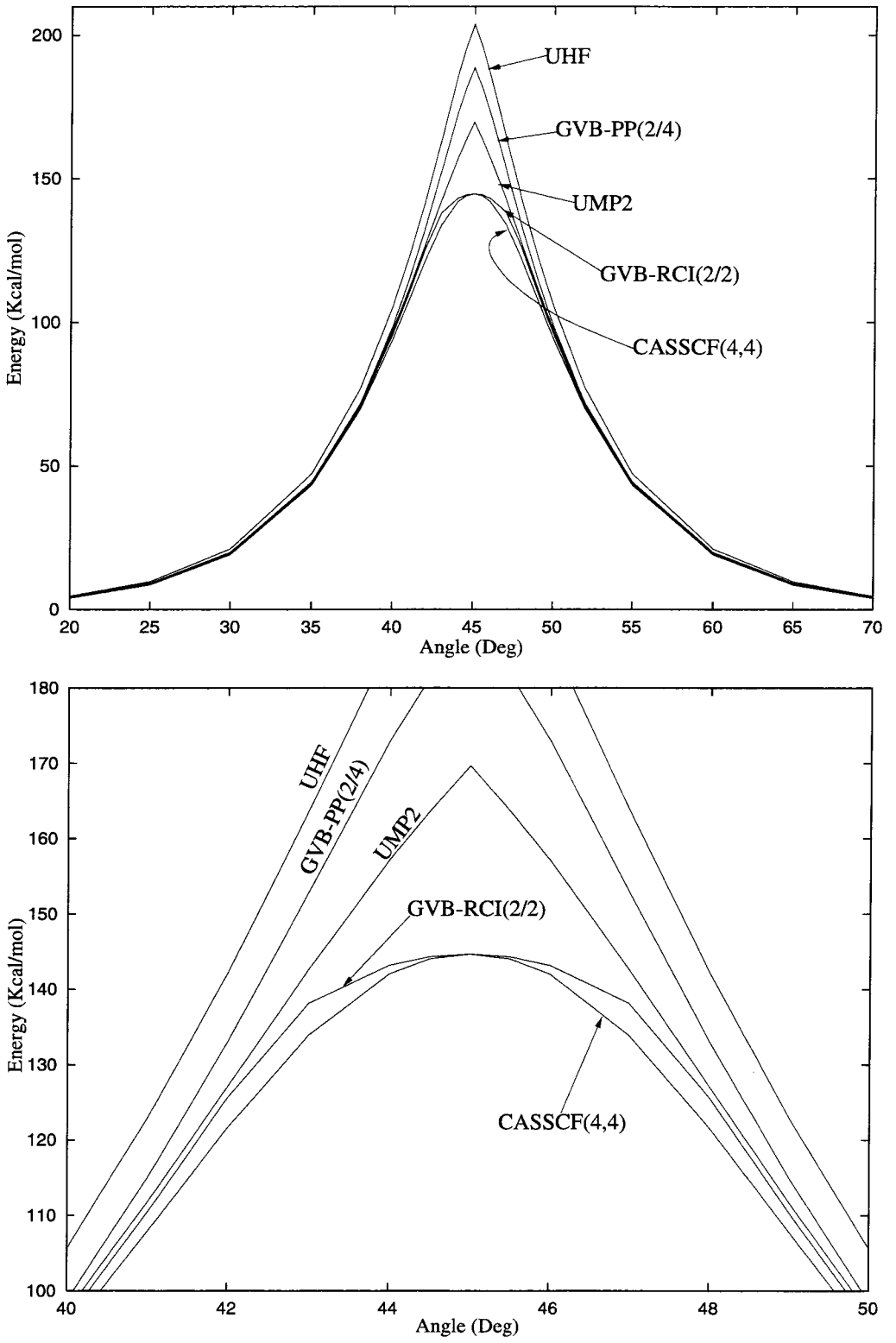

Figure 2.8: Energy profile for $H_2 + H_2$ (D_{2h} geometry) along the CASSCF(4,4) reaction coordinate reported in Figure 2.7(H_4). The abscissa is the angle $\arctan(Y/X)$, where X and Y are the cartesian coordinates of Figure 2.7. The bottom plot is a magnification of the transition state region reported on the top. The GVB-RCI potential has an edge at about 43° and 47°.

MP2 treatment of the UHF wavefunction does not correct the problem. The GVB-RCI potential energy profile is not smooth, that is, it is the superposition of two distinct electronic states with a discontinuity in the gradient; however, the discontinuity is not at the transition state and we expect the GVB-RCI description to provide good potential energy surfaces for most transition states. GVB-RCI fails to describe the transition state region when it is important to include configurations to describe charge transfer from one pair to another, as is the case for *tight* transition states, with all the active electrons confined in a restricted volume of space. In this case it is easy to include the missing configurations at the post-SCF level.

Forbidden Reaction: Cyclobutadiene

In order to understand the importance of this shortcoming, we studied the transition between the two forms of cyclobutadiene.

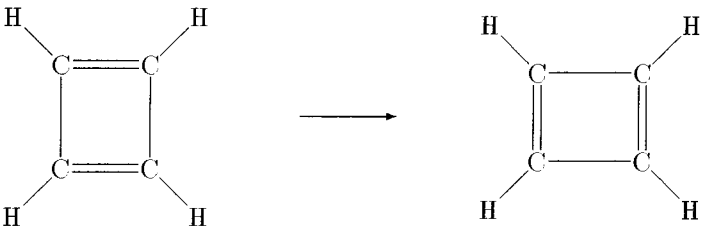

The reaction coordinate was determined at the CASSCF(4,4) level, with correlation on the four π electrons, using 6-31G* basis set and was used for all levels of theory. The reaction coordinate is reported in Figure 2.7 along with the reaction coordinate for $H_2 + H_2$ reaction. The main difference between the two paths is that in the case of cyclobutadiene the transition state cannot stretch outward due to the presence of the σ bonds.

As reported in Figure 2.9, UHF, UHF+MP2, GVB-PP, and GVB-RCI fail to describe the transition properly, while CASSCF provides a physically reasonable potential energy profile.

A detailed analysis of the wavefunction indicates that the difference between GVB-RCI and CASSCF wavefunctions is due to the two configurations shown schematically in Figure 2.10. Inclusion of the extra configurations at the post-SCF level lowers the GVB-RCI energy to within 0.4 kcal/mol of the CASSCF energy. This indicates that the active space selected by GVB-RCI is almost optimal.

This potential energy is compared with CASSCF in Figure 2.11.

2.3.3 Transition Metal Compounds

As an example of reaction at a transition metal center, we studied the H insertion into the $Ru = CH_2$ double bond in the complex $ClRuHCH_2$ —— $ClRuCH_3$.

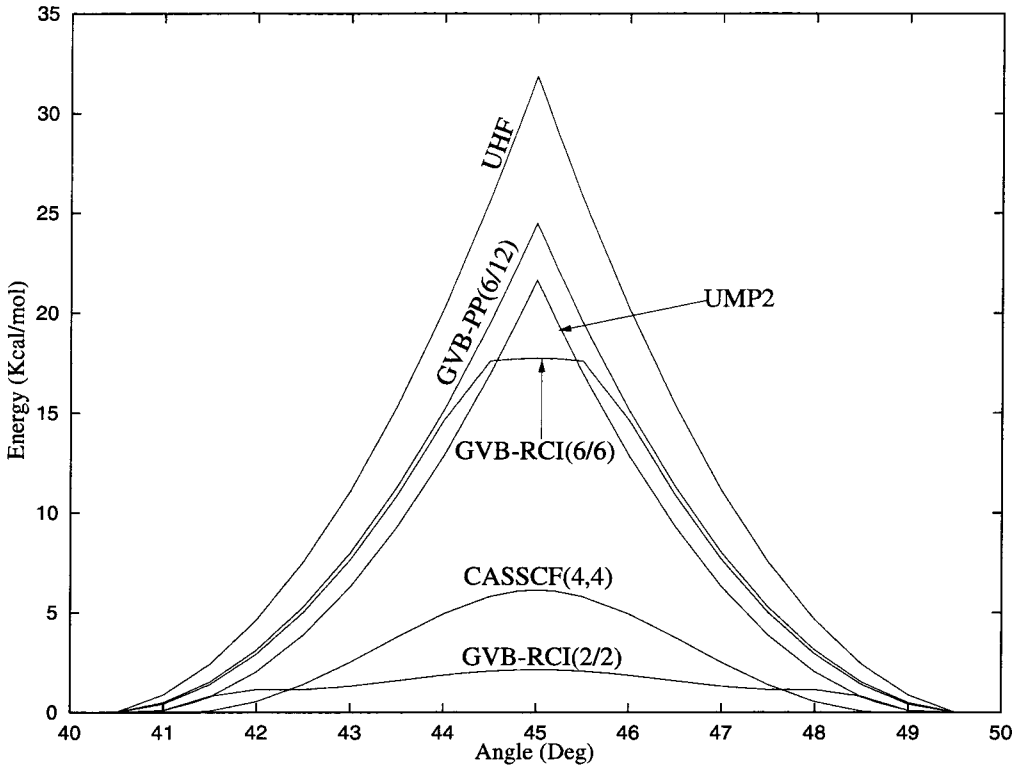

Figure 2.9: Energy profile along the CASSCF(4,4) reaction coordinate for pseudorotation of C_4H_4 reported in Figure 2.7(C_4H_4).

The reaction coordinate determined at the UHF+MP2 level was used also for the other levels of theory. (We used 6-31G** basis set on the carbon and hydrogens, LACV Effective Core Potential (ECP) and double-ζ basis set on Ru, and LAV ECP and double-ζ basis set on Cl.) Figure 2.12 summarizes the results obtained at various levels. The active space used to describe the reaction includes six electrons and six orbitals in the $H - Ru - C$ plane. These orbitals correspond to the σ_{RuH}, σ^*_{RuH}, σ_{RuC}, σ^*_{RuC}, π_{RuC}, and π^*_{RuC} in the reactant and to σ_{RuC}, σ^*_{RuC}, σ_{CH}, σ^*_{CH}, and two d orbitals on Ru in the product.

While UHF cannot describe properly the reactants and predicts essentially no barrier for the forward reaction, all other methods give a more reasonable description. Figure 2.12 shows clearly that although the GVB-PP description is qualitatively correct, this level of theory cannot be trusted in the quantitative estimate of reaction and activation enthalpies.

GVB-RCI provides a substantially better result, recovering a large portion of the active space correlation energy (95.7%, 89.7%, and 94.5% of the active space correlation energy is recovered at 25°, 53°, and 90°, respectively). CASSCF and UMP2 are provided for comparison.

Orbitals

B_{3u} B_{1g} B_{2g} A_u

Configurations

Config. N.	Occupancy			
	B_{3u}	B_{1g}	B_{2g}	A_u
1	2	2	0	0
2	2	0	2	0
3	0	2	0	2
4	0	0	2	2
5	1	1	1	1
6	0	2	2	0
7	2	0	0	2

Figure 2.10: Decomposition of the active space for C_4H_4. The four symmetry orbitals are represented on top; each circle represents the lobe of a p orbital coming out of the page and the sign represents its phase. The bottom reports the configurations important for the CASSCF wavefunction. Configurations $1-5$ form the GVB-RCI active space. When configurations 6 and 7 are added to GVB-RCI with a post-SCF CI, the resulting energies approach the CASSCF result as reported in Figure 2.11.

2.3.4 Computational Details

All RHF, GVB-PP, GVB-RCI, Full CI computations, as well as the CASSCF for the Ru system were performed with our code. All UHF, UMP2, and the remaining CASSCF computations were performed using GAUSSIAN92 and GAUSSIAN94[8].

2.4 Conclusions

We have developed a self-consistent computational method, called GVB-RCI, which is able to provide good potential energy surfaces for most reactions that are not properly described at the HF or GVB-PP levels. The method considers only a small number of selected configurations to describe the wavefunction and requires the transformation of a limited number of integrals at each self-consistent step.

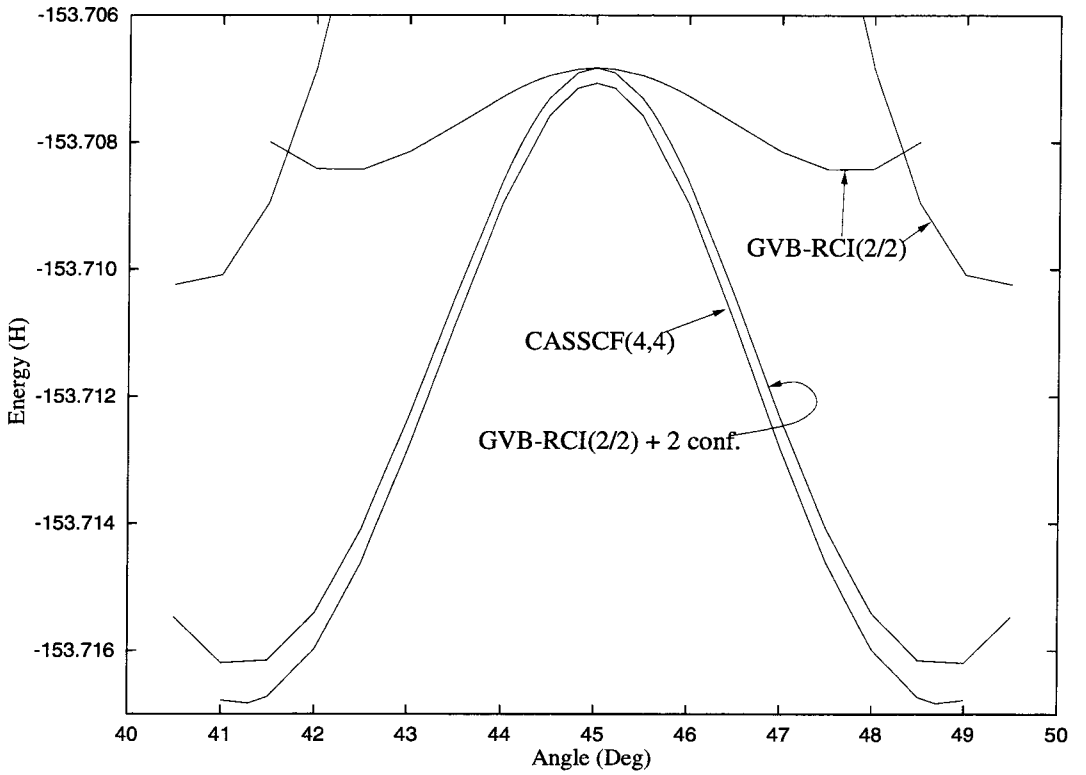

Figure 2.11: Energy profile obtained when two extra configurations are added at the post SCF stage to the GVB-RCI wavefunction is reported as GVB-RCI(2/2)+2 conf. Notice that the GVB-RCI(2/2) leads to two energy surfaces depending on spin coupling.

We tested GVB-RCI on a few simple systems, to verify the limits to its applicability and to suggest possible improvements at the post SCF level.

The potential energies obtained are consistently better than UHF and GVB-PP, often approaching the CASSCF quality. It must however be pointed out that in transition metal systems, dynamic correlation involving excitations outside the active space may play a significant role. The self-consistent wavefunctions considered in this chapter must hence be regarded as starting points for further procedures to include correlation energy, such as CI or perturbative expansions.

Appendix

It is necessary to optimize three kinds of coefficients:

- Pair coefficients C_I^g, C_I^u, defined in Eq. 2.2. for all GVB pairs I.
- Spin coefficients C_{IJ}^s, C_{IJ}^t, defined in Eq. 2.3, for all combinations IJ.
- CI coefficients C_0, C_{IJ}, defined in Eq. 2.5.

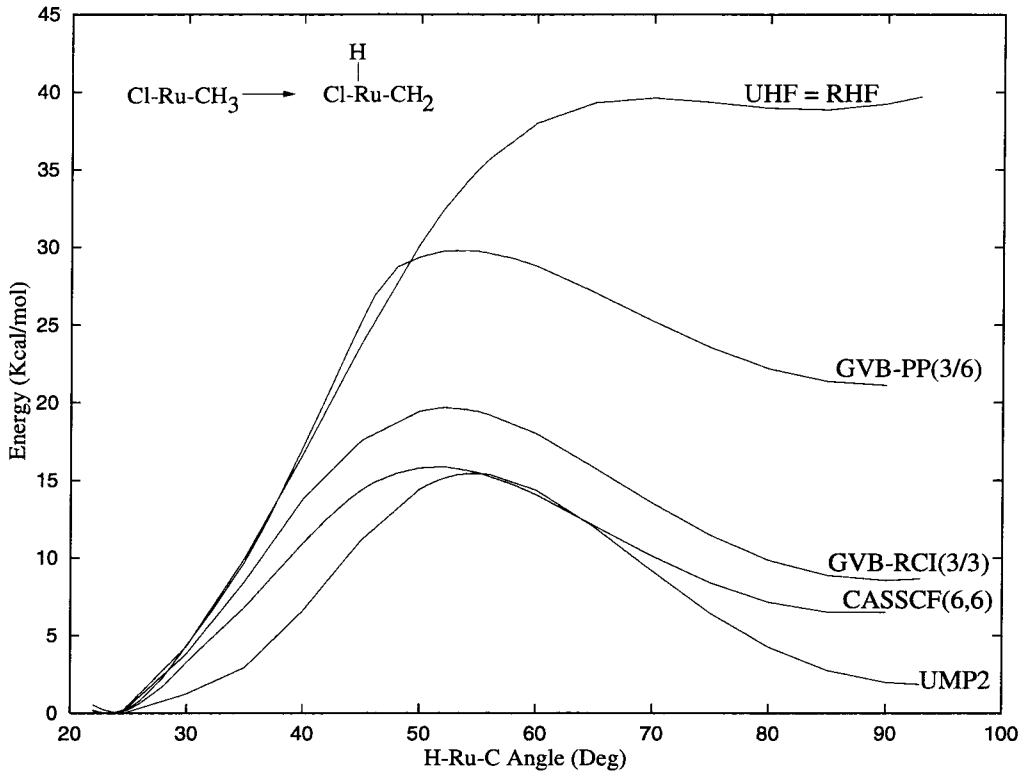

Figure 2.12: Energy profile for $ClHRuCH_2 \longrightarrow ClRuCH_3$ at various levels of theory.

We optimize each kind of coefficient assuming the other kinds to be fixed and iterate to a self consistent convergence.

Pair Coefficients

Consider the GVB coefficients for a pair $P \in RCI$, namely $C_p = C_P^g$ and $C_{p'} = C_P^u$. Assuming that all other parameters are fixed, the total energy can be expressed as

$$\begin{aligned} E &= \text{Constant} + 2f_p h_p + 2f_{p'} h_{p'} + a_{pp} J_{pp} + b_{pp} K_{pp} + a_{p'p'} J_{p'p'} + b_{p'p'} K_{p'p'} + \\ &\quad + 2\sum_{i \notin P} (a_{ip} J_{ip} + b_{ip} K_{ip} + a_{ip'} J_{ip'} + b_{ip'} K_{ip'}) + 2(a_{pp'} J_{pp'} + b_{pp'} K_{pp'}) + \\ &\quad + \sum_{I \neq P} [r_{IP}(ip|i'p') + s_{IP}(ip'|i'p) + t_{IP}(ii'|pp')] \end{aligned}$$

Substituting the values of the parameters f, a, b, r, s, and t and collecting the pair coefficients, this becomes

$$\frac{1}{2}E = \tilde{\mathbf{C}}\mathbf{Y}\mathbf{C} - 2\tilde{\mathbf{C}}\mathbf{X} + \text{Constant}$$

where

$$\mathbf{C} = \begin{vmatrix} C_p \\ C_{p'} \end{vmatrix} \qquad \mathbf{Y} = \begin{vmatrix} Y_{pp} & Y_{pp'} \\ Y_{p'p} & Y_{p'p'} \end{vmatrix} \qquad \mathbf{X} = \begin{vmatrix} X_p \\ X_{p'} \end{vmatrix}$$

The explicit values of each element are

$$\begin{aligned} Y_{pp} &= \Gamma_P h_p + \frac{1}{2}\Gamma_P J_{pp} + \Gamma_P \sum_{i \notin RCI} (2f_i J_{ip} - f_i K_{ip}) + \\ &+ \sum_{i \in RCI, i \notin P} \left\{ \left[(\Gamma_I + \Gamma_P + C_{IP}^2 - 1)C_i^2 + \frac{1}{2}(1 - \Gamma_I - C_{IP}^2) \right] (2J_{ip} - K_{ip}) \right\} \end{aligned}$$

$$\begin{aligned} Y_{p'p'} &= \Gamma_P h_{p'} + \frac{1}{2}\Gamma_P J_{p'p'} + \Gamma_P \sum_{i \notin RCI} (2f_i J_{ip'} - f_i K_{ip'}) + \\ &+ \sum_{i \in RCI, i \notin P} \left\{ \left[(\Gamma_I + \Gamma_P + C_{IP}^2 - 1)C_i^2 + \frac{1}{2}(1 - \Gamma_I - C_{IP}^2) \right] (2J_{ip'} - K_{ip'}) \right\} \end{aligned}$$

$$Y_{p'p} = Y_{pp'} = -\frac{1}{2}\Gamma_P K_{pp'}$$

$$\begin{aligned} X_p &= -\frac{1}{4} \sum_{I \neq P} \left\{ \left[C_0 C_{IP} C_{i'} (\sqrt{3} C_{IP}^t + C_{IP}^s) - C_i \sum_K C_{IK} C_{KP} (C_{IK}^s C_{KP}^s + C_{IK}^t C_{KP}^t) \right] (ip|i'p') + \right. \\ &+ \left[C_0 C_{IP} C_i (\sqrt{3} C_{IP}^t - C_{IP}^s) + C_{i'} \sum_K C_{IK} C_{KP} (C_{IK}^s C_{KP}^s - C_{IK}^t C_{KP}^t) \right] (ip'|i'p) + \\ &+ \left. \left[2C_0 C_{IP} (C_i - C_{i'}) C_{IP}^s + 2(C_i - C_{i'}) \sum_K C_{IK} C_{KP} (C_{IK}^s C_{KP}^s) \right] (ii'|pp') \right\} \end{aligned}$$

$$\begin{aligned} X_{p'} &= -\frac{1}{4} \sum_{I \neq P} \left\{ \left[C_0 C_{IP} C_i (\sqrt{3} C_{IP}^t + C_{IP}^s) - C_{i'} \sum_K C_{IK} C_{KP} (C_{IK}^s C_{KP}^s + C_{IK}^t C_{KP}^t) \right] (ip|i'p') + \right. \\ &+ \left[C_0 C_{IP} C_{i'} (\sqrt{3} C_{IP}^t - C_{IP}^s) + C_i \sum_K C_{IK} C_{KP} (C_{IK}^s C_{KP}^s - C_{IK}^t C_{KP}^t) \right] (ip'|i'p) + \\ &- \left. \left[2C_0 C_{IP} (C_i - C_{i'}) C_{IP}^s + 2(C_i - C_{i'}) \sum_K C_{IK} C_{KP} (C_{IK}^s C_{KP}^s) \right] (ii'|pp') \right\} \end{aligned}$$

We minimize the energy subject to the constraint $\tilde{\mathbf{C}}\mathbf{C} = 1$

$$\frac{\partial \left[\tilde{\mathbf{C}}\mathbf{Y}\mathbf{C} - 2\tilde{\mathbf{C}}\mathbf{X} + \text{Constant} - \lambda(\tilde{\mathbf{C}}\mathbf{C} - 1) \right]}{\partial \mathbf{C}} \propto (\mathbf{Y} - \lambda \mathbf{I})\mathbf{C} - \mathbf{X} = 0$$

where λ is the Lagrange multiplier.

The system has solution

$$\begin{aligned}
\mathbf{C} &= \begin{vmatrix} C_p \\ C_{p'} \end{vmatrix} = \begin{vmatrix} Y_{pp} - \lambda & Y_{pp'} \\ Y_{p'p} & Y_{p'p'} - \lambda \end{vmatrix}^{-1} \begin{vmatrix} X_p \\ X_{p'} \end{vmatrix} = \\
&= \frac{1}{(Y_{pp} - \lambda)(Y_{p'p'} - \lambda) - Y_{p'p}^2} \begin{vmatrix} Y_{p'p'} - \lambda & -Y_{pp'} \\ -Y_{p'p} & Y_{pp} - \lambda \end{vmatrix} \begin{vmatrix} X_p \\ X_{p'} \end{vmatrix} = \\
&= \frac{1}{(Y_{pp} - \lambda)(Y_{p'p'} - \lambda) - Y_{p'p}^2} \begin{vmatrix} (Y_{p'p'} - \lambda)X_p - Y_{pp'}X_{p'} \\ (Y_{pp} - \lambda)X_{p'} - Y_{p'p}X_p \end{vmatrix}
\end{aligned}$$

which leads to the normalization condition

$$1 = C_p^2 + C_{p'}^2 = \frac{\left[(Y_{p'p'} - \lambda)X_p - Y_{pp'}X_{p'}\right]^2 + \left[(Y_{pp} - \lambda)X_{p'} - Y_{p'p}X_p\right]^2}{\left[(Y_{pp} - \lambda)(Y_{p'p'} - \lambda) - Y_{p'p}^2\right]^2}$$

which in turn leads to the equation in λ

$$\begin{aligned}
0 = {} & \lambda^4 - 2Tr\lambda^3 + \left[2\,\Delta + Tr^2 - X_{p'}^2 - X_p^2\right]\lambda^2 + \\
& + \left[2\,(X_p\,Y_{p'p'} - Y_{pp'}\,X_{p'})\,X_p + 2\,(X_{p'}\,Y_{pp} - Y_{pp'}\,X_p)\,X_{p'} - 2\,\Delta Tr\right]\lambda + \\
& - (X_p\,Y_{p'p'} - Y_{pp'}\,X_{p'})^2 + \Delta^2 - (X_{p'}\,Y_{pp} - Y_{pp'}\,X_p)^2
\end{aligned}$$

where

$$\Delta = Y_{pp}\,Y_{p'p'} - Y_{pp'}^2 \qquad\qquad Tr = Y_{pp} + Y_{p'p'}$$

which has four real solutions since the the hamiltonian is hermitian.

λ is related to the energy by $E \propto \lambda - \widetilde{\mathbf{C}}\mathbf{X}$ which enables us to select the solution that minimizes the energy. Notice that the normalization condition can be satisfied in all cases except when λ is an eigenvalue of the matrix $\mathbf{Y}$, in which case it must be $\mathbf{X} = \mathbf{0}$ and we can solve the homogeneous equation.

The optimal coefficients for each pair depend from the coefficients of the other pairs and from the other CI coefficients; therefore, the solution must be determined iteratively until self-consistency.

In the special case that pair P is treated at the perfect pairing level, the above expressions simplify as follows.

The total energy can be expressed as

$$\begin{aligned}
E = {} & \text{Constant} + 2f_p h_p + 2f_{p'} h_{p'} + a_{pp} J_{pp} + b_{pp} K_{pp} + a_{p'p'} J_{p'p'} + b_{p'p'} K_{p'p'} + \\
& + 2\sum_{i \notin P} (a_{ip} J_{ip} + b_{ip} K_{ip} + a_{ip'} J_{ip'} + b_{ip'} K_{ip'}) + 2\,(a_{pp'} J_{pp'} + b_{pp'} K_{pp'})
\end{aligned}$$

which takes the form

$$\frac{1}{2}E = \text{Constant} + \widetilde{\mathbf{C}}\mathbf{Y}\mathbf{C}$$

where

$$\mathbf{C} = \begin{vmatrix} C_p \\ C_{p'} \end{vmatrix} \qquad \text{and} \qquad \mathbf{Y} = \begin{vmatrix} Y_{pp} & Y_{pp'} \\ Y_{p'p} & Y_{p'p'} \end{vmatrix}$$

and

$$\begin{aligned} Y_{ii} &= h_i + \frac{1}{2}J_{ii} + \sum_{j \notin P} f_j(2J_{ji} - K_{ji}) \\ Y_{ij} &= -\frac{1}{2}K_{ij} \qquad\qquad \text{for } i \neq j \end{aligned}$$

We minimize the energy with the constraint $\widetilde{\mathbf{C}}\mathbf{C} = 1$:

$$\frac{\partial\left[\widetilde{\mathbf{C}}\mathbf{Y}\mathbf{C} - \lambda(\widetilde{\mathbf{C}}\mathbf{C} - 1)\right]}{\partial \mathbf{C}} \propto \mathbf{Y}\mathbf{C} - \lambda\mathbf{C} = 0$$

In this case λ is directly proportional to the energy.

Spin Coefficients

We optimize the coefficients C^t_{PQ} and C^s_{PQ} assuming all other coefficients are frozen.

All terms in the energy expression that do not depend on C^t_{PQ} or C^s_{PQ} are constant, so we can write:

$$\begin{aligned} E \;=\; & \text{Constant} + 2b_{pp'}K_{pp'} + 2b_{pq}K_{pq} + 2b_{pq'}K_{pq'} + 2b_{p'q}K_{p'q} + 2b_{p'q'}K_{p'q'} + 2b_{qq'}K_{qq'} + \\ & + 2r_{PQ}(pq|p'q') + 2s_{PQ}(pq'|p'q) + 2t_{PQ}(pp'|qq') + \\ & + 2\sum_{I \neq P,Q}\left[r_{IP}(ip|i'p') + s_{IP}(ip'|i'p) + t_{IP}(ii'|pp') + r_{IQ}(iq|i'q') + s_{IQ}(iq'|i'q) + t_{IQ}(ii'|qq')\right] \end{aligned}$$

Which is put in the form

$$E = \text{Constant} + \widetilde{\mathbf{C}}\mathbf{Y}\mathbf{C} - 2\widetilde{\mathbf{C}}\mathbf{X}$$

where

$$\begin{aligned} Y_{tt} &= C^2_{PQ}\left[\frac{1}{2}(K_{pq} + K_{pq'} + K_{p'q} + K_{p'q'}) - (K_{pp'} + K_{qq'})\right] \\ Y_{ss} &= C^2_{PQ}\left[(K_{pp'} + K_{qq'}) - \frac{1}{2}(K_{pq} + K_{pq'} + K_{p'q} + K_{p'q'})\right] \\ Y_{st} &= Y_{ts} = C^2_{PQ}\frac{\sqrt{3}}{2}(K_{pq} + K_{p'q'} - K_{pq'} - K_{p'q}) \end{aligned}$$

$$
\begin{aligned}
X_t &= -\sqrt{3}C_0C_{PQ}\left(C_pC_{q'}+C_{p'}C_q\right)(pq|p'q') - \sqrt{3}C_0C_{PQ}\left(C_pC_q+C_{p'}C_{q'}\right)(pq'|p'q) + \\
&+C_{PQ}\sum_{I\neq P,Q}\left[C_{IQ}C^t_{IQ}\left(C_iC_p+C_{i'}C_{p'}\right)(ip|i'p') + C_{IQ}C^t_{IQ}\left(C_iC_{p'}+C_{i'}C_p\right)(ip'|i'p) + \right. \\
&\left. + C_{IP}C^t_{IP}\left(C_iC_q+C_{i'}C_{q'}\right)(iq|i'q') + C_{IP}C^t_{IP}\left(C_iC_{q'}+C_{i'}C_q\right)(iq'|i'q)\right]
\end{aligned}
$$

$$
\begin{aligned}
X_s &= -C_0C_{PQ}\left(C_pC_{q'}+C_{p'}C_q\right)(pq|p'q') + C_0C_{PQ}\left(C_pC_q+C_{p'}C_{q'}\right)(pq'|p'q) + \\
&-2C_0C_{PQ}\left(C_p-C_{p'}\right)\left(C_q-C_{q'}\right)(pp'qq') + \\
&+C_{PQ}\sum_{I\neq P,Q}\left[C_{IQ}C^s_{IQ}\left(C_iC_p+C_{i'}C_{p'}\right)(ip|i'p') - C_{IQ}C^s_{IQ}\left(C_iC_{p'}+C_{i'}C_p\right)(ip'|i'p) + \right. \\
&-2C_{IQ}C^s_{IQ}\left(C_i-C_{i'}\right)\left(C_p-C_{p'}\right)(ii'|pp') + C_{IP}C^s_{IP}\left(C_iC_q+C_{i'}C_{q'}\right)(iq|i'q') + \\
&\left. -C_{IP}C^s_{IP}\left(C_iC_{q'}+C_{i'}C_q\right)(iq'|i'q) - 2C_{IP}C^s_{IP}\left(C_i-C_{i'}\right)\left(C_q-C_{q'}\right)(ii'|qq')\right]
\end{aligned}
$$

and the optimal coefficients can be found using the same algorithm described in the pair coefficients optimization (this time the $\mathbf{Y}$ matrix is traceless; therefore, the equation in λ is simpler).

CI Coefficients

Let $\mathbf{H}$ denote the CI matrix:

$$
\mathbf{H} = \begin{vmatrix}
<\Psi^{GVB}|H|\Psi^{GVB}> & <\Psi^{GVB}|H|\Psi^{RCI}_{12}> & <\Psi^{GVB}|H|\Psi^{RCI}_{13}> & \cdots & <\Psi^{GVB}|H|\Psi^{RCI}_{R-1,R}> \\
<\Psi^{RCI}_{12}|H|\Psi^{GVB}> & <\Psi^{RCI}_{12}|H|\Psi^{RCI}_{12}> & <\Psi^{RCI}_{12}|H|\Psi^{RCI}_{13}> & \cdots & <\Psi^{RCI}_{12}|H|\Psi^{RCI}_{R-1,R}> \\
<\Psi^{RCI}_{13}|H|\Psi^{GVB}> & <\Psi^{RCI}_{13}|H|\Psi^{RCI}_{12}> & <\Psi^{RCI}_{13}|H|\Psi^{RCI}_{13}> & \cdots & <\Psi^{RCI}_{13}|H|\Psi^{RCI}_{R-1,R}> \\
\vdots & \vdots & \vdots & \ddots & \vdots \\
<\Psi^{RCI}_{R-1,R}|H|\Psi^{GVB}> & <\Psi^{RCI}_{R-1,R}|H|\Psi^{RCI}_{12}> & <\Psi^{RCI}_{R-1,R}|H|\Psi^{RCI}_{13}> & \cdots & <\Psi^{RCI}_{R-1,R}|H|\Psi^{RCI}_{R-1,R}>
\end{vmatrix}
$$

Each element of $\mathbf{H}$ can be expressed as function of the pair and spin coefficients by expanding each bra and ket and collecting equal integrals over the orbitals.

The ground state CI coefficients are given by the eigenvector with lowest eigenvalue, i.e., lowest energy, of the above matrix.

Again, the matrix elements depend on the pair and spin coefficients, which in turn depend on the CI coefficients, so a self-consistent approach is required.

Acknowledgements

We thank Richard P. Muller for working out the detailed formulas for a special case. This research was supported by NSF (ASC 92-17368 and CHE 95-22179). In addition, the facilities of the MSC

are also supported by grants from ARO/DURIP, BP Chemical, ARO, Exxon, Seiko-Epson, Owens Corning, Asahi Chemical, Saudi Aramco, Beckman Institute, Chevron Petroleum Technology Co., Chevron Chemical Co., NASA/Ames, NASA/JPL, ONR, Avery Dennison, and Chevron Research Technology Co.

Bibliography

[1] Hinze, J.; *J. Chem. Phys.* **1973**, *59*, 6424. Shepard, R.; *Adv. Chem. Phys.* **1987**, *69*, 63.

[2] McWeeny, R.; *Methods of Molecular Quantum Mechanics*, 2^{nd} Edition. (Academic Press, 1992).

[3] Roos, B.O.; Taylor, P.R.; Siegbahn, P.E.M.; *Chem. Physics* **1980**, *48*, 157. Roos, B.O.; *Adv. Chem. Phys.* **1987**, *69*, 399.

[4] Szabo, A.; Ostlund, N.S.; *Modern Quantum Chemistry* (McGraw-Hill, 1989).

[5] Bobrowicz, F.W.; Goddard III, W.A.; *Modern Theoretical Chemistry*, Vol. 3, *Methods of Electronic Structure Theory*, Shaefer, H.F.III. (Plenum Press, 1977).

[6] Another form of post SCF GVB-RCI was previously used. See, for instance, Carter, E.A.; Goddard III, W.A.; *J. Chem. Phys.* **1988**, *88*, 3132.

[7] Lofthus, A.; Krupenie, P.H.; *J. Phys. Chem. Ref. Data* **1977**, *6*, 113.

[8] *Gaussian 92/DFT*, Revision F.4, Frisch, M.J.; Trucks, G.W.; Schlegel, H.B.; Gill, P.M.W.; Johnson, B.G.; Wong, M.W.; Foresman, J.B.; Robb, M.A.; Head-Gordon, M.; Replogle, E.S.; Gomperts, R.; Andres, J.L.; Raghavachari, K.; Binkley, J.S.; Gonzalez, C.; Martin, R.L.; Fox, D.J.; Defrees, D.J.; Baker, J.; Stewart, J.P.P; Pople, J.A.; Gaussian, Inc., Pittsburgh, PA, 1993. *Gaussian 94*, Revision B.3, Frisch, M.J.; Trucks, G.W.; Schlegel, H.B.; Gill, P.M.W.; Johnson, B.G.; Robb, M.A.; Cheeseman, J.R.; Keith, T.; Petersson, G.A.; Montgomery, J.A.; Raghavachari, K.; Al-Laham, M.A.; Zakrzewski, V.G; Ortiz, J.V.; Foresman, J.B.; Peng, C.Y.; Ayala, P.Y.; Chen, W.; Wong, M.W.; Andres, J.L.; Replogle, E.S.; Gomperts, R.; Martin, R.L.; Fox, D.J.; Binkley, J.S.; Defrees, D.J.; Baker, J.; Stewart, J.P.P; Head-Gordon, M.; Gonzalez, C.; Pople, J.A.; Gaussian, Inc., Pittsburgh, PA, 1995.

Chapter 3 Theoretical Description of the STM Images of Alkanes and Substituted Alkanes Adsorbed on Graphite

Abstract

A theoretical model based on perturbation theory has been developed to predict the Scanning Tunneling Microscopy (STM) images of molecules adsorbed on graphite. The model is applicable to a variety of different molecules with reasonable computational effort, and provides images that are in qualitative agreement with experimental results. The model predicts that topographic effects will dominate the STM images of alkanes on graphite surfaces. The computations correlate well with the STM data of functionalized alkanes, and allow assessment of the structure and orientation of most of the functionalized alkanes that have been studied experimentally. In addition, the computations suggest that the highly diffuse virtual orbitals, despite being much farther in energy from the Fermi level of the graphite than the occupied orbitals of the adsorbed molecules, may play an important role in determining the STM image contrast of such systems.

3.1 Introduction

This chapter contains the description of a theoretical model to interpret Scanning Tunneling Microscopy (STM) images of organic molecules adsorbed in ordered monolayers onto highly ordered pyrolytic graphite (HOPG) surfaces.[1] The project is the theoretical part of a more complete study of STM imaging of adsorbed monolayers carried out in collaboration with C. L. Claypool and N. S. Lewis.[1, 2]

The experimental images obtained by Claypool et al. are reported in reference [2]. The images reported therein reveal features as small as single atoms and/or functional groups in the adsorbed molecules and provide atomic level information on the electronic coupling profiles of such overlayers. The STM images observed in this work and in studies of related systems[3, 4, 5, 6] are, however, dependent on subtle structural changes in the adsorbed molecules, and appear to be the result of both electronic and geometric effects. Thus, to fully exploit this imaging technique, it is important to understand how different aspects of the adsorbate and the experimental conditions blend together to create the observed images.

The theoretical model described in this chapter has been developed to simulate the STM process in order to study and explain such phenomena for a large number of molecules. The method

is accurate enough to be useful and reliable, it is simple enough to provide a facile method for interpretation of the available STM results, and it is cheap enough to be applicable to the systems of interest – small functionalized alkanes on HOPG – with affordable computational effort, e.g., a few hours on an HP9000 workstation.

In order to attain this goal, we have developed an alternative to expensive quantum mechanics computations that include explicitly the wavefunctions of the tip and/or the graphite. Our approach is to (1) use a force field (FF) to optimize the geometry of the adsorbed molecules on graphite, (2) determine the shapes and the energies of the molecular orbitals (MO) using Hartree-Fock (HF) computations for the isolated molecule, and (3) then simulate the STM image using a simple perturbative approach which adds negligible cost with respect to steps 1 and 2.

Several theories have already been developed to predict and explain STM images of both surfaces and adsorbates. Tersoff and Hamman[7] used the transfer hamiltonian approach first introduced by Bardeen.[8] Their conclusion is that the observed current is proportional to the local density of states (LDOS) at the Fermi energy of the sample, at the position of the tip. Adsorbates are observed through the change they induce in the LDOS of the support. Lang[9] replaced the support and the tip with the jellium model and used a metal atom to mimic the tip. This procedure was used to predict the images of adsorbed atoms using the transfer hamiltonian approach in the low bias limit. Doyen and coworkers[10] have used semi-empirical techniques to study the exact tunneling current, evaluating the interactions between the tip and the support explicitly and without the assumptions of the transfer hamiltonian. More recently Hallmark, Chiang, and coworkers[11] have used extended Hückel calculations to predict images of aromatic molecules adsorbed on a metal substrate, and Sautet[12] used electron scattering techniques for the same purpose. Liang et al.[3] have also used the extended Hückel method to investigate the STM images of alkanes on graphite. Fisher and Blöchl[13] instead have performed *ab initio* density functional theory studies to simulate the STM imaging of adsorbed benzene molecules on graphite and MoS_2. Hui, Marcus, and Källebring[14] have developed a model for STM imaging of adsorbed molecules that includes the effect of d orbitals on the tip.

The models based on the transfer hamiltonian have proven effective in predicting images of conducting surfaces in the low bias limit. Tersoff-Hamman theory has been used to interpret atomic resolution STM images of insulating molecules on a metallic substrate, and these studies have indicated that the molecular features of the images are determined by the most protruded atoms of the adsorbed molecules.[3, 6] In addition, this work indicated that the insulating molecules were detected because their orbitals mix slightly into the Fermi level of the metallic substrate and because they are close to the tip.[3, 6] When adsorbed insulating molecules are sampled with higher biases, this approach requires that the periodic molecular structure, as well as the supporting graphite, be included in the simulation.[3, 13] As a result, significant effort is spent computing the band structure of the graphite every time a new molecule is studied. The method then becomes as complex

as other approaches that can lead, in principle, to an exact prediction but are not based on the transfer hamiltonian approximation. The result is that most methods which include the detailed wavefunctions of the graphite and the tip give excellent results but require extensive computations.

The goal of our work was to develop a theoretical approach that could aid in the interpretation of the experimental images obtained for alkanes and alkanols on graphite, in which the overlayer only is observed at high tip/sample biases.[2, 3, 4] Of course, the states of the graphite and of the tip are the initial and final states for tunneling processes for all of these molecular overlayers on a graphite surface. However, the primary goal of this theoretical study was to gain insight into the relative contributions of topographic and electronic factors in determining the STM contrast of different functional groups in the molecular overlayer. Since the experimental images for the different overlayers were obtained at a relatively constant tip/sample bias, the theoretical treatment focused on describing the changes in STM contrast for the various different molecules. To achieve this goal, a simple model was built that ignores the shape of the graphite states and that considers the coupling, or perturbation, between molecular states and a simplified version of graphitic states. In the high bias limit, such a model is expected to produce, at a fraction of the cost, the same results as a more complete treatment that explicitly includes the graphite orbitals. Of course, in the low bias limit, and for intermediate bias situations, this model will not be computationally useful nor physically appropriate. Our approach does, however, allow simulations of STM images on reasonably big systems with a good description of the molecular states involved mediating the tunneling process.

In Section 2 we present the theoretical model and the approximations used to implement it. Section 3 then describes the predictions of the model and compares model and experiment for a number of molecules for which the experimental images have been obtained.

3.2 Theoretical Model

We are interested in determining how the electric current between a tip and a graphite support is modulated by one molecule adsorbed on the graphite. In the cases of concern, the molecules are physisorbed onto the graphite via van der Waals interactions. These interactions are small compared to the intramolecular forces, since van der Waals forces are typically on the order of 1 kcal/mol per pair of atoms, while bond energies are on the order of 100 kcal/mol per bond. Thus, the shape of the molecular wavefunction for the adsorbed molecule is not expected to change significantly relative to that of the unadsorbed molecule. Also, the interaction between the tip and the molecule must be small, otherwise the molecule would be displaced by the tip, and it could not be observed in the experimental STM image. The orbital energies, on the other hand, are expected to be affected by the presence of two conductors in close proximity to the molecule. According to classical electrostatics,

the presence of the conductors results in a shift of the ionization potentials (IP) and electron affinities of the molecule, as described in Section 2.5.

3.2.1 Formalism

We will use the symbol $|t>$ to describe the wavefunction of the tip. $|t>$ belongs to a continuum of states with energies E_t and with a density of states $\rho_t(E_t)$. E_t^f indicates the Fermi energy of the tip. Similarly, $|g>$ indicates the wavefunction of the graphite support, with E_g, $\rho_g(E_g)$ and E_g^f defined as the corresponding energy, density of states and Fermi energy, respectively. Also, the adsorbed molecule is described by its MO $|k>$ (and occasionally $|l>$) having orbital energies E_k (E_l).

When a potential E_b, equivalent to a bias $-E_b$, is applied to the graphite support, electrons may flow from the more negative to the more positive side of the tunnel gap. When $E_g^f + E_b > E_t^f$ the electrons will flow from the states with energy $E_g \in (E_t^f, E_g^f + E_b)$ on the graphite to the states with energy $E_t \in (E_t^f, E_g^f + E_b)$ on the tip. The reverse is true when $E_g^f + E_b < E_t^f$. Throughout the chapter, the energy band into which the electrons are transferred under such a bias is denoted as the *conduction region.*

3.2.2 Coupling Potential

The perturbative potential, V, is the effective potential experienced by an electron in the region of space occupied by the molecule. Within the independent particle approximation, this potential is due to the Coulomb attraction of the nuclei, the average Coulomb repulsion from the molecular electrons, and the exchange interaction (from the Pauli principle).

V is exactly the potential used to solve the HF equation for the isolated molecule, so it acts on the MOs k as described in eq 3.1:

$$V^{HF}|k>=(H^{HF}-T)|k>=(E_k-T)|k> \tag{3.1}$$

where E_k is the orbital energy from the HF computation, T is the kinetic energy operator and H^{HF} is the HF hamiltonian.

We are interested in tunneling conditions corresponding to the experimental observations, for which the molecules dominate the STM image contrast. This observation indicates that the direct coupling between the tip and the graphite is much smaller than the coupling through the molecular states. Thus, it is legitimate to neglect the direct coupling of tip and graphite and to consider only the coupling through the MOs. This is equivalent to assuming that the unperturbed states of both tip and graphite overlap with the molecular wavefunction but not with each other. We also assume that there is no coupling between different states on the tip or on the graphite.

In this case, evaluation of all the relevant matrix elements for the coupling potential is readily

performed:

$$\begin{aligned}
&< t|V|g >= 0 && \text{assumed} \\
&< t|V|k >= E_k S_{tk} - T_{tk} && \text{from eq. 1} \\
&< g|V|k >= E_k S_{gk} - T_{gk} && \text{from eq. 1} \\
&< k|V|k' >= 0 && \text{because the MOs are HF solutions} \\
&< t|V|t' > \approx 0 && \text{assumed} \\
&< g|V|g' > \approx 0 && \text{assumed}
\end{aligned} \tag{3.2}$$

where S and T are the overlap and kinetic energy matrices, respectively.

3.2.3 Perturbation Theory: Nondegenerate Case

The tunneling probability will be evaluated through the use of time-independent perturbation theory.[15] When the perturbation is off, the tip, molecule and graphite do not interact. Thus, the unperturbed eigenstates are the functions $|t>$ and $|g>$ for the tip and the graphite along with the MO $|k>$ for the molecule. In the presence of the perturbation, the tip wavefunction is corrected by the first-order term of (3.3),

$$|t^{(1)}>= \sum_k \frac{V_{kt}}{(E_t - E_k)}|k> \tag{3.3}$$

and by the second-order term of (3.4),

$$|t^{(2)}>= \sum_k \frac{V_{gk}V_{kt}}{(E_t - E_k)(E_t - E_g)}|g> -\frac{1}{2}\sum_k \frac{|V_{kt}|^2}{(E_t - E_k)^2}|t> \tag{3.4}$$

The first correction due to the function $|g>$ appears in the second-order term. It is as if the functions $|t>$ and $|g>$ were coupled to first order by the effective element:

$$\mathcal{V}_{tg} = \sum_k \frac{V_{gk}V_{kt}}{(E_t - E_k)} \tag{3.5}$$

To first-order, this matrix element will be responsible for the tunneling current.

According to the Fermi golden rule, the number of transitions per unit time $d\omega_{gt}$ between an initial state $|t>$ and all final states $|g>$ with energy between E_g and $E_g + dE_g$ is[15]

$$d\omega_{gt} = \frac{2\pi}{\hbar}|\mathcal{V}_{tg}|^2 \delta(E_t - E_g)\rho_g(E_t)dE_g \tag{3.6}$$

The total current is then

$$I_{gt} = \frac{2\pi}{\hbar}\int \rho_t(E_t)dE_t \int \rho_g(E_g)dE_g \left|\sum_k \frac{V_{gk}V_{kt}}{(E_t - E_k)}\right|^2 \delta(E_t - E_g) \tag{3.7}$$

$$= \frac{2\pi}{\hbar}\int\left|\sum_k \frac{V_{gk}V_{kt}}{(E-E_k)}\right|^2 \rho_t(E)\rho_g(E)dE \tag{3.8}$$

where all integrals are over the conduction region. A more detailed description of the bias dependence is given in the appendix.

This approach provides an alternate method, relative to the traditional transfer hamiltonian formalism[7, 8] for obtaining an expression for the tunneling current under our conditions. In the transfer hamiltonian formalism,[7] the graphite wavefunction includes explicitly the contributions from the molecular states.[3] Its coupling with the tip is due, in the high bias limit, mainly to these contributions. In our approach, the same physical picture is described, but within the framework of a perturbation theory formalism. The results are thus consistent with the transfer hamiltonian theory and help to gain insight into the STM process of concern in the experimental data by focusing on the properties due to molecular states.

It should be noted that the common assumption that all of the STM current flows to or from states near the graphite Fermi level[3] does not hold in the high bias regime. The current involves all the states in the conduction region, hence an integration over energy in this region is required. This integration was performed for all of the molecular overlayers investigated during the course of this study.

3.2.4 Perturbation Theory: General Case

The above theory holds only for the case when all the energy differences in the denominators are large with respect to the coupling elements in the numerators. A more general treatment is described in this section. The molecular spectrum can be considered as a continuum with the following distribution:

$$S(E) = \sum_k V_{gk}V_{kt}\delta^{(\epsilon)}(E-E_k) \tag{9}$$

where $\delta^{(\epsilon)}(x)$ is such that

$$\lim_{\epsilon\to 0}\delta^{(\epsilon)}(x) = \delta(x) \tag{10}$$

and ϵ is a small quantity with the physical meaning of uncertainty in the energy. For instance, $\delta^{(\epsilon)}(x)$ can be taken to be a square function centered at $x = 0$ of width ϵ and height $1/\epsilon$.

It is now necessary to estimate the order of magnitude of ϵ. Whenever one of the orbitals falls in the conduction region, it is expected to be responsible for most of the observed current. A typical current used in STM imaging is $650pA = 9.8\times 10^{-8}$ au, so on average one electron leaves the orbital to contribute to the current every $1/9.8\times 10^{-8} \approx 1\cdot 10^{7}$ au of time. If we further assume that the orbital is doubly occupied half of the time, then each electron spends about 5×10^{6} au of time in the orbital, that is, the state with the electron in the orbital has an average lifetime of $5\cdot 10^{6}$ au,

which implies an uncertainty in its energy of $\hbar/(5 \times 10^6) = 2 \times 10^{-7}$ hartrees. Thus, a very rough order-of-magnitude estimate gives $\epsilon \approx 2 \times 10^{-7}$ and yields $\delta^{(\epsilon)}(0) \approx 5 \times 10^6$ au.

The number of transitions per unit time is then[15]

$$d\omega_{gt} = \frac{2\pi}{\hbar} \left| \int \frac{S(E)}{(E_t - E + i0)} dE \right|^2 \delta(E_t - E_g)\rho_g(E_t) dE_g \tag{11}$$

where the notation $i0$ indicates that in evaluating the integral, one must take the principal value plus one half the contribution from the residue on the integration path:

$$\int \frac{S(E)}{(E_t - E + i0)} dE = \mathcal{P} \int \frac{S(E)}{(E_t - E)} dE + i\pi S(E_t) \tag{12}$$

Since ϵ is small, the integral can be computed easily. When all orbitals are not degenerate with the tip, this expression becomes the same as the one found for the nondegenerate case. When one of the orbitals, for example $|l>$, is degenerate with the tip, its contribution to the principal value of the integral vanishes, so the integral becomes

$$\int \frac{S(E)}{(E_t - E + i0)} dE = \sum_{k \neq l} \frac{V_{gk} V_{kt}}{E_t - E_k} + i\pi V_{gl} V_{lt} \delta^{(\epsilon)}(0) \tag{13}$$

The number of transitions per unit time due to the degenerate orbital is then

$$d\omega_{gt} = \frac{2\pi}{\hbar} \pi^2 |V_{gl} V_{lt}|^2 \left[\delta^{(\epsilon)}(0)\right]^2 \delta(E_t - E_g)\rho_g(E_t) dE_g \tag{14}$$

The actual formula for the current is therefore

$$I \propto \int_{CR} \rho_t(E)\rho_g(E) \left| \sum_{k \notin CR} \frac{V_{gk} V_{kt}}{(E - E_k)} + i\pi \sum_{k \in CR} V_{gk} V_{kt} \delta^{(\epsilon)}(E - E_k) \right|^2 dE \tag{15}$$

where CR indicates the conduction region. Expanding the absolute value yields the desired expression:

$$I \propto \int_{CR} \rho_t(E)\rho_g(E) \left\{ \left[\sum_{k \notin CR} \frac{V_{gk} V_{kt}}{(E - E_k)} \right]^2 + \left[\pi \sum_{k \in CR} V_{gk} V_{kt} \delta^{(\epsilon)}(E - E_k) \right]^2 \right\} dE \tag{16}$$

where again the bias dependence (described explicitly in the appendix) is included implicitly into the energy terms of (16).

3.2.5 Practical Implementation

Several other approximations were made in order to simplify the practical implementation of this approach. These are described below.

First, the tip wavefunction was replaced by a single $2s$ oxygen orbital (using the STO-3G basis).[16] This orbital is similar in size to one lobe of a platinum d_{z^2} orbital, which would be the dominant orbital in computing the tip sample wavefunction overlap properties in a more complete quantum mechanical representation of the tip.

Second, the graphite wavefunction was replaced by an array of $2p$ carbon orbitals (STO-3G basis) that were centered onto a grid of points. The coupling between the graphite and each MO was obtained by summing the absolute contributions from each lobe on the grid. Tests with various grid spacings gave essentially identical results. This choice of graphite basis set is one of several possible methods to implement practically our algorithm. As long as the wavefunction decay with distance is reasonable and coupling is allowed to occur to all of the graphite states, the result is expected to depend little on the actual form of the graphite wavefunction, especially when the features of interest are the relative functional group contrasts of the various molecular STM images under high bias conditions.

The grid used in the simulation was deliberately chosen to be more dense than the carbons on the real graphite surface in order to avoid accidental couplings that might arise due to the position of the grid.

Third, since the continuum and the discrete states cannot be easily normalized using the same criteria, the unnormalized states were used for the continuum part. As a consequence, all coupling elements are only known up to a proportionality constant. Thus, the actual current cannot be estimated at each tip position, but only the ratio between currents at different points is obtained.

This is not a practical drawback at the present time since only the relative tunneling probabilities are of primary interest in modeling the observed image contrast. This approach does have the disadvantage that it requires tuning the tip-molecule distance based on the experimental images rather than on the intensity of the current. This approximation is a limitation to the method that could, in principle, be removed by explicitly taking into account the proper normalization of the continuum states. We prefer to keep the model as simple as possible and thus have not pursued such refinements at the present time.

Fourth, the orbital energies of the MOs used in (16) were shifted to account for the presence of two conductors in close proximity to the molecule. This required an estimate of the Coulomb term acting on the molecular state. Within the HF framework, the energy of an occupied orbital has the physical meaning of an IP: $E_{occ} = -IP = E_{molecule} - E_{cation}$. The presence of the conductors has little effect on $E_{molecule}$, but it stabilizes the cation, therefore E_{occ} becomes less negative, and the IP decreases. Another way to view this effect is the following: in vacuum, the IP is the energy needed to move one electron from the molecule to infinity, whereas in the presence of the conductors, the electron only must be moved from the molecule to the conductor: therefore, the IP decreases.

The stabilization effect can be computed with the method of image charges. Let the charge on

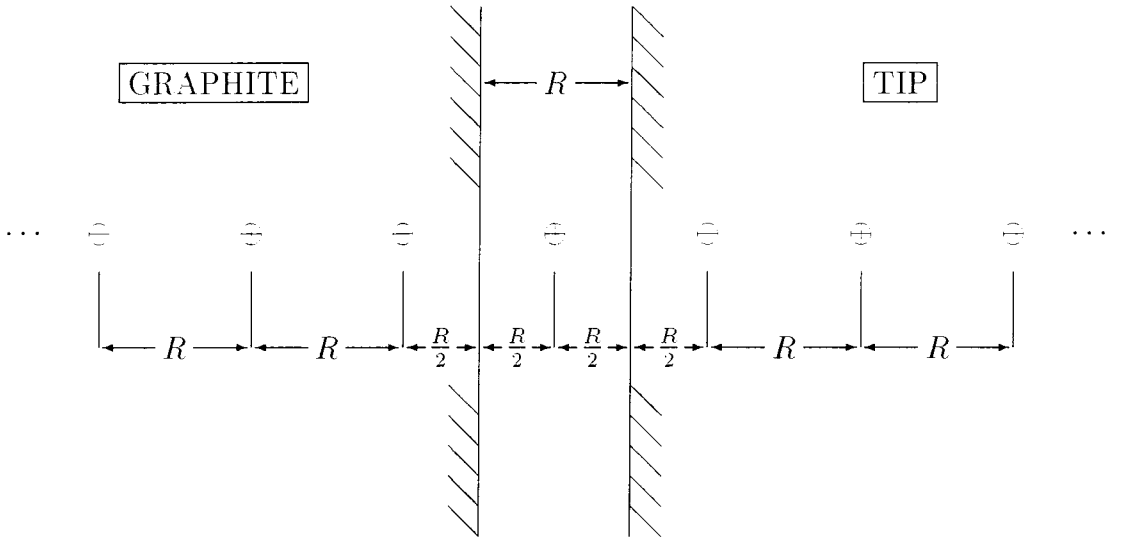

Figure 3.1: Charge distribution used to estimate the effect of the conductors on the orbital energies of the adsorbed molecule with the method of the image charges. The molecular ion is replaced by a point charge halfway between the tip and the graphite, seen as semi-infinite conductors. R is the tip-graphite distance.

the molecule be localized at its center of mass. The center of mass is estimated to be roughly half way between the tip and the graphite, which, for this purpose, are taken to be two semi-infinite conductors terminated by two parallel planes.

Let R be the distance between the two planes and $R/2$ the distance between each plane and the localized charge. In order for the potential to be zero on the surfaces of the conductors, a first pair of negative charges can be placed at a distance $R/2$ into each conductor. Each one of these charges will have positive images at a distance $3R/2$ into the opposite conductor, and so on, to infinity, as depicted in Figure 3.1.

The electrostatic stabilization of the original charge due to this series of images is (in au):

$$\Delta E = 2\left\{-\frac{1}{R}+\frac{1}{2R}-\frac{1}{3R}+\cdots\right\} = \frac{2}{R}\sum_{n=1}^{\infty}\frac{(-1)^n}{n} = -\frac{2\log(2)}{R} \tag{17}$$

Thus, the occupied orbital energies used in the computation of the current are shifted by adding $2\log(2)/R$, where R is the distance between the tip and the graphite.

The HF virtual orbitals, on the other hand, describe the energy required to add an electron to the molecule and have the physical meaning of electron affinities: $E_{virt} = E_{anion} - E_{molecule}$. In this case, the anion is stabilized by the presence of the two conductors but the molecule is not, so the virtual orbital energies must be corrected by subtracting the quantity $2\log(2)/R$. This treatment is not rigorous, as we do not account for the different shapes and polarizabilities of different orbitals. However, it is very simple and it gives a reasonable estimate of this Coulombic correction term.

The different behavior of occupied and virtual orbitals is a consequence of the definition of orbital energy arising from the HF treatment. All HF orbital energies include the interactions of an electron in the orbital with the nuclei and with all the other electrons in the system. For a molecule containing N electrons, for instance, the energy of an occupied orbital includes interactions with the remaining $(N-1)$ electrons while the energy of a virtual orbital includes interactions with all N electrons. Occupied orbital energies, therefore, describe the removal and virtual orbital energies describe the addition of one electron with respect to the state for which the orbitals were optimized.

Fifth, orbitals that fall in the conduction region must be treated separately. During the flow of current, their occupations and their orbital energies are not easily defined. A simple approximation is to assume that they fall in the middle of the conduction region. Notice also that orbitals that are occupied in the isolated molecule, but that fall above the conduction region, are not well-described and hence should be treated as conduction orbitals.

Sixth, it is necessary to estimate the potential distribution when a bias is applied across the tip-sample gap. When the tip, molecule, and graphite are brought together, the Fermi levels of the three components tend to become equal at the interface.[17] The rigorous description of this effect is rather complicated, requiring sophisticated computational techniques that would considerably increase the cost of the simulation. For the situation of interest, the Fermi energies of the metal tip and of the graphite were assumed to be equal to each other. Additionally, as derived previously, the bias was assumed to be distributed in the tip-sample gap such that the molecule experiences 1/2 of the bias potential.[2, 18]

To account for the effects of the initial charge equilibration on the energies of the MOs, all orbital energies were considered to be shifted from their values in vacuum by an amount λ. This quantity represents the difference between the computed HF orbital energies, rescaled to account for the presence of the conductors, and the real orbital energies of the adsorbed molecules during the STM imaging experiment.

λ includes contributions from two very different phenomena. One contribution to λ arises from the inability of HF calculations to reliably predict IPs. This contribution can be evaluated by comparison of the highest occupied molecular orbitals (HOMO) energy obtained from the HF calculation to a reliable value for the IP of the molecule, obtained either from experimental data or from high level calculations. For a number of small molecules, the energies of both the molecules and the corresponding cations were computed at the HF and MP2 level, and the resulting IPs, as well as the experimental ones whenever available, are displayed in Table 1. Although the HOMO energy obtained from the HF calculation tends to overestimate the true IP by about 1 eV, the error changes considerably for different molecules. The correction for this effect was estimated for every class of molecules, and this correction was included in the value of λ for each different molecule. For consistency, the value chosen for the correction was taken as the difference between the HF HOMO

TABLE 1: Ionization Potentials (eV)

Molecule	IP[a] (Koopmans)	IP[b] (HF)	IP[c] (MP2)	IP[d] (exper)
$CH_3(CH_2)_4CH_3$	11.57	10.12	10.44	(10.22)[e]
$CH_3(CH_2)_3OH$	11.87	9.24	10.56	10.37-10.44
$CH_3(CH_2)_3F$	12.53	11.10	11.30	—[f]
$CH_3(CH_2)_3Cl$	11.42	9.96	10.60	10.84
$CH_3(CH_2)_3Br$	10.55	9.38	9.75	(10.15)[e]
$CH_3(CH_2)_3I$	9.62	8.66	8.99	9.5
$CH_3(CH_2)_3CN$	11.92	10.48	12.05	—[f]
$C_2H_5CF_3$	14.02	12.85	12.72	—[f]
$C_2H_5COC_2H_5$	11.14	7.97	9.55	9.52
$C_2H_5NHC_2H_5$	9.87	7.37	8.54	8.63-8.68
$C_2H_5NH_2$	10.47	8.19	9.33	9.47-9.50
$C_2H_5OC_2H_5$	11.32	8.46	9.85	9.59-9.70
$C_2H_5SC_2H_5$	9.00	7.44	8.23	7.45-8.44
C_2H_5SH	9.60	8.21	8.94	(9.15)[e]
$C_2H_5SSC_2H_5$	9.13	8.06	8.15	8.70-8.85
CH_3COOH	11.90	8.78	10.35	(10.66)[e]
$C_2H_5CCC_2H_5$	9.37	7.90	9.14	(9.32)[e]
$C_2H_5CHCHC_2H_5$	8.74	7.35	8.69	9.14

The values are vertical ionization potentials in eV.
[a] Estimate based on Koopmans theorem (HF orbital energy) with 6-31G** basis set.
[b] Estimate obtained by comparing the total HF/6-31G** energies of the molecule and the cation.
[c] Estimate obtained by comparing the total MP2/6-31G** energies of the molecule and the cation.
[d] Experimental value from ref. [25].
[e] Adiabatic ionization potential.
[f] Data not available.

energy and the IP that was computed at the MP2 level.

The other contribution to λ arises from a need to account for possible energetic differences between the energy levels of molecules adsorbed onto graphite and those in vacuum. It is likely that the reference energy for a molecule (the chemical potential of the electrons in the molecule) changes from its value in vacuum when the molecule instead is adsorbed on graphite, surrounded by solvent, and approached by the tip. For the substituted alkane chains under similar tunneling conditions (i.e., similar bias and tunneling current), this component of λ was chosen to best reproduce in general the entire set of observed images and then was not varied for calculations on individual systems.

Seventh, the density of states for the tip $\rho_t(E)$ was assumed to be a constant in the conduction region. The density of states for the graphite $\rho_g(E)$ was assumed to be a parabola having a vertex at the initial value of the graphite Fermi level,[19] $\rho_g(E) \propto (E - E_f)^2$.

Adopting these approximations, the STM current is then

$$I \propto \int_{CR} (E_f - E)^2 \left[\sum_{k \notin CR} \frac{V_{gk} V_{kt}}{(E - E_k)} \right]^2 dE + \int_{CR} (E_f - E)^2 \left[\pi \sum_{k \in CR} V_{gk} V_{kt} \delta^{(\epsilon)}(E - E_k) \right]^2 dE \quad (18)$$

where again the bias dependence is implicitly contained in the energy terms of (18). The first of these integrals is computed numerically (e.g., using Simpson's rule), and the second one uses the estimates of E_k described above and the value of $\delta^{(\epsilon)}(E - E_k)$ obtained in Section 2.4.

3.2.6 General Procedure

For every chemical species, one molecule was laid onto a rigid graphite slab and the molecular geometry was optimized using the DreidingII FF[20] with charges estimated using charge equilibration.[21] Two more molecules were then added, parallel to the first one and sandwiching it, at a distance of about 4.5 Å. The molecular geometry was then reoptimized. The distance of 4.5 Å was chosen because it is close to the one observed experimentally, both in STM images[2] and in low-angle X-ray diffraction experiments of alkane and alkanol overlayers on HOPG.[22]

The central molecule was then isolated without changing its geometry. All alkyl chains were truncated four carbons away from any functional group, and the cleaved bonds were saturated with hydrogens. The resulting molecules were then checked for symmetry elements. The molecules that were found to be symmetric (with a tolerance of 0.04 Å) were symmetrized in order to speed up the Hartree-Fock computation. A standard HF computation was then performed on the resulting molecules using the 6-31G** basis set.[23] The choice of the basis set was motivated by the desire for reasonably accurate orbital energies.

To simulate an STM scan, a grid of 26 × 26 points was positioned to correspond to the graphite surface in the FF computation. All of the coupling elements with the graphite were then computed

placing one carbon $2p$ orbital at each grid point. The tip was positioned on a grid of 51×51 points that was positioned parallel to, and at a fixed distance from, the plane of the graphite grid. For each position of the tip, the coupling elements were computed and the tunneling current estimated assuming a bias of -1 eV. The resulting data were then used to produce three-dimensional plots or contour diagrams of the current. This approach simulates a constant height STM image, and was used to calibrate the tip-graphite distance and to establish the value of the parameter λ. For each molecule, a constant current simulation was also performed, in which the tip was allowed to move in a direction perpendicular to the graphite in order to adjust the current to a fixed value. The tip displacement was then plotted with respect to an arbitrary plane that was parallel to the graphite surface. These simulations are three to four times more computationally expensive than the constant height simulations, but resemble more closely the experimental STM technique. Qualitative agreement was observed between the computed constant height and constant current images for all the cases studied in this work.

In order to facilitate interpretation of the results in terms of electronic and geometric effects, the overlap between the tip wavefunction and the occupied MOs was also evaluated. The resulting images have no experimental equivalent, but represent what the STM image would look like if only the geometry of the molecule were mapped while all electronic effects were ignored. The comparison of these images with the results of the complete simulations will point out whether topographic or electronic effects are primarily responsible for the features that are observed in the experimental and computed STM images.

The tip-molecule distance that was used for the constant height simulations, and the current used in the constant current simulations, were each chosen to reproduce as closely as possible the features that were observed experimentally. A tip-molecule distance of 7 au $\approx$3.7 Å was selected for the constant height simulations. At this distance, the maximal current observed for the alkane molecules is close to 0.001 arbitrary units (only relative current densities are computed in the present model) and this value was used for the constant current simulations. For much shorter distances, the resulting images seem to be determined mainly by the topology of the molecule, while at much longer distances the computed resolution decreased below that observed experimentally.

In all constant current plots, the tip was not allowed to get too close to the graphite, so these plots produce features that appear to be bumps on a flat surface. In previous simulations reported in the literature,[3] STM images have been related to the LDOS at a distance of 0.5 Å from the adsorbed molecule. We believe such distances are unrealistically small to describe actual STM measurements. In our work, the distance corresponding to the flat surface was set to be 14.5 bohrs for molecules oriented with their carbon-carbon skeletons parallel to the graphite surface plane and 15 bohrs for molecules having their carbon-carbon skeletons oriented perpendicular to the plane of the graphite surface. These values correspond to a tip-molecule distance of about 2.9 Å.

The value of the parameter λ was chosen to best reproduce the experimental images. While the value of λ has little or no effect on most molecules, it plays a fundamental role for the molecules having their HOMOs close to the conduction region. After correcting for the difference between the HOMO energy and the MP2 IP, as reported in Table 1, the second contribution to λ was estimated by the value needed to bring the HOMO of the amines into the conduction region and to leave the HOMO of the alkyl bromide at lower energy. This condition is satisfied for any correction between 1.3 and 1.8 eV, assuming a tip-molecule distance of 7 au. We arbitrarily selected a correction of 1.5 eV. This value was fixed for all the simulations, based on the assumption that it should be approximately equal for all the molecules of concern.

3.3 Results

The orientation of the carbon-carbon skeletons of the alkyl chains relative to the graphite surface plane must be carefully considered in order to accurately model the STM images that have been observed experimentally. In the discussion that follows, the term flat will be used to indicate adsorption orientations in which the carbon-carbon skeleton of the alkane chain lies parallel to the plane containing the graphite surface, while the term vertical will be used to indicate the situation in which the carbon-carbon skeleton is oriented perpendicular to the graphite surface plane. Also, since the tip is assumed to be above the graphite, down and up will be used to describe atomic positions that are located toward the graphite and toward the tip, respectively.

3.3.1 Alkanes

To investigate the geometry and packing of adsorbed alkanes, the molecule $CH_3(CH_2)_{33}CH_3$ was considered, since it was the alkane that was imaged experimentally with the STM.[2] According to the results from the FF study, a single *trans-* $CH_3(CH_2)_{33}CH_3$ molecule adsorbs on graphite in the flat orientation, with the vertical orientation being less stable by 8 kcal/mol. The adsorption energy (from the gas phase) for $CH_3(CH_2)_{33}CH_3$ was computed to be on the order of 70 kcal/mol. In these computations, only the all *trans-* conformation was considered. This was justified because conformations with *gauche-* bonds were likely to be significantly less favorable energetically, and because the experimental STM[2] and X-ray diffraction[22] data strongly suggest that the alkanes are adsorbed in an all *trans-* conformation onto the graphite surface.

When three *trans-* $CH_3(CH_2)_{33}CH_3$ molecules are adsorbed from the gas phase, each pairwise interaction between neighboring molecules was computed to further stabilize the system by about 23 and 56 kcal/mol in the flat and the vertical orientations, respectively. Consequently, for a three-molecule overlayer model, the vertical orientation is computed to be more stable by an energy difference of 25 kcal/mol.

The experimental images indicate that the molecules are generally adsorbed in the flat orientation.[2, 3] Although the vertical orientation is computed to be more stable, if the monolayer is built by adding one molecule at a time and by letting it migrate on the graphite surface, it is conceivable that the system would be trapped into the flat orientation. Migration of a single $CH_3(CH_2)_{33}CH_3$ molecule on the graphite surface was computed to have a barrier of 1-2 kcal/mol. However, the barrier to flip one $CH_3(CH_2)_{33}CH_3$ molecule into the vertical orientation is estimated to be around 18 kcal/mol, making this process unlikely at room temperature. This proposed nucleation process is similar to one that has been recently observed in an STM study of the growth dynamics of self-assembled thiol monolayers on gold.[24] An alternative possibility that was not explored in the present calculations is that since the adsorption occurs from solution, differential solvation plays a significant role in determining the energetically favored orientation of the molecules in the graphite overlayer.

Instead of carrying out more extensive simulations to include both dynamical effects and solvation effects, both orientations of the alkane were investigated in order to evaluate which produced computed STM images that more closely matched the experimental data. The images for $CH_3(CH_2)_7CH_3$ in the vertical orientation are reported in Figure 3.2A. The constant current image of Figure 3.2A clearly does not match the high resolution STM image observed experimentally for alkanes on HOPG.[2] The constant height and the constant current images show spots corresponding to the hydrogens closest to the tip, leading to a rectangular pattern that is predominantly due to the geometry of the molecule, similar to the conclusions of a previous extended Hückel level analysis of this system.[3] Our calculations produced an average distance between maxima in the constant current mode of 2.59 Å in the direction along the backbone and an average distance of 1.57 Å between nearest neighbors.

The STM images predicted for the flat molecule $CH_3(CH_2)_6CH_3$ at a bias of -1 eV are reported in Figure 3.2B. The constant current and constant height images of the alkane in this orientation were similar to each other, and both displayed patterns that closely match the pattern produced by the geometric locations of the hydrogens that were closest to the tip. This effect can be seen more clearly by comparison of the image in Figure 3.2B to the overlap plot of Figure 3.2C. This comparison indicates that the molecular topography alone is sufficient to explain the qualitative aspects of the computed STM image of this system.

The images of Figure 3.2B are in excellent agreement with the experimental images obtained for alkanes on graphite.[2] In the constant current simulation, the average distance between subsequent spots along the alkane chain is 2.61 Å and the average distance between spots along the direction of the molecule is 2.56 Å, whereas the experimental data are 2.35 Å between spots along the chain and 2.54 Å between spots along the direction of the molecule. The positions of the spots observed experimentally are not in exact agreement with those in the simulation presumably due to the approximations contained in both the model and the computation.

(A) Vertical $CH_3(CH_2)_7CH_3$ at $-1.0\ eV$ Constant current

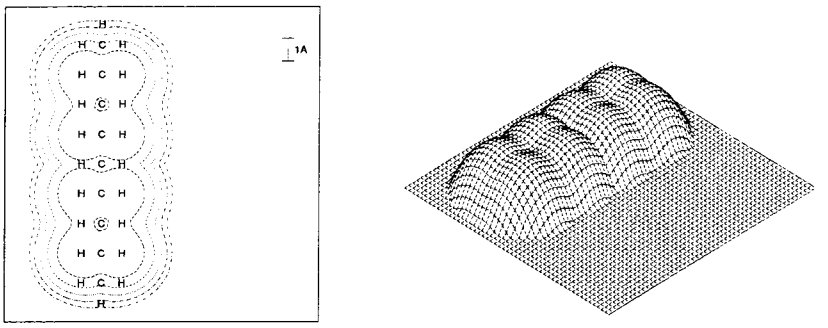

(B) Flat $CH_3(CH_2)_6CH_3$ at $-1.0\ eV$ Constant current

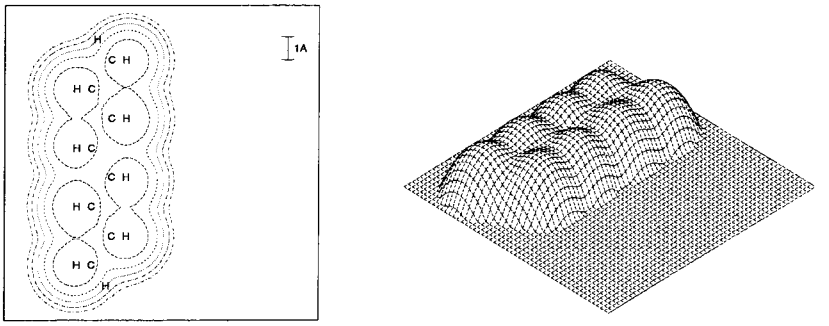

(C) Flat $CH_3(CH_2)_6CH_3$ at $-1.0\ eV$ Overlap Only

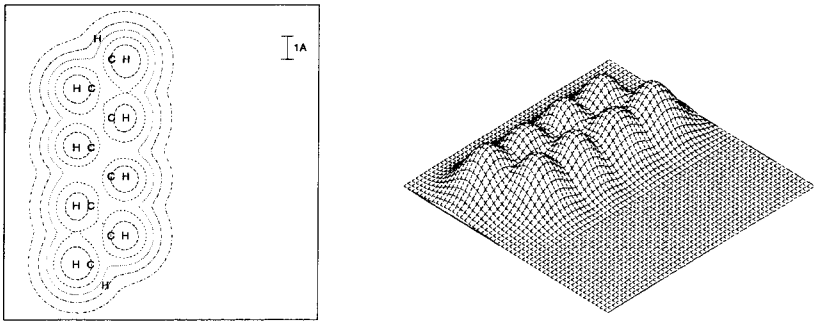

Figure 3.2: Computed STM images of an alkane molecule adsorbed on graphite. The contour levels are at 1/6, 2/6, 3/6, 4/6, and 5/6 of the maximum peak of each plot; the same spacing criteria for contour levels is used for all the contour plots of the paper. 3-D plots are shown to the right of the contour plots. The bias is -1 eV in all panels of Figures 2-16 unless otherwise noted. In (A), the vertical orientation is assumed, while (B) and (C) depict results for the flat orientation. (A) Constant current simulation; the plot represents the tip displacement perpendicular to the graphite surface. The maximum displacement is 1.71 a.u. (B) Constant current simulation in the flat orientation. The maximum displacement is 1.47 a.u. (C) Simulation of only the overlap of the tip with the occupied MOs at each tip position (see text for details). The maximum current is 0.050 arbitrary units.

It is also of interest to examine the relative contribution of the occupied and unoccupied orbitals to the overall tunneling current. Since the occupied orbitals of the alkane are very stable, the computations indicate that the current is determined mainly by the virtual orbitals. A simple interpretation of this behavior is that the tunneling electrons behave as low energy electrons elastically scattered by the adsorbed molecules. Because the same coupling is present in both biases, the images are predicted to be symmetric with bias voltage,[2, 18] in accord with experimental observations.[2]

3.3.2 Alkanols

Since the experimental STM images show that alkanols lay flat on HOPG,[2] only the flat adsorption orientation was considered computationally for these systems. The molecular geometry of the adsorbed alkanol was computed for the molecule $CH_3(CH_2)_{11}OH$ and the *ab initio* computation of the STM image was carried out on the molecule $CH_3(CH_2)_3OH$.

Three conformations were investigated for the flat orientation of $CH_3(CH_2)_{11}OH$ on graphite. For one adsorbed molecule, the most stable conformation was the one with the OH group *trans* to the alkyl chain. This conformation was computed to have an adsorption energy of 26.3 kcal/mol from the gas phase. The two *gauche*-conformers, in which the OH group was either pointing toward the graphite (OH down) or toward the tip, denoted as OH up, were less stable by 3.4 and 3.0 kcal/mol, respectively. For three $CH_3(CH_2)_{11}OH$ molecules adsorbed on graphite, the *trans*-conformer was again the most energetically favored in the computations, while the *gauche*-conformers were 3.2 and 3.1 kcal/mol higher in energy, respectively.

Figure 3.3A displays the computed STM images for the most energetically favorable *trans*-conformer of $CH_3(CH_2)_3OH$ at a bias of -1 eV in the flat orientation. The simulation shows that the alcohol is dark with respect to the alkyl chain, in accord with experiment. Additionally, the image of the chain is dominated by the spots corresponding to the hydrogen atoms closest to the tip, as in the case of unsubstituted alkanes.

The average distance between spots is 2.63 Å along the direction of the molecule and 2.62 Å between nearest neighbors. The average angle between spots imaged on the alkyl chain is 60.2°. The experimental values for $CH_3(CH_2)_{13}OH$ are 2.57 Å, 2.36 Å, and 61° respectively.[2] The difference between these computed values and the ones obtained for the unsubstituted alkane can be attributed to the fact that the alkyl chain used in the computational modeling of the alkanol overlayer is shorter, and hence is less representative of the real system. Again the virtual orbitals were primarily responsible for the contrast between the OH group and the hydrogens in the methylene chain.

The *gauche*-conformers of the alkanol produced significantly different computed STM images. The OH group in the computed STM plot for both *gauche*-isomers is brighter than the spots in the alkyl chain, although the computations indicate that the oxygen atom is not observed directly by the STM for either conformation of the alkanol. For the OH down conformation, the α-hydrogen

$CH_3(CH_2)_3OH$ Constant current

(A) Flat

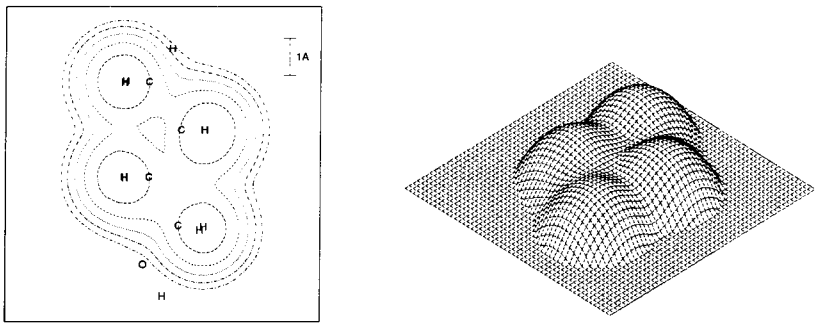

(B) $-OH$ down

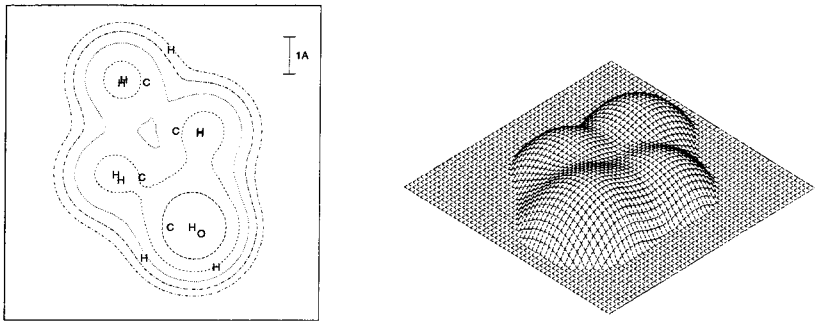

(C) $-OH$ up

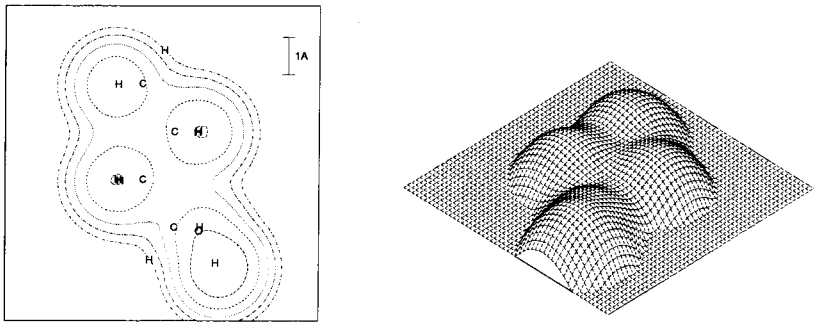

Figure 3.3: Computed constant current STM images of an alcohol molecule laid flat on the graphite surface. (A) The -OH group is *trans-* to the alkyl chain. The maximum value of the plot is 1.00 a.u. (B) The -OH group is *gauche-* to the alkyl chain and it points toward the graphite. (C) The -OH group is *gauche-* to the alkyl chain and it points away from the graphite. The maximum value of the plots in (B) and (C) are 1.32 and 1.12 a.u., respectively.

is forced up toward the tip and becomes bright due to a topographic effect (Figure 3.3B). For the OH up conformation, the hydrogen atom of the OH group is close to the tip and is thus computed to be imaged as a bright spot (Figure 3.3C). Since the *gauche*-conformations produce computed images that do not agree with experimental observation, but the computed STM image of the *trans*-conformation does agree with the data, it is reasonable to conclude that the more energetically favored *trans*-conformer was in fact being imaged experimentally in the work of Claypool et al.[2]

3.3.3 Halogenated Alkanols

For these molecules, only the flat orientation was considered. This was justified by the observation that the experimental images of halogenated alkanols show the same packing as that displayed by unsubstituted alkanols,[2] for which the high resolution STM images clearly revealed a flat orientation.[2] The parameters of the adsorbed molecules were determined for $X(CH_2)_{12}OH$, where $X = F$, Cl, Br, and I, whereas the *ab initio* STM image computations were performed on the smaller molecules $X(CH_2)_3CH_3$.

Figure 3.4 depicts the images computed for these adsorbates at a bias of -1 eV. These images display the results obtained for the most energetically stable conformation, in which the halide was in a *trans*-conformation relative to the alkyl chain. The images show that the functional groups F, Cl, and Br appear dark in the STM images relative to the alkyl chain, while I is much brighter than any other part of the iodoalkanol. These predictions are in excellent agreement with the experimental observations.[2]

In the case of I, the two HOMOs fall in the conduction region. The molecule then becomes a conductor and most of the current goes through the lone pairs on the iodine.

In the case of F, Cl, and Br, both the occupied and virtual orbitals are far in energy from the conduction region. As the virtual orbitals reach farther out from the molecule than the occupied orbitals, they couple better with the tip and with the graphite. Consequently, the virtual orbitals are computed to be responsible for most of the current. These halogens cannot transmit current, and thus appear dark in the STM image contrast, because they have no low energy virtual orbital available. To illustrate these effects, Figure 3.5 compares the constant height images obtained from the entire STM image computation to those computed for the alkyl bromide and alkyl iodide adsorbates when only the occupied or the virtual orbitals are considered. When only the occupied orbitals are considered, both Br and I are bright, even though I is much brighter.

Computations were also performed for two other conformations of the alkyl bromide, both of which had the Br in a *gauche*-position relative to the alkyl chain. In one conformation, the Br group was pointing toward the graphite (Br down) and in the other conformation the Br was pointing away from the graphite (Br up).

For a single adsorbed molecule, the adsorption energy (from the gas phase) of the *trans*-Br

(A) $CH_3(CH_2)_3F$

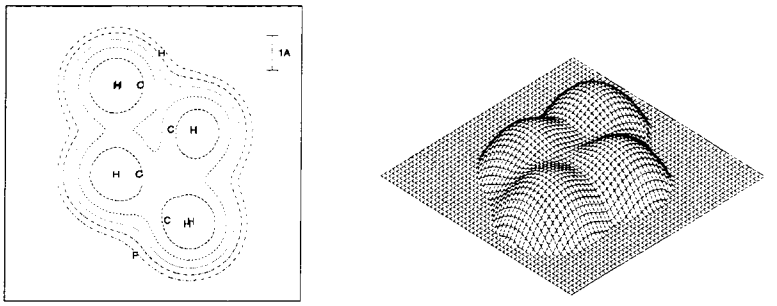

(B) $CH_3(CH_2)_3Cl$

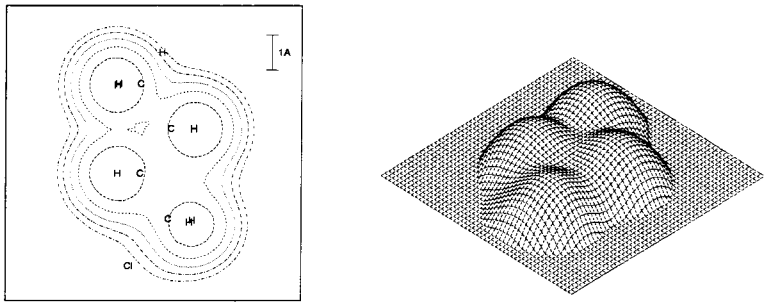

(C) $CH_3(CH_2)_3Br$

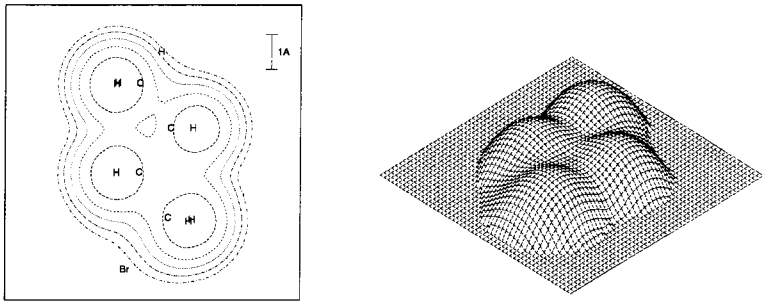

(D) $CH_3(CH_2)_3I$

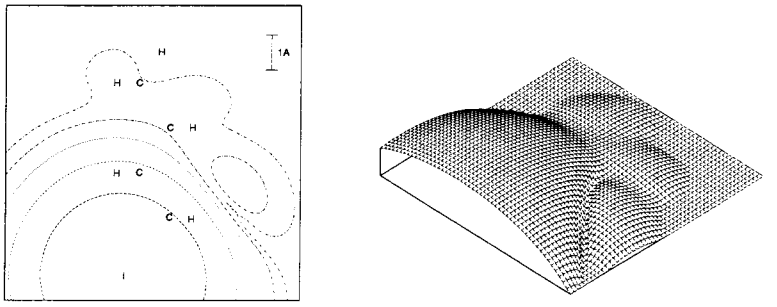

Figure 3.4: Computed constant current STM images of halobutanes laid flat on graphite. (A) Fluoro-butane; (B) Chloro-butane; (C) Bromo-butane; (D) Iodo-butane. The maximum values for the plots are 0.99, 0.99, 0.98, and 5.16 a.u., respectively.

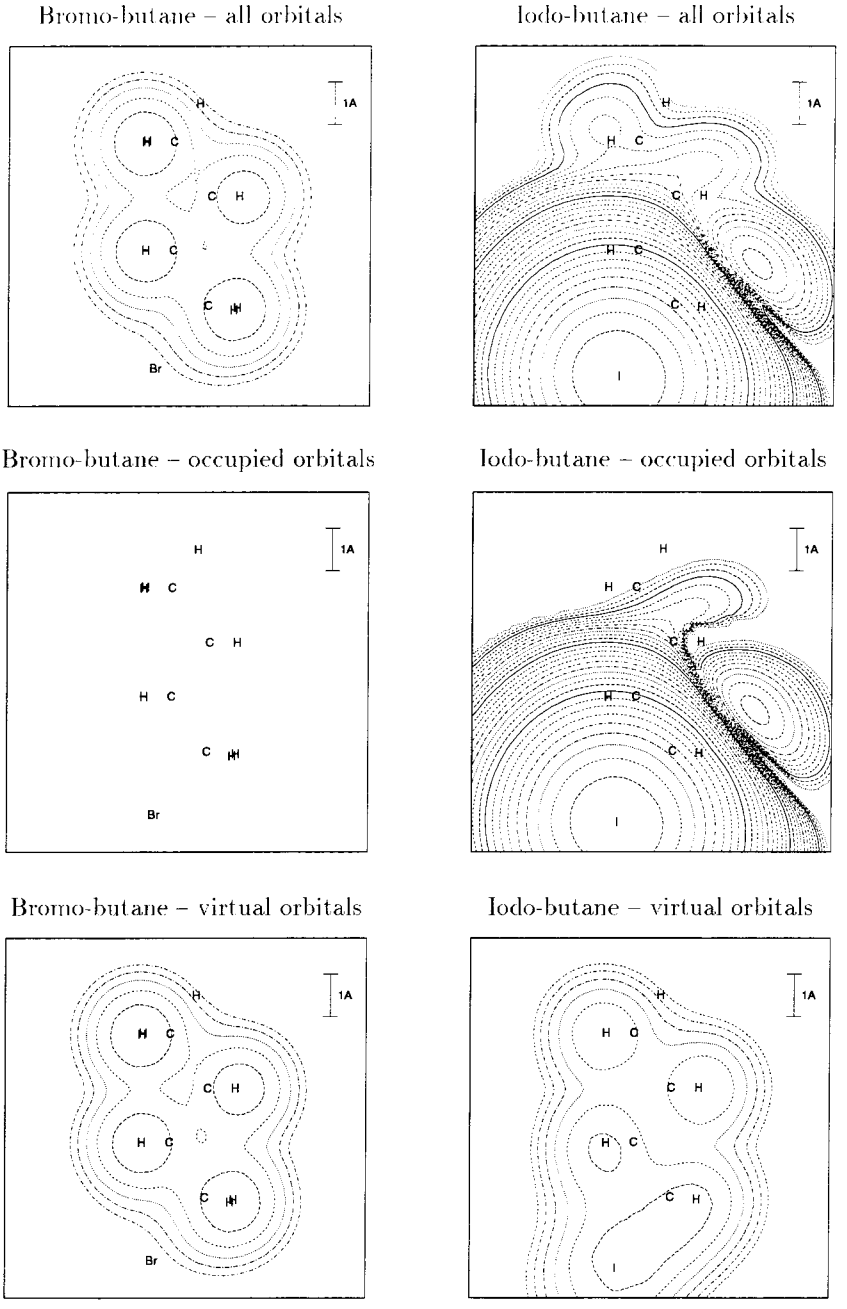

Figure 3.5: Computed STM images of bromo- and iodo-butane in the constant current mode. The top two plots represent the total current transmitted. The contributions to the current due to the occupied (center) and the virtual (bottom) orbitals alone is reported to show the similarity between the two molecules. To illustrate the differences between the two molecules, the same contour levels and reference distance were used in all plots. Each contour line represents a tip displacement of 1/6 a.u. The zero corresponds to a tip-graphite distance of 14.5 a.u. (i.e., a tip-molecule distance of about 2.9 Å) and only positive displacements are computed. In the bromine, the total current is dominated by the virtual orbitals while in the iodine it is dominated by the occupied orbitals.

(A) $CH_3(CH_2)_3Br$ *Br* down

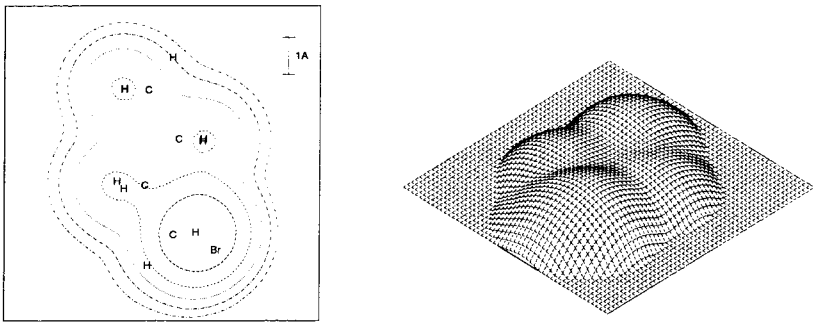

(B) $CH_3(CH_2)_3Br$ *Br* up

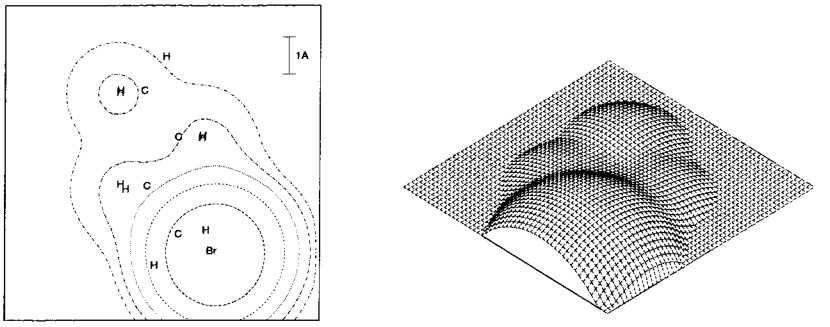

Figure 3.6: Computed constant current STM images of bromo-butane on graphite. (A) The Br is *gauche* to the alkyl chain and points toward the graphite. (B) The Br is *gauche* to the alkyl chain and points away from the graphite. The maximum values in the plots are 1.91 and 2.95 a.u., respectively.

conformation was 28.9 kcal/mol, whereas the *gauche*-conformers were found to be less stable by 3.6 kcal/mol (Br down) and 3.5 kcal/mol (Br up). For three adsorbed molecules, the *gauche*-conformers were less stable than the *trans* by 11.9 kcal/mol (Br down) and 13.7 kcal/mol (Br up).

STM simulations were performed on both of these *gauche*- conformations. As displayed in Figure 3.6, changing the conformation from a *trans* to a *gauche*-alkyl halide is predicted to effect a large and diagnostic change in the STM image. Although the Br is dark relative to the alkyl chain in a *trans*-conformation, it is predicted to be bright in both *gauche*-conformations. With the Br down, the Br pushes up one of the hydrogen atoms on the α carbon, and this topographic effect causes the α hydrogen atom to become bright in an STM image (Figure 3.6A). With the Br up, the Br atom itself is bright (Figure 3.6B). Neither of these predictions correspond to the experimental data on the alkanol bromide, which are instead in accord with the computational prediction that the more energetically stable *trans*-conformation is being imaged in the STM experiment. The prediction that a bromide group would change from dark to bright in an STM image if its conformation changed from *trans* to *gauche* is consistent with the image-contrast reversal that has been recently reported for bromide groups after sustained imaging of alkyl bromide overlayers on graphite substrates.[4]

3.3.4 Fluorinated Alkanols

Figures 3.7 and 3.8 depict the STM images that were computed for the CF_3 and C_3F_7 functional groups. Both of these molecules were considered in the flat adsorption orientation. As observed experimentally, all three functional groups appear darker than the alkyl chain.

In these molecules, some fluorine atoms are closer to the tip than any other atom in the alkyl chain. Despite this topographic effect that should cause the flourine atoms to be bright in the STM contrast, they are dark both theoretically and experimentally. This electronic effect results from the fact that the occupied orbitals describing the wavefunction in the fluorine region are computed to be very strongly bound while the virtual orbitals are very far above the vacuum level. Hence, the current due to these orbitals is very small, despite a good overlap with the tip wavefunction, and these functional groups thus appear to be dark in STM contrast.

3.3.5 Ethers

The adsorption orientation on a graphite surface was determined for the long chain ether $CH_3(CH_2)_{15}O(CH_2)_{15}CH_3$. According to FF simulations, a single molecule prefers to be adsorbed in the flat orientation but the vertical orientations are computed to be less stable by 9.3 and 9.5 kcal/mol when the oxygen is pointing down and up, respectively. When the molecules are packed with a density close to the experimental one, the vertical orientation with oxygen pointing up is computed to be the most stable, followed by the vertical orientation with oxygen pointing down (1 kcal/mol) and the flat (8.2 kcal/mol) orientation. STM images for all three possibilities were therefore simulated.

Figure 3.9 reports the results obtained for a bias of -1 eV for the molecule $O[(CH_2)_3CH_3]_2$. In the vertical orientation with the oxygen down (Figure 3.9A), the ether is bright, due to the hydrogens on the α carbons. This image is thus not in agreement with experiment.

In the flat orientation (Figure 3.9B), the ether is dark and it appears similar to a missing hydrogen in the alkyl chain. In the vertical orientation with the oxygen pointing up (Figure 3.9C), the ether is also dark. In this orientation, the dark area is bounded by the spots corresponding to the hydrogens on the β carbons with respect to the oxygen.

Since by itself the observed STM contrast does not distinguish between the flat and O up orientations, it would be useful to obtain independent support for the orientational assignment suggested above. Such support can be obtained by inspection of the molecular packing arrangement of the ether overlayer. As discussed by Claypool at al.[2], the characteristic angle θ is expected to be 0° for the sterically favored packing arrangement in the flat orientation (c.f. Figure 20B in ref. [2]) and is expected to be 26° for the sterically favored packing in the vertical orientation (c.f. Figure 20A in ref. [2]). The option for producing $\theta = 26°$, arising from the flat orientation with an offset of adjacent

Flat $CH_3(CH_2)_3CF_3$ at $-1.0\,eV$

(A) Constant current

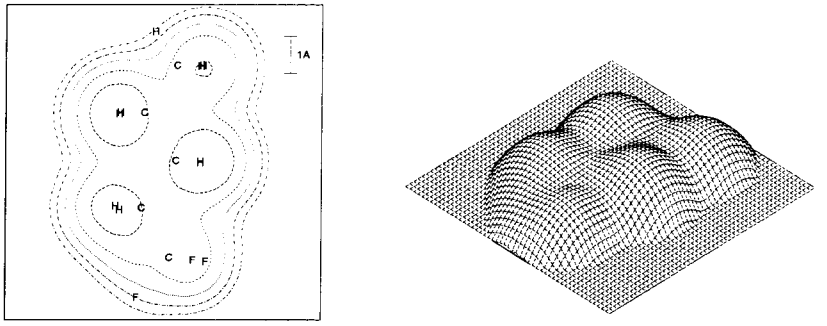

(B) Constant height

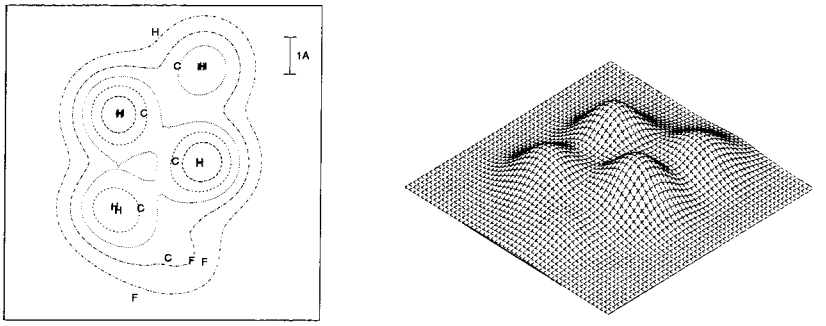

(C) Constant height – Overlap only

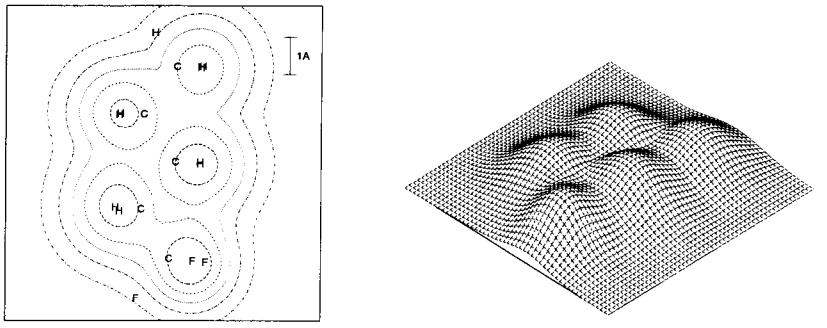

Figure 3.7: Computed constant current STM images of $CH_3(CH_2)_3CF_3$ laid flat on the graphite surface. The maximum values for the three plots are: (A) 1.12 a.u.; (B) 0.00038 arbitrary units; and (C) 0.054 arbitrary units.

Flat $CH_3(CH_2)_3(CF_2)_2CF_3$ at -1.0 eV

(A) Constant current

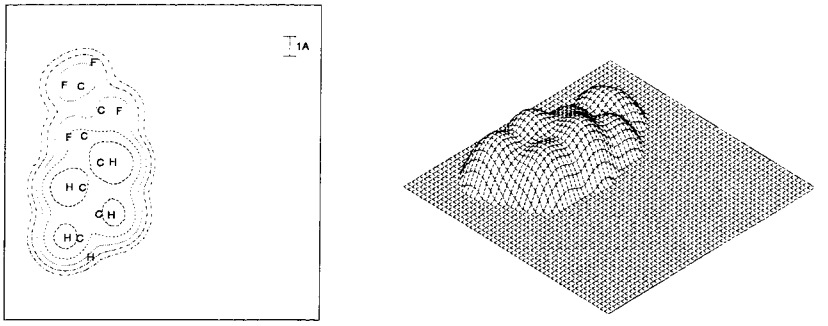

(B) Constant height

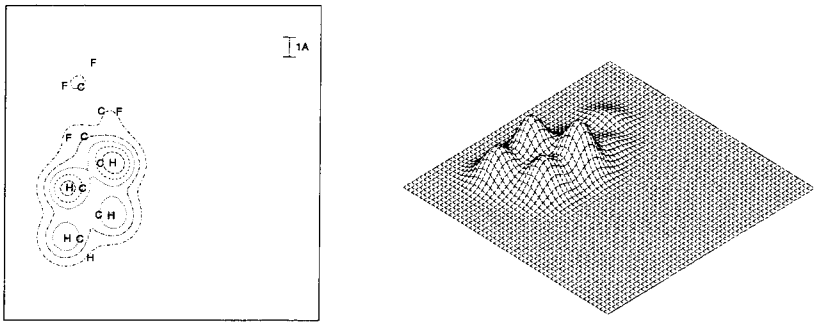

(C) Constant height – Overlap only

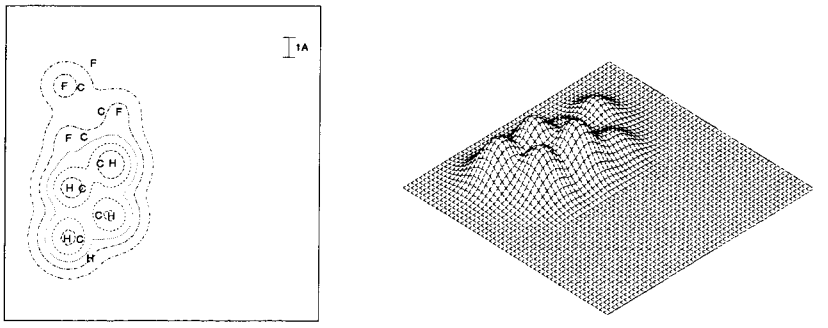

Figure 3.8: Computed constant current STM images of $CH_3(CH_2)_3(CF_2)_3CF_3$ laid flat on the graphite surface. The maximum values for the three plots are (A) 1.55 a.u.; (B) 0.0011 arbitrary units; and (C) 0.097 arbitrary units.

$CH_3(CH_2)_3O(CH_2)_3CH_3$

(A) Vertical, O down

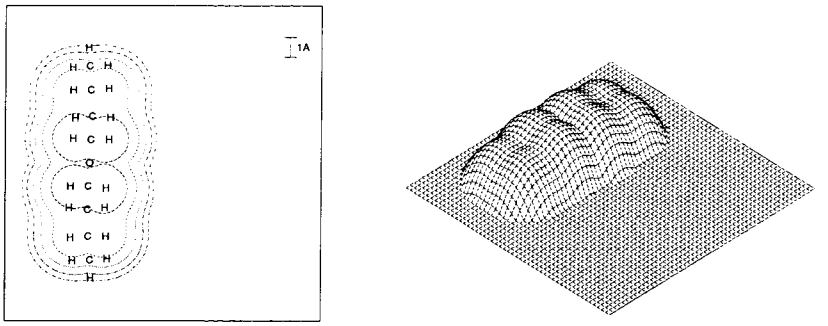

(B) Flat

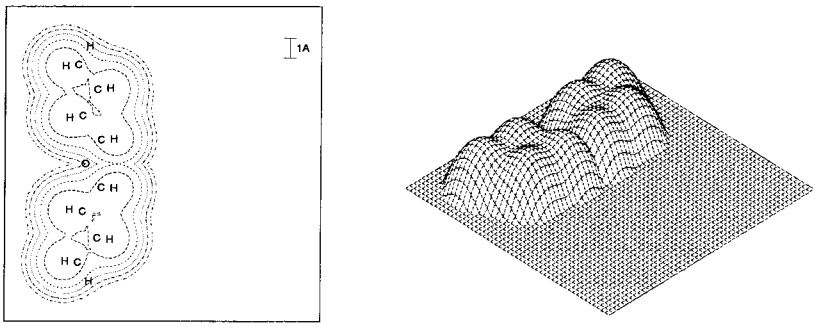

(C) Vertical, O up

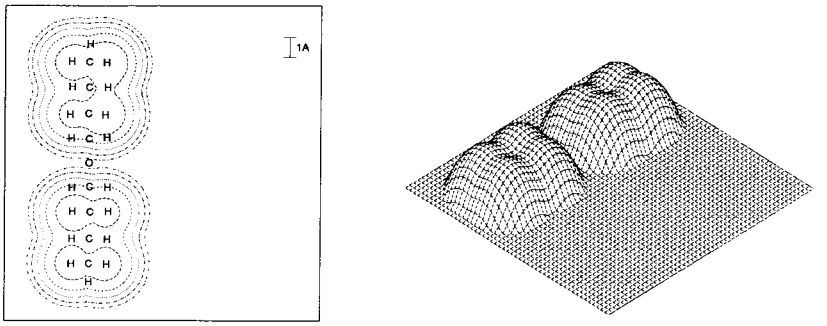

Figure 3.9: Computed constant current STM images of $CH_3(CH_2)_3O(CH_2)_3CH_3$ on graphite. (A) Vertical orientation with the oxygen atom pointing down. (B) Flat orientation. (C) Vertical orientation with the oxygen atom pointing up. The maximum values for the three plots are 2.12, 1.51, and 1.76 a.u., respectively.

molecules by the distance of methylene unit. The experimental observation of θ=26° for the ether packing arrangement in the experimental STM images[2] therefore provides additional support for the suggestion that the ether is adsorbed in the flat orientation on the graphite surface.

3.3.6 Thio-ethers and Thiols

The FF simulation predicts one molecule of $CH_3(CH_2)_{13}S(CH_2)_{13}CH_3$ to be most stable when adsorbed in the flat orientation, and the vertical orientations are predicted to be higher in energy by 7.8 (S down) and 8.8 (S up) kcal/mol. When more molecules are packed at the density observed experimentally, the vertical orientation with the sulfur pointing down becomes the most stable. The other vertical orientation is higher in energy by 6.9 kcal/mol and the flat orientation is higher in energy by 9.2 kcal/mol. Since these orientations were close in energy, STM images were computed for molecules in all three adsorption orientations.

Figure 3.10 presents the STM images predicted for the molecule $CH_3(CH_2)_3S(CH_2)_3CH_3$ in each of the three orientations. In all three orientations the alkyl chains define a linear intramolecular axis, so inspection of the molecular shape alone does not allow identification of the orientation that is being observed experimentally in the STM image unless the position of the sulfur relative to the alkyl chain can be accurately resolved.

In all three orientations, the sulfur appears much brighter than any other portion of the molecule. The lone pair orbitals on the sulfur atom are in the conduction region and are responsible for most of the tunneling current. Under these conditions, the actual size of the bright spot is expected to depend strongly on the dimensions and the shape of the tip. However, for the constant experimental conditions assumed in the simulations, the size of the bright spot is different for the three orientations, being larger in the vertical orientation with the sulfur pointing toward the graphite. The bright spot in the various computed constant current STM images is approximately 10 Å (S down), 8.2 Å (flat), or 5.4 Å (S up), as compared to the experimentally observed value of $6.5-6.7$ Å.[2] This comparison is very instructive, indicating that the large apparent width of the thioether functionality observed in the experimental images[2] can be naturally explained by the electronic structure of this molecule.

Because alkanethiols have also been recently imaged using STM, the images of alkanethiol overlayers were also modeled theoretically in this study. Only the flat adsorption geometry was considered for the molecule $CH_3(CH_2)_7SH$, and the STM simulation was conducted on the molecule $CH_3(CH_2)_3SH$. As displayed in Figure 3.11, the thiol group is overwhelmingly brighter than the rest of the molecule. This prediction is in good agreement with experimental results.[4] The brightness is due to the sulfur nonbonding electrons which enter the conduction region, making the thiol a conductor for the same reason that the S functionality is bright in the STM image of the thioether.

$CH_3(CH_2)_3S(CH_2)_3CH_3$

(A) Vertical, S down

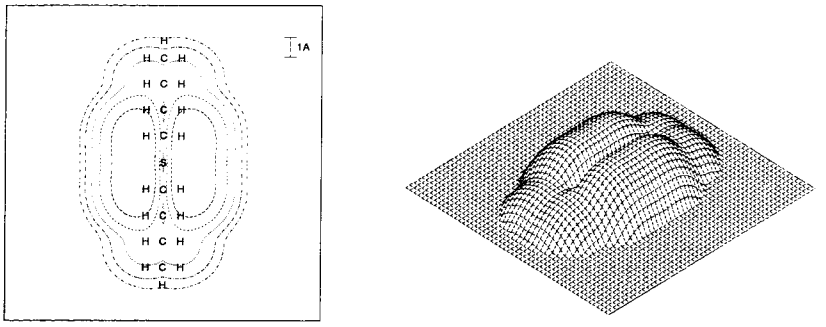

(B) Flat

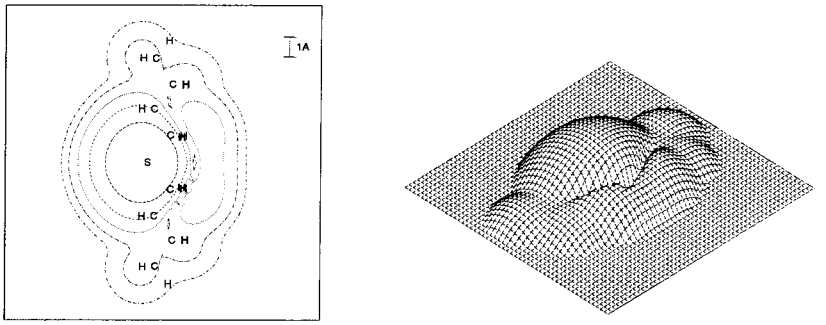

(C) Vertical, S up

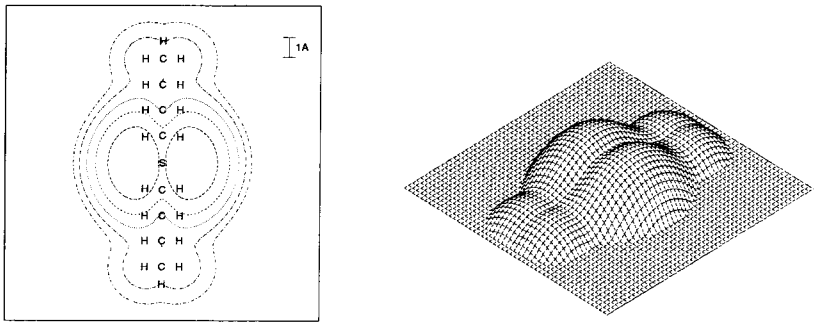

Figure 3.10: Computed constant current STM images of $CH_3(CH_2)_3S(CH_2)_3CH_3$ on graphite. (A) Vertical orientation with the sulfur atom pointing down; (B) flat orientation; (C) vertical orientation, with the sulfur atom pointing up. The maximum values for the three plots are 3.17, 4.26, and 3.74 a.u., respectively.

(A) Flat

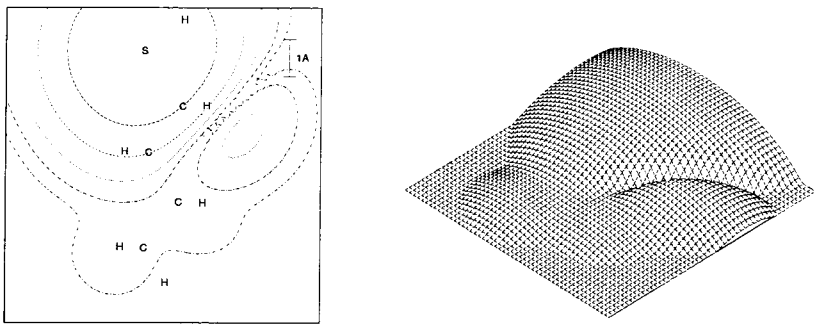

Figure 3.11: Computed constant current STM images of $CH_3(CH_2)_3SH$ laid flat on graphite. The maximum value for the plot is 4.30 a.u.

3.3.7 Disulfide

The molecule used to study the adsorption orientation is $[CH_3(CH_2)_{15}S]_2$. Once again, for a single molecule, the flat adsorption orientation was computed to be favored, being lower in energy by 10.4 kcal/mol, while the vertical orientation is more stable by 7.9 kcal/mol for densely packed systems. Also, for this system, the lowest energy conformation of the vertical orientation of $CH_3(CH_2)_{15}SS(CH_2)_{15}CH_3$ had the carbon-carbon skeletons of both alkyl chains oriented perpendicular to the graphite surface plane. This adsorbate geometry is significantly different than the lowest energy molecular conformation for the disulfide in the gas phase, in which the carbon-carbon skeletons of the alkyl chains are mutually perpendicular.

The STM predictions for the computed lowest energy flat and vertical orientations are reported for negative bias in Figure 3.12. The computed images reveal that the disulfide functionality is much brighter than the rest of the molecule in either orientation. As discussed above for the iodoalkanol, the bright spot is due to the lone pair electrons on the sulfur, which become conducting electrons and thereby facilitate electronic coupling between the tip and the graphite. The apparent width of the disulfide functionality in the computed STM image is $9.4 - 11.3$ Å, which is in good agreement with the experimentally observed value of $11.6 - 12.6$ Å. As is the case for the thioether, this agreement indicates that the very large width of the disulfide functional group in the experimental STM image has a very plausible physical explanation in terms of the electronic structure of the disulfide moiety.

3.3.8 Primary and Secondary Amines

Both primary and secondary amines have been imaged recently using STM. We first discuss the theoretical results for the secondary amine and then extend these findings to a primary amine.

For the secondary amine, four possible adsorption orientations must be considered: two flat

$CH_3(CH_2)_3SS(CH_2)_3CH_3$

(A) Flat

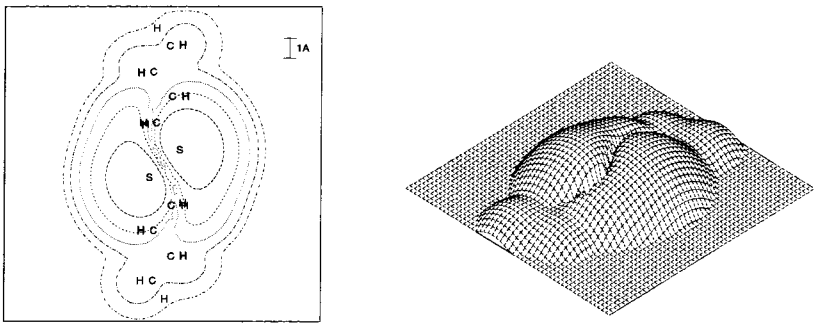

(B) Vertical

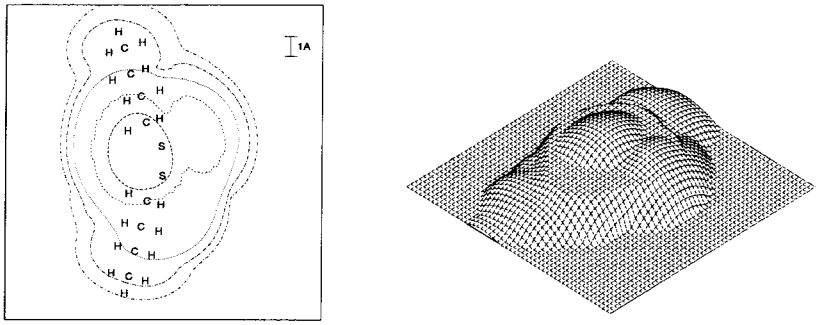

Figure 3.12: Computed constant current STM images of $CH_3(CH_2)_3SS(CH_2)_3CH_3$ on graphite. (A) Flat orientation; (B) vertical orientation. The maximum values of the plots are 4.10 and 4.57 a.u., respectively.

(A) Flat, NH up

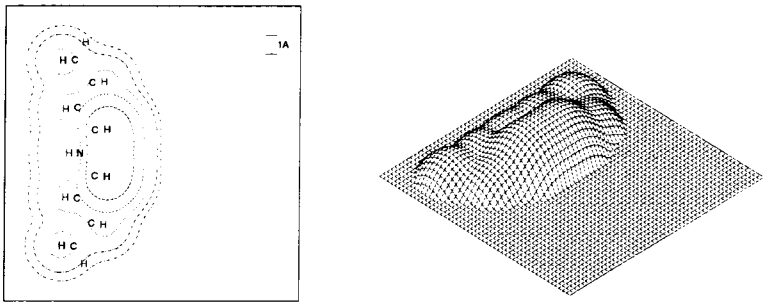

(B) Flat, NH down

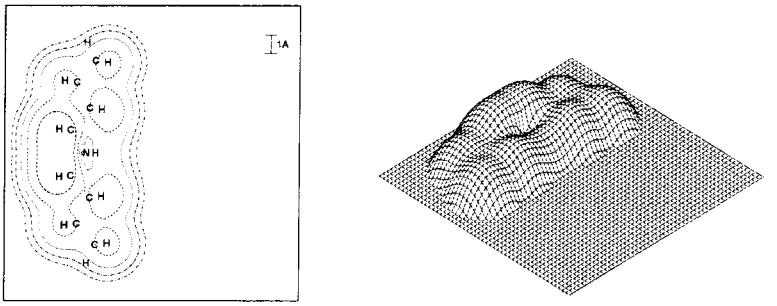

(C) Vertical, NH up

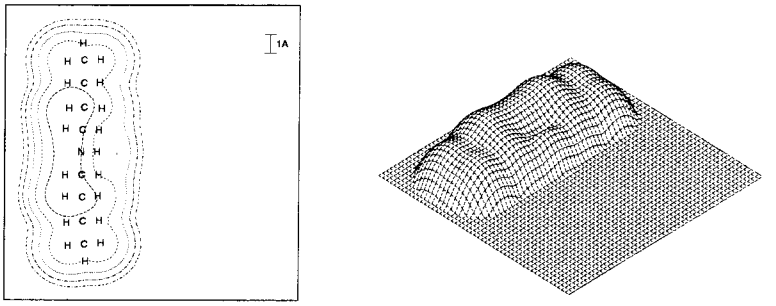

(D) Vertical, NH down

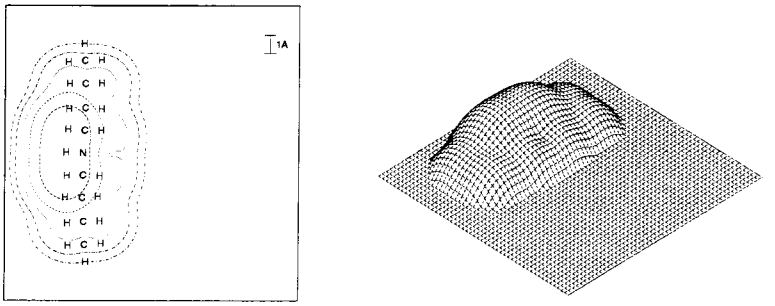

Figure 3.13: Computed constant current STM images of $CH_3(CH_2)_3NH(CH_2)_3CH_3$ on graphite. (A) flat orientation with the NH group pointing up; (B) flat orientation with the NH group pointing down; (C) vertical orientation with the NH group pointing up; (D) vertical orientation with the NH group pointing down. The maximum values for the plots are 2.71, 2.16, 2.26, and 3.00 a.u., respectively.

and two vertical, with the amine hydrogen pointing either toward the graphite or away from the graphite. FF simulations on the molecule $CH_3(CH_2)_{17}NH(CH_2)_{17}CH_3$ predict isolated molecules to be more stable by 9.9 kcal/mol in the flat orientations and packed molecules to be more stable by 10.4 kcal/mol in the vertical orientations. Nevertheless, STM images were computed for all four orientations (Figure 3.13).

When the molecule is flat, the amine is predicted to be brighter than the rest of the molecule (Figures 3.13A,B). The brightness is localized on the hydrogen atoms which are close to the nitrogen and point toward the tip. The predicted brightness is due to the fact that the HOMO, which is localized on the amine, is in the conduction region, making the molecule a conductor.

When the molecule is vertical, the amine is only slightly brighter than the alkane chain when the NH group is pointing up (Figure 3.13C) and it is bright when the NH is pointing down (Figure 3.13D). The prediction is in qualitative agreement with the experimental image for three of the four possible orientations,[2] and further assignment cannot be made with the resolution of the STM data available at present.

To describe the properties of primary amines, the adsorption geometry of the molecule $CH_3(CH_2)_7NH_2$ was studied when the alkyl chain is flat. Three conformations were considered, in which the lone pair of the amine group was either flat (*trans* to the alkyl chain), pointing up or pointing down. All three conformations are found to lie within 0.5 kcal/mol of each other, and were investigated theoretically.

The STM simulation was carried out on the molecule $CH_3(CH_2)_3NH_2$, and the results are reported in Figure 3.14. For all three conformations, the amine appears to be bright, with the main spot centered on the α hydrogens. This result is in qualitative agreement with the experimental images reported in the literature for a primary amine,[4] although the exact position of the bright spot could not be determined from the STM data on this system. The computations indicate that the low IP of the amine brings the HOMO of the adsorbate into the conduction region. The HOMO has significant contributions from the α hydrogens, which have a good coupling with the tip and the graphite and appear therefore bright in the simulation.

3.3.9 Alkene

FF minimizations on the adsorbed molecule $CH_3(CH_2)_{15}CHCH(CH_2)_{16}CH_3$ predict that isolated molecules should adsorb in the flat orientation, with the vertical orientation being more energetic by 9.1 kcal/mol. Packed molecules on the graphite surface are more stable by 11.8 kcal/mol in the vertical orientation, with the double-bond region strongly distorted toward a flat orientation and the rest of the molecule oriented vertically. We considered both orientations for the STM simulation.

The images obtained for *trans*-5-decene are reported in Figure 3.15. Both orientations exhibit a bright spot located close to the double bond, in agreement with the experimental results.[2] The

$CH_3(CH_2)_3NH_2$ Flat

(A) Lone pair flat

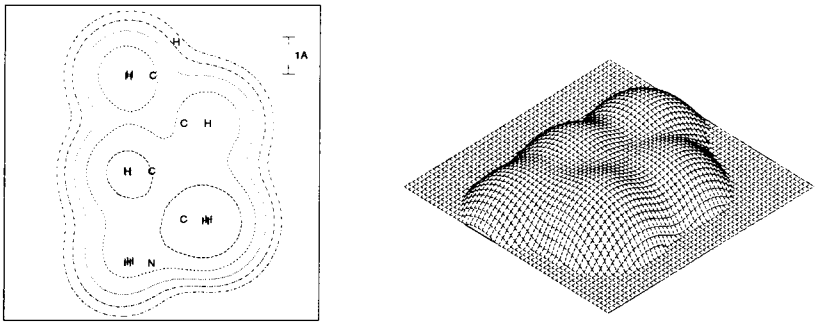

(B) Lone pair up

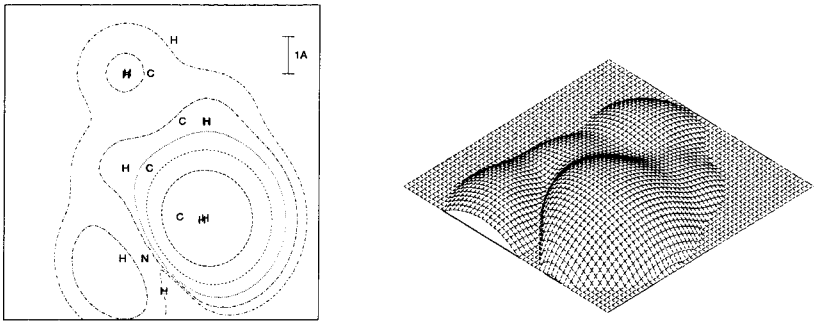

(C) Lone pair down

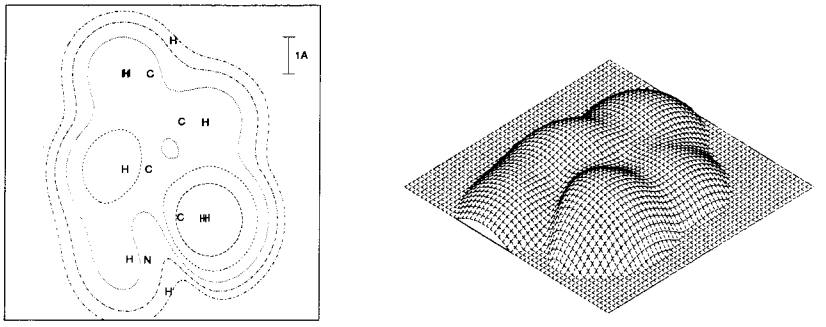

Figure 3.14: Computed constant current STM images of $CH_3(CH_2)_3NH_2$ adsorbed flat on graphite. (A) Amine lone pair flat; (B) amine lone pair pointing up; (C) amine lone pair pointing down; The maximum values for the three plots are 1.39, 2.49, and 1.74 a.u., respectively.

$$CH_3(CH_2)_3HC = CH(CH_2)_3CH_3$$

(A) Flat

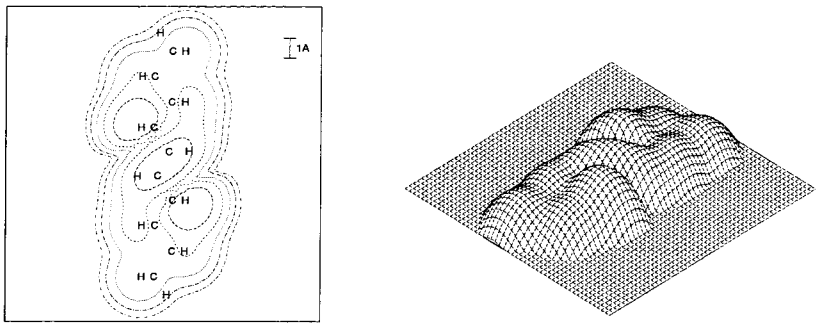

(B) Vertical

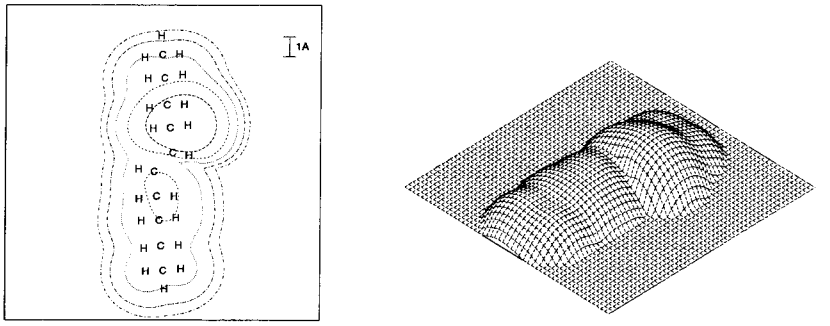

Figure 3.15: Computed constant current STM images of $CH_3(CH_2)_3CHCH(CH_2)_3CH_3$ on graphite. (A) Flat orientation; (B) vertical orientation. The maximum values for the plots are 2.38 and 3.52 a.u., respectively.

$CH_3(CH_2)_3C \equiv C(CH_2)_3CH_3$

(A) Flat

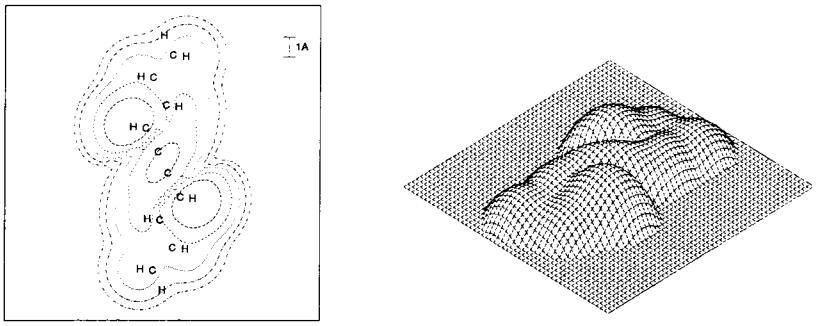

Figure 3.16: Computed constant current STM images of $CH_3(CH_2)_3CC(CH_2)_3CH_3$ laid flat on graphite. The maximum value for the plot is 2.58 a.u.

high conductivity of this functionality in the STM experiment is due to the HOMO being located in the conduction region. In the flat orientation, the bright spot is centered on top of the double bond, essentially imaging the π system of the molecule (Figure 3.15A). In contrast to this electronic effect, in the vertical orientation the bright spot is dominated by topographical considerations, and arises from the location of one of the hydrogen atoms pointing up from the molecule towards the tip (Figure 3.15B). Better resolution would be needed to distinguish between these possibilities experimentally.

Interestingly, the packing arrangement displayed by the *trans*-pentatriacontene produced an angle θ of 0° in the experimental STM images.[2] In this case, the possibility of significant intermolecular forces between the double bonds in the overlayer must be considered. Thus, for this system, the observed packing angle does not uniquely identify the orientation of the carbon-carbon skeleton, but it can be taken to indicate that the double bonds are in translational registry in the overlayer as would be expected for significant $\pi - \pi$ interactions between adsorbed molecules.

3.3.10 Alkyne

The molecule studied experimentally by Claypool et al. is 7-hexadecyn-1-ol.[2] Since alkanols prefer to lay flat on the graphite,[2] only the flat orientation was investigated computationally.

The predicted image for 5-decyne, at a bias of -1 eV, is reported in Figure 3.16. In this image, the triple bond and the surrounding hydrogens appear to be brighter than the rest of the molecule, in agreement with experimental data on 7-hexadecyn-1-ol[2] as well as on 10,12 octadecadiynoic acid.[5] The simulated width of the bright spot around the triple bond was 6.4 Å, versus the experimental observation of $3.5 - 4.3$ Å.[2] Additionally, the flat orientation is expected to produce a kink around the triple bond due to the geometry of the molecule, and this feature is observed in the experimental STM images of the alkyne overlayers.[2]

$CH_3(CH_2)_3CN$

(A) Flat

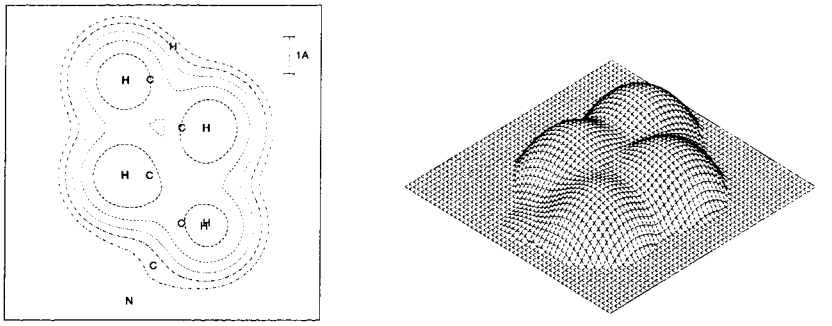

Figure 3.17: Computed constant current STM images of $CH_3(CH_2)_3CN$ laid flat on graphite. The maximum value of the plot is 1.09 a.u.

3.3.11 Nitrile

Figure 3.17 depicts the predicted STM image of a nitrile. This functionality also has a π system, like the alkenes and alkynes discussed above, yet it appears dark in the experimental STM image.[2] This behavior is reproduced in the computed STM images. The nitrile HOMO is much lower in energy than that of the alkyl chain; additionally, in the energetically favored *trans-* conformation, the nitrile group is farther from the tip than are the methylene hydrogens in the alkyl chain. Thus, both electronic and geometric considerations would predict the group to be dark, in accord with the experimental STM data for nitrile-containing alkyl overlayers on graphite.[2]

3.3.12 Acid Dimer

Prior work has described STM images of carboxylic acids on graphite.[3, 5] To investigate this system theoretically, the dimer $[CH_3(CH_2)_7COOH]_2$ was studied to determine the adsorption geometry. Only the adsorption of one dimer was studied in the flat configuration.

The STM simulation was then performed on the smaller dimer $[CH_3(CH_2)_3COOH]_2$, and the results are reported in Figure 3.18. The acid region appears to be dark, in good agreement with the experimental results.[3] This occurs because, similar to the nitrile group, the π system of the acid group is very stable. The HOMO remains far from the conduction energy and the image is dominated by the alkyl hydrogens, which are closer to the tip.

3.3.13 Ketone

FF simulations on the molecule $CH_3(CH_2)_{16}CO(CH_2)_{16}CH_3$ indicate that the flat orientation is expected to be most stable for a singly adsorbed molecule, while the vertical orientations with CO pointing down and up are 12.4 and 9.0 kcal/mol more energetic, respectively. For packing densities

$(CH_3(CH_2)_3COOH)_2$

(A) Flat

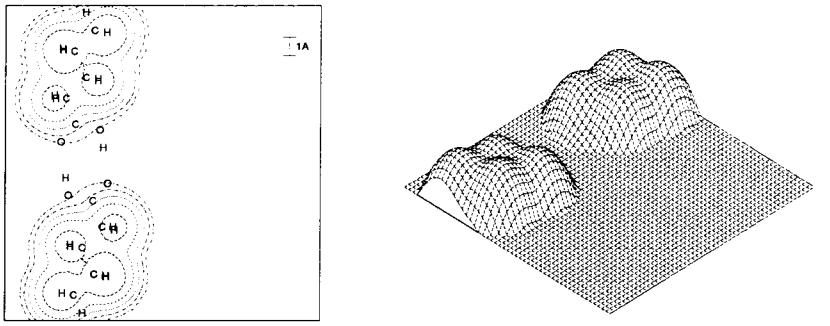

Figure 3.18: Computed constant current STM images of $[CH_3(CH_2)_3COOH]_2$ laid flat on graphite. The maximum value for the plot is 1.72 a.u.

close to those observed experimentally, the vertical orientation with CO pointing up is most stable, the vertical orientation with CO pointing down is less stable by 8.5 kcal/mol, and the flat geometry is less stable by 9.5 kcal/mol.

Figure 3.19 reports the computed STM images for $CH_3(CH_2)_3CO(CH_2)_3CH_3$ in each of the three orientations. The ketone region is bright in the STM image when the molecule is in the vertical orientation with the CO pointing down (Figure 3.19A). The brightness is predominantly topographic in origin and is due to the fact that the hydrogens closest to the CO are pushed toward the tip. In the flat orientation, the ketone is predicted to be dark (Figure 3.19B). The dark region extends over the hydrogens on the α carbons and, to a minor extent, to those on the β carbons with respect to the CO. In the vertical orientation with the CO pointing up, the ketone is predicted to be bright in the STM image (Figure 3.19C).

No conclusive experimental images are available for comparison with these computational results. Preliminary experimental data, however, gave a bright spot on the ketone for negative bias and a dark region for positive bias.[2] According to the theoretical model presented above for the effects of bias in STM experiments, based on the derivation of Marcus,[2, 18] images obtained under positive and negative bias should be very similar unless the orientation or geometry of the molecule is different at the different bias polarities. Since the ketone is a polar group, it is possible that the transition from the flat to the vertical orientation with the CO pointing up is more favorable when the graphite has a negative charge (negative bias) than when the graphite has a positive charge. If this is the case, the observed images should depend on the history of the sample, with fresh samples having the molecules in the flat orientation and old samples, as well as samples already used for negative bias STM, having the molecules in the vertical orientation. These considerations are being investigated experimentally at present for ketones and for other highly polar functionalities adsorbed on graphite surfaces.

$CH_3(CH_2)_3CO(CH_2)_3CH_3$

(A) Vertical, CO down

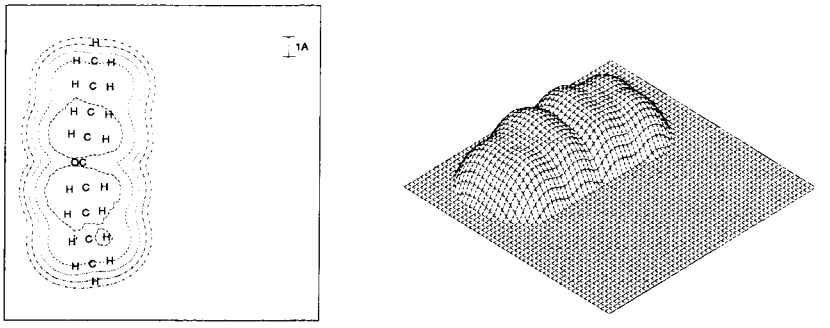

(B) Flat

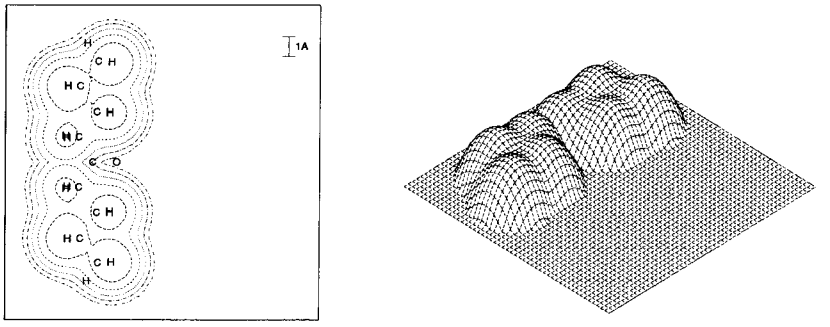

(C) Vertical, CO up

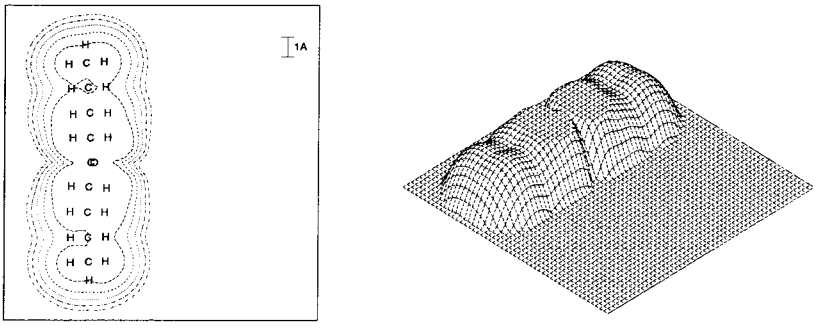

Figure 3.19: Computed constant current STM images of $CH_3(CH_2)_3CO(CH_2)_3CH_3$ on graphite. (A) Vertical orientation with the CO pointing down toward the graphite; (B) flat orientation; (C) vertical orientation with the CO pointing up. The maximum values for the three plots are 2.23, 1.63, and 1.77 a.u., respectively.

3.4 Discussion

The predicted STM images reproduce the qualitative features of all of the experimental STM data reported by Claypool at al. as well as those of other results on related systems.[2-6] These computations have provided physically reasonable explanations for the STM image contrast of all of the functional groups investigated experimentally, and also allow an understanding of the widths of the various functional groups that have been observed in the experimental STM data.[2] In addition, the results explain the angles between the spots observed in the STM images of alkyl chains, and in a number of cases allow assignment of the orientation of the adsorbates with respect to the graphite surface plane. The computations also allow separation of the importance of electronic and topographic effects in the STM images of many of the systems studied experimentally.

An interesting result arising from the computational model used in this work is the predicted importance of the virtual orbitals of the halogenated alkanols and of other related substituted alkanes in defining the STM image contrast. This result is different from the HOMO-dominated electronic coupling that is believed to determine electron tunneling matrix elements in intramolecular electron transfer processes between a donor and an acceptor connected to an alkane chain. The difference in importance of the occupied and virtual orbitals arises because the STM experiment is much more sensitive to the shape of the orbitals that are projected into the localized region defined by the tip-sample gap; thus, the more diffuse virtual orbitals can play a much more dominant role in defining the overall electronic coupling term in an STM experiment despite being significantly farther in energy from the Fermi level of the substrate than the occupied orbitals. Although the relative contributions of the virtual and occupied orbitals in determining electronic coupling matrix elements in an STM image have not been definitively established experimentally, the calculations presented herein should offer a framework for future experimental studies that are designed to evaluate these effects in a systematic fashion.

The computational results have allowed classification of the functional groups into three categories, based on how their electronic structure affects the contrast in an STM image. These categories are discussed briefly below.

3.4.1 Conductors

These functional groups have an IP lower than a fixed value I_0. The exact value of I_0 is not known, but based on the available data it is between the IP of an alkyl bromide and that of an alkyl amine.[2] These groups have one (or more) orbital, in resonance with the conduction states on the tip and on the graphite, that is responsible for most of the observed current. As the STM image is essentially a map of the conducting orbitals, these groups tend to appear much brighter than the alkyl chain. For functionalized alkanes on graphite, this category of functional groups includes disulfides, thioethers,

thiols, amines, alkenes, alkynes, and alkyl iodides. This functional group classification is closely related to the HOMO-IP model discussed by Claypool et al.[2]

3.4.2 Dark Groups

Functional groups that are not conductors and that have low electron affinities appear dark. This is because the coupling is small through both the HOMO and LUMO. In addition, the computations indicate that most of the tunneling current in the systems evaluated in this work is described by the low lying virtual orbitals, much like a low energy electron diffraction process. Virtual orbitals, in fact, need to be orthogonal to the occupied orbitals. Since the occupied orbitals tend to be close to the nuclei, the virtual orbitals are therefore squeezed toward the outside of the molecule and have better overlap, in general, with the tip and graphite, so they can dominate the tunneling matrix element that is responsible for the STM process. Functional groups with electron affinities lower than that of the corresponding alkane will hence be dark in the STM image. Nonconducting functional groups in this class include *trans*-conformations of alkyl fluorides, alkyl chlorides, alkyl bromides, and alcohols, as well as ethers and trifluoromethyene units.

3.4.3 Bright Groups

Functional groups with high electron affinities but which are not conductors, are expected to be brighter than the alkyl chain. However, these groups are not expected to appear as bright as conductors. Since the relative energies of the virtual orbitals localized on different parts of the molecule must be compared, it is also important to consider that charge-withdrawing groups will lower the electron affinity of the alkyl chain, effectively shifting the reference intensity of neighboring groups that might be used to establish the STM image contrast of the functional group. No functional groups in this class have been observed yet.

3.4.4 Relative Importance of Geometric and Electronic Effects

Since the electronic coupling is determined strongly by the overlap of each orbital with the tip and the graphite, the geometry of the molecule plays a key role in determining the STM image. In fact, the theoretical STM images presented in this work reveal that the experimental STM data for most of the functionalized alkane overlayers investigated to date are dominated by topographic effects of the molecules in the overlayer. Functional groups which are close to the tip (or to the graphite) will thus tend to appear bright unless there are strong electronic effects that reduce the orbital overlap in this region of space. Fluorinated alkyls (Figure 3.7) provide an example of this interplay between topographic and electronic effects in determining the contrast of an STM image. A theoretical description of the image contrast of such systems therefore requires an evaluation of

electronic and steric effects in a fairly detailed fashion.

The conclusion that most molecules are imaged through the virtual orbitals is consistent with the observation that at low bias the graphite is imaged while at high bias the molecules are observed. The long-range behavior of an electronic wavefunction in a Coulomb potential is described by[15]

$$\psi(\mathbf{r}) = f(\mathbf{r})\epsilon^{-\lambda r} \quad ; \qquad \lambda = \sqrt{2|E|} \tag{19}$$

where $f(\mathbf{r})$ diverges at most like a polynomial. Therefore, in general, the occupied MOs of the absorbate decay faster than the orbitals of the substrate that have energies near the graphite Fermi level. These graphite orbitals, in turn, decay faster than the virtual MOs of the absorbate overlayer. It follows that if the occupied orbitals dominate the STM images at large distances, then they should also dominate the image at smaller distances. Thus, the experimental data, which show a transition from images of graphite at small tip-sample biases to images of the overlayer at large tip-sample biases, are in accord with the behavior expected for the situation where the virtual orbitals of the molecular overlayer dominate the electronic coupling in the tip-sample gap. This result is, however, only described qualitatively at present because the graphite states were omitted in our simulation method so that the description of the STM data at high bias could be obtained in a straightforward fashion.

3.4.5 Expense of the Computational Methods

The computational methods were reasonably inexpensive to perform. The computational cost of each prediction can be roughly divided as follows: 40% to optimize the adsorption geometry, 55% to run the HF computation, and 5% to run the actual STM simulation. The overall computer (CPU) time on HP9000/735 workstations is of the order of 30 minutes for the small molecules and 1 hour for the largest ones. Thus, this theoretical framework can be readily adopted by a variety of researchers in order to guide future experimental investigations of the mechanisms underlying the image contrast of molecules in an STM experiment. Numerous theoretical predictions have been advanced in this chapter that will be interesting to explore experimentally, and the hope is that this set of predictions will stimulate experimental studies designed to further elucidate the factors that control these interesting atomic-resolution imaging processes.

3.5 Summary and Conclusions

In summary, a simple model, based on perturbation theory, was used to predict the STM images of molecules adsorbed on graphite. The geometries of the adsorbed molecules were estimated using a FF and the unperturbed molecular wavefunction was assumed to be the HF wavefunction for the

gas-phase molecule, except for a simple shifting of the orbital energies to account for the fact that during the tunneling process the molecule is in close proximity to two conductors: the tip and the graphite.

The model contains one adjustable parameter representing the interaction between the molecules and the graphite. This parameter is expected to change very little for different molecules of the same family, and it was fixed to a value that seems to reproduce most of the experimental images.

For most of the molecules investigated in this study, topographic effects were observed to play a key role in determining the contrast observed in the experimental STM images. In fact, this correlation allows assignment of the orientation of most of the molecules with respect to the plane of the graphite surface, and allows formulation of predictions regarding how the image contrast should be affected as the molecular orientation is varied. Electronic effects on the STM image contrast were revealed through an analysis of the orbital coupling properties of functional groups such as fluoromethyl and perflоromethylene units in the alkane and alkanol overlayers investigated in this work.

The theoretical predictions are mainly qualitative, but they can provide significant insight into the experimental STM images and can define further avenues of interest in the experimental investigation of STM imaging mechanisms with a minor computational cost.

Appendix: Bias dependence in formulas (8), (16) and (18).

The bias dependence in Eq. (8) appears in two forms: (1) the integration domain is the conduction region CR defined as

$$CR = \begin{cases} \{E : E \in (E_f, E_f + E_b)\} & \text{for negative bias } (E_b > 0) \\ \{E : E \in (E_f + E_b, E_f)\} & \text{for positive bias } (E_b < 0) \end{cases}$$

where E_f is the fermi energy and $-E_b$ is the bias; (2) the scaled orbital energies E_k are

$$E_k = \epsilon_k + \frac{1}{2}E_b$$

where ϵ_k is the original orbital energy.

We can write Eq. (8) as:

$$I_{gt} = \frac{2\pi}{\hbar}\int_{E_f}^{E_f+E_b}\left|\sum_k \frac{V_{gk}V_{kt}}{(E - E_k - \frac{1}{2}E_b)}\right|^2 \rho_t(E)\rho_g(E)dE$$

with the assumption that the absolute value of the integral be taken.

Including explicitly the dependence in Eq. (16) requires the definition of a new function $F(E)$:

$$F(E) = \begin{cases} 1 & \text{if } E \notin CR \\ 0 & \text{if } E \in CR \end{cases}$$

Equation (16) becomes then (again, we need to take the absolute value of the integral, but this time the relation is formally correct due to the $\propto$ symbol):

$$I \propto \int_{E_f}^{E_f+E_b} \rho_t(E)\rho_g(E) \left\{ \left[\sum_k \frac{F(E_k + \frac{1}{2}E_b) V_{gk} V_{kt}}{(E - E_k - \frac{1}{2}E_b)} \right]^2 + \right.$$
$$\left. + \left[\pi \sum_k \left(1 - F(E_k + \frac{1}{2}E_b) \right) V_{gk} V_{kt} \delta^{(\epsilon)}(E - E_k - \frac{1}{2}E_b) \right]^2 \right\} dE$$

Finally, Eq. (18) becomes:

$$I \propto \int_{E_f}^{E_f+E_b} (E_f - E)^2 \left[\sum_k \frac{F(E_k + \frac{1}{2}E_b) V_{gk} V_{kt}}{(E - E_k - \frac{1}{2}E_b)} \right]^2 +$$
$$+ \int_{E_f}^{E_f+E_b} (E_f - E)^2 \left[\pi \sum_k \left(1 - F(E_k + \frac{1}{2}E_b) \right) V_{gk} V_{kt} \delta^{(\epsilon)}(E - E_k - \frac{1}{2}E_b) \right]^2 dE$$

Acknowledgments

We thank C. L. Claypool and N. S. Lewis for major contributions to this work and H. B. Gray and R. A. Marcus for discussing the theory. The research was funded by NSF (CHE 95-22179 and ASC 92-17368; WAG and CHE-9202583; NSL). The facilities of the MSC are also supported by grants from DOE-BCTR, Chevron Petroleum Technology Co., Asahi Chemical, Aramco, Owens-Corning, Asahi Glass, Chevron Research Technology Co., Chevron Chemical Co., Hercules, Avery-Dennison, BP Chemical, and the Beckman Institute.

Bibliography

[1] Faglioni, F.; Claypool, C.L.; Lewis, N.S.; Goddard III, W.A.; *J. Phys. Chem. B* **1997**, *101*, 5996.

[2] Claypool, C.L.; Faglioni, F.; Goddard III, W.A.; Gray, H.B.; Lewis, N.S.; Marcus, R.A.; *J. Phys. Chem. B* **1997**, *101*, 5978.

[3] Liang, W.; Whangbo, M.-H.; Wawkuschewski, A.; Cantow, H.-J.; Magonov, S.N.; *Adv. Mater.* **1993**, *5*, 817. Bar, G.; Magonov, S.N.; Cantow, H.-J.; Kushch, N.D.; Yabubskii, E.B.; Liang, W.; Ren, J.: Whangbo, M.-H.; *New J. Chem.* **1993**, *17*, 439.

[4] Venkataraman, B.; Flynn, G.W.; Wilbur, J.L.; Folkers, J.P.; Whitesides, G.M.; *J. Phys. Chem.* **1995**, *99*, 8684. Cyr, D.M.; Venkataraman, B.; Flynn, G.W.; Black, A.; Whitesides, G.M.; *J. Phys. Chem.* **1996** *100*, 13747. Cyr, D.M.; Venkataraman, B.; Flynn, G.W.; *Chem. Mater.* **1996**, *8*, 1600.

[5] Rabe, J.P.; Buchholz, S.; *Science* **1991**, *253*, 424. Rabe, J.P.; Buchholz, S.; Askadskaya, L.; *Synt. Met.* **1993**, *54*, 339.

[6] Magonov, S.N.; Whangbo, M.-H.; *Surface Analysis with STM and AFM*, (VCH, 1996).

[7] Tersoff, J.; Hamman, D.R.; *Phys. Rev. Lett.* **1983**, *50*, 1998. Tersoff, J.; Hamman, D.R.; *Phys. Rev. B* **1985**, *31*, 805.

[8] Bardeen, J.; *Phys. Rev. Lett.* **1961**, *6*, 57.

[9] Lang, N.D.; *Phys. Rev. Lett.* **1985**, *55*, 230. Lang, N.D.; *Phys. Rev. Lett.* **1986**, *56*, 1164.

[10] Doyen, G.; Drakova, D.; Kopatzki, E.; Behm, R.J.; *J. Vac. Sci. Technol. A* **1988**, *6*, 327. Kopatzki, E.; Doyen, G.; Drakova, D.; Behm, R.J.; *J. Microsc.* **1988**, *152*, 687.

[11] Hallmark, V.M.; Chiang, S.; Meinhardt, K.P.; Hafner, K.; *Phys. Rev. Lett.* **1993**, *70*, 3740. Hallmark, V.M.; Chiang, S.; *Surf. Sci.* **1995**, *329*, 255.

[12] Sautet, P.; Joachim, C.; *Chem. Phys. Lett.* **1991**, *185*, 23. *Surf. Sci.* **1991**, *271*, 387. Sautet, P.; Bocquet, M.L.; *Surf. Sci.* **1994**, *304*, L445.

[13] Fisher, A.J.; Blöchl, P.E.; *Phys. Rev. Lett.* **1993**, *70*, 3263.

[14] Yang, H.O.; Marcus, R.A.; Källebring, B.; *J. Chem. Phys.* **1994**, *100*, 7814.

[15] Landau, L.D.; Lifshits, E.M.; *Quantum Mechanics*, (Pergamon Press, 1977).

[16] Hehre, W.J.; Stewart, R.F.; Pople, J.A.; *J. Chem. Phys.* **1969**, *51*, 2657.

[17] Koryta, J.; Dvorak, J.; Kavan, L.; *Principles of Electrochemistry*, (John Whiley & Sons Ltd., 1993).

[18] Marcus, R.A.; *J. Chem. Soc., Farad. Trans*, in press.

[19] Landolt-Börnstein *Numerical Data and Functional; Relationships in Science and Technology* New Series, Vol. 13c, (Springel-Verlag). Charlier, J.C.; Gonze, X.; Michenaud, J.P.; *Phys. Rev. B* **1991**, *43*, 4579.

[20] Mayo, S.L.; Olafson, B.D.; Goddard III, W.A.; *J. Phys. Chem.* **1990**, *94*, 8897.

[21] Rappé, A.K.; Goddard III, W.A.; *J. Phys. Chem.* **1991**, *95*, 3358.

[22] Morishige, K.; Takami, Y.; Yokota, Y.; *Phys. Rev. B* **1993**, *48*, 8277.

[23] *Gaussian 92/DFT*, Revision F.4, Frisch, M.J.; Trucks, G.W.; Schlegel, H.B.; Gill, P.M.W.; Johnson, B.G.; Wong, M.W.; Foresman, J.B.; Robb, M.A.; Head-Gordon, M.; Replogle, E.S.; Gomperts, R.; Andres, J.L.; Raghavachari, K.; Binkley, J.S.; Gonzalez, C.; Martin, R.L.; Fox, D.J.; Defrees, D.J.; Baker, J.; Stewart, J.P.P; Pople, J.A.; Gaussian, Inc., Pittsburgh, PA, 1993. *Gaussian 94*, Revision B.3, Frisch, M.J.; Trucks, G.W.; Schlegel, H.B.; Gill, P.M.W.; Johnson, B.G.; Robb, M.A.; Cheeseman, J.R.; Keith, T.; Petersson, G.A.; Montgomery, J.A.; Raghavachari, K.; Al-Laham, M.A.; Zakrzewski, V.G; Ortiz, J.V.; Foresman, J.B.; Peng, C.Y.; Ayala, P.Y.; Chen, W.; Wong, M.W.; Andres, J.L.; Replogle, E.S.; Gomperts, R.; Martin, R.L.; Fox, D.J.; Binkley, J.S.; Defrees, D.J.; Baker, J.; Stewart, J.P.P; Head-Gordon, M.; Gonzalez, C.; Pople, J.A.; Gaussian, Inc., Pittsburgh, PA, 1995.

[24] Pairler, G.E.; Pylant, E.O.; *Science* **1996**, *272*, 1145.

[25] Lias, S.G.; Levin, R.D.; *Ionization Potential and Appearance Potential Measurements, 1971-1981* U.S. Department of Commerce/National Bureau of Standards (1982).